Visualization and analysis of particle settling and clogging behavior in porous media

Yang Li

COLLEGE DOCTORAL BRETAGNE SCIENCES POUR L'INGENIEUR

INSA INSTITUT NATIONAL DES SCIENCES APPLIQUÉES RENNES

THÈSE DE DOCTORAT DE

L'INSTITUT NATIONAL DES SCIENCES APPLIQUÉES DE RENNES

ÉCOLE DOCTORALE №647
Sciences pour l'Ingénieur
Spécialité : *Génie Civil*

Par
Yang LI

Visualization and analysis of particle settling and clogging behavior in porous media

Thèse présentée et soutenue à INSA Rennes, le 16/07/2024
Unité de recherche : LGCGM
Thèse №: 24ISAR 14 / D24 - 14

Rapporteurs avant soutenance :

Azita AHMADI-SENICHAULT — Professeure, Arts et Métiers, Bordeaux
Stéphane CHAMPMARTIN — Maître de conférences HDR, Arts et Métiers, Angers

Composition du Jury :

Président :	Abdelghani SAOUAB	Professeur, Université de Normandie, Le Havre
Examinateurs :	Azita AHMADI-SENICHAULT	Professeure, Arts et Métiers, Bordeaux
	Stéphane CHAMPMARTIN	Maître de conférences HDR, Arts et Métiers, Angers
Dir. de thèse :	Mustapha HELLOU	Professeur, INSA de Rennes
Co-encad. de thèse :	Khaled BOURBATACHE	Maître de Conférences, INSA de Rennes
Co-encad. de thèse :	Franck LOMINÉ	Maître de Conférences, INSA de Rennes

Contents

INTRODUCTION

Transportation and clogging of suspensions are widely involved in many civil engineering applications, such as aquifer storage and restoration [1], clogging of permeable pavements [2], [3], clogging of riverbeds [4], oil extraction [5] and so on. The clogging or unclogging phenomenon due to particle transportation can have a significant impact on the efficiency as well as the economy of the original porous media [6]. For example, clogging of permeable pavements reduces the infiltration of rainwater and significantly reduces the function of drainage [7]; clogging of rock formations in oil extraction reduces the production of oil [5]. Therefore, it is very necessary to study the transportation and clogging phenomena of suspensions, to avoid their negative effects and maximize the performance of porous media.

Many macroscopic column experiments have been realized to show the influence of different factors on clogging phenomena: the size of suspended particles, their concentration, the size of the medium grains, the injection rate of the suspension, etc., on the permeability, the deposition profile, the pressure drop of the porous medium [8]–[11]. Among them, the particle size ratio is widely used to predict the occurrence of clogging, but the critical value is not uniform in different experiments [4], [11], [12]. Similarly, it remains difficult to quantify the effect of concentration on the onset and development of clogging [4], [8]. This is mainly because we still lack information on particle deposition within the column medium, and the complex interaction between particles, fluids, and media, and the heterogeneity of the various parameters make it even more challenging to study this phenomenon [13].

The deposition of suspended particles in porous media involves many mechanical effects, including gravity, buoyancy, inertia, drag, lubrication, and contact forces [13], [14]. Some dimensionless numbers have been proposed to quantify the forces that dominate the deposition behavior of particles, such as Stokes number, Archimedes number, and so on [15]. Meanwhile, many researchers have investigated the effect of different forces on particle deposition and blockage formation at the pore scale. The results show that the size of the particles, the nature of the fluid, and the structure of the porous medium can significantly affect this process [15]–[17]. Some simple models have been developed to describe

the probability of clogging at a single pore throat and the dynamic deposition profile of non-gravitational particles within the medium [18], [19]. The transportation and clogging behavior at the pore scale should be investigated further, to refine these models with more related factors.

In this study, we further contribute to this research by analyzing the settling of particles into porous media. The investigation method employed is the visualization of particle motion into transparent porous media made in the laboratory. In Chapter 1, we present in detail the state of the art on particle transportation and clogging, including the application areas involved in clogging, the methodology of the macroscopic column experiments, the obtained macro results and shortcomings, the need for research at the microscopic pore scale, the mechanical interactions between particles, fluids, and media grains as well as the main mechanisms of particle capture, and then we show the results of the microscopic scale research and shortcomings.

In Chapter 2, we describe the setup of the visualization experiment and its validation. First, we describe the assembly of the experimental setup, the physical parameters of the fluids employed, particles and porous media, and the operational steps of the experiment. The visualization allows us to obtain a series of images of the settling of particles. Then, we present the steps and algorithmic principles for importing the images into the software FIJI [20] and using Trackmate [21] for particle trajectory detection. Then, using the corresponding time series, we describe how to further compute the particle dynamic characteristics, including particle velocity, travel time, particle number counts, and particle concentration. Finally, we validate the accuracy of the above experimental setup by examining the static and dynamic settling of individual particles.

Based on the visualization experiment described in Chapter 2, we explore the settling kinematic properties of individual particles in Chapter 3. First, we analyze the motion traces as well as the velocity profiles of individual particles of different sizes falling in glycerin oil filling a confined medium made of two parallel plates with different gaps. Further, we indicate how the gap of the medium affects the settling motion of different particle diameters. Then, we analyze the motion characteristics of individual particles in porous media as well as the travel time. We compare the results for different particle diameters and different media structures and give the effects of both finally.

In Chapter 4, we gradually increase the number of particles injected and observe the settling motion characteristics of the particle population within the medium and their corresponding travel times. Also, as the number of particles increases, clogging occurs at

the pore throat of the medium. The number of particles entered, exited, and retained by each layer of the porous medium for different numbers of injected particles are further counted to establish the deposition profiles. To illustrate the process of clog formation, we directly track the motion behavior of the particle population within the pore space (including their velocity and moving direction) to explain the occurrence of clogging at the entrance and in the interior of the medium. Then, we seek a better description of the dynamic clogging process by quantifying the particles entering, leaving, and the cumulative concentration of particles in the pore space, as well as the contacts between particles and pillars. Ultimately, we give probability distributions for clogging under different conditions.

Chapter 1

The state of art on clogging

1.1 Introduction

While suspension flow goes through porous media, the particles transported by the liquid would plug the pore channel of the medium, reducing the permeability and increasing the pressure drop across medium [6], [13], [22]. Such transportation and clogging phenomenons refer to many fields like wastewater treatment, oil production [5], bank erosion [23], permeable pavement [7], aquifer drainage [1], farmland irrigation, and so on, in which clogging (or non-clogging) would gradually reduce initial working efficiency of filter medium and lead to economic loss.

Aquifer storage oil production [5] and recovery (ASR) is a widely used technique to store stormwater runoff and treated wastewater for future use. However, the clogging of the recharge system is the main problem of ASR application, which could lead to quick failures of ASR operation [1], [24]. During drilling operations, fluid is laterally filtered into the surrounding permeable rock formation. Reservoir damage occurs when particulate matter from the drilling mud, such as drill solids, invades the reservoir rock, plugging pores and forming an internal filter cake. The permeability of the reservoir rock is significantly compromised, resulting in a substantial reduction in oil production. [5] Moreover, the permeable pavement is a type of new sustainable urban drainage system for attenuation of runoff volumes, mitigation of heat urban islands, and reduction of transportation-related noise by the designed porous structure [25], [26]. As shown in Fig.1.1, it has been showed that suspended sediments and pollutants carried by the runoff could clog the pore throat and hence, decrease the infiltration rate of the system partially or fully, thereby weakening its functions [3], [7], [25]–[29]. It is important to avoid clogging occurrences for permeable pavement for a long-time service. In addition, even if clogging happens, it is still necessary to evaluate the clogging state for scheduling the maintenance (like sweeping, vacuuming, sonication, or combination among them) or replacement activities [30].

Investigations in various fields of transport of fine particles in porous media have shown

Figure 1.1: Standing water over PICP (permeable interlocking concrete pavers) section after progression of clogging [7].

that the desired results of particle transport are different or even opposed in different situations. In the case of wastewater filtration, the goal is to trap particles to prevent their transport. Thus, the deposition of particles is a positive goal aimed at improving water quality. In contrast, in petroleum engineering, to prevent formation damage and maintain field productivity, it is desired that the particle flow remains enough permeable to avoid pore blockage. Active anti-clog design and controlled clog development can maximize the workability as well as the economic benefits of porous media. But this requires an in-depth understanding of the clogging mechanism, which tends to describe the probability of clogging occurrence, clogging depth inside medium [11], [12], the deposition profile of suspended particles [10], [12], the pressure drop across medium [8], the reduction in permeability [8]–[10] under certain conditions (including the characteristics of particle, fluid and porous medium). Until now, a large number of studies on a macroscopic scale have revealed a wealth of transportation and clogging phenomena. However, there is still a lack of information on the mechanical interactions of particles, fluids, and media structures at the pore scale, which in turn limits our understanding of the clogging phenomenon.

1.2 Macro studies on filtration

1.2.1 Measurement and experimental method

Clogging is not an inherent property of the porous media itself, but rather a process that results in changes in variables specific to the porous media [4]. This requires that these variables should be defined in a field or laboratory setting to determine or quantify the extent of clogging. They are typically indicated by measuring the clogging depth and deposition profiles in the medium, or by indicating clogging through hydraulic conductivity, pressure drop, and effluent concentration. All of these elements can be linked to the changes in medium porosity caused by the clogging process. However, since it may be difficult to measure changes in porous media properties directly, indirect variables such as deposition profile, permeability, and pressure drop are useful in assessing the clogging process.

For the experiment setup, researchers usually use column experiments to simulate the filtration behavior of suspensions in porous media. As shown in Fig.1.2, typically, the column experimental apparatus consists of a column vessel filled with the porous medium (e.g., sand, gravel, or soil) required for the study. The top of the column is equipped with an inlet for adding the suspended liquid for the test. The bottom of the column is equipped with an outlet for collecting the filtered fluid. During the experiment, the flow rate and pressure of the fluid and the concentration of the suspension at the outlet can be monitored by various instruments. Column experiments are favored for their ability to provide information about the macroscopic filtration behavior of porous media under relatively simple and controlled laboratory conditions.

1.2.2 Basic properties of clogging

Physical clogging process

In general, the degree of clogging varies spatially. This is because the heterogeneity of the medium structure further leads to different particle concentration distributions and fluid flow rates, and therefore to different clogging probabilities [13]. Also, the degree of clogging varies with time [4]. Initially, particle clogging is just occurring, when it has little effect on the permeability performance of the medium. As the clogging continues to develop, more particles are trapped. At this point, the permeability decreases significantly and the deposited particles accumulate toward the surface of the media. Finally, the clogging

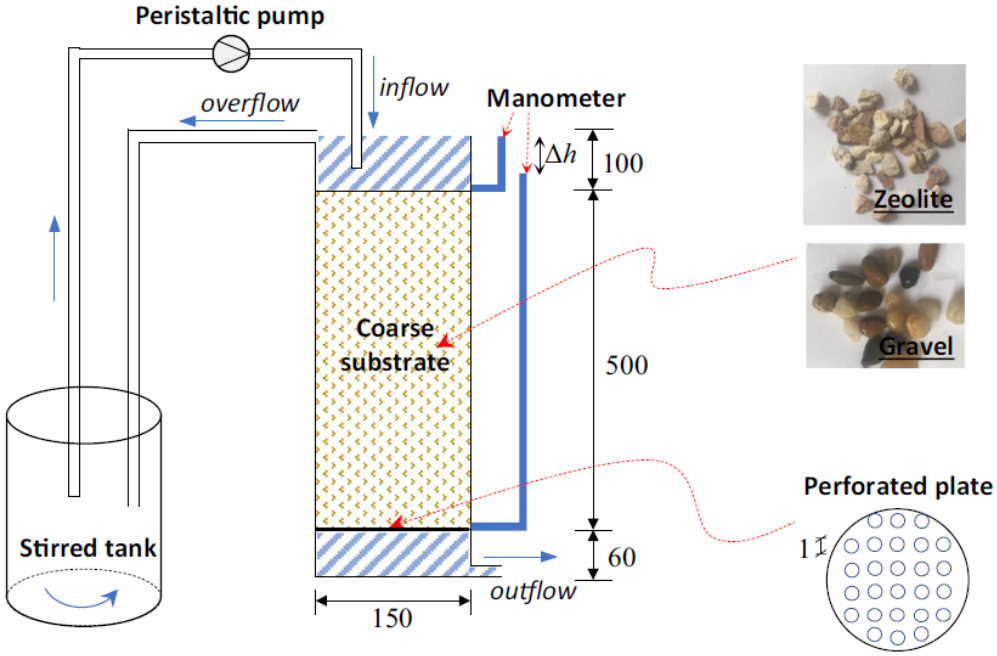

Figure 1.2: Typical column experiment setup [11].

reaches its maximum state and no more particles are deposited.

The clogging depth and deposition profile

When the spaces between the grains that build up the porous medium are wide, suspended particles tend to penetrate deeply. Over time, the formation of bridging particles decreases the size of these interstices, thus reducing the ability of particles to penetrate further. When the size of these gaps decreases to the point where they cannot hold more particles, the depth of the blockage stabilizes. Therefore, a critical clogging depth can be observed in column experiments [11], [12], which show the maximum intrusion depth of fine particles into the coarse medium. Besides, it is reported that the proportion of fine particle deposits in a homogeneous matrix with internal clogging shows an exponentially decreasing profile [12]. This means that the amount of fine particle deposits decreases rapidly with depth.

The type of clogging

Based on the distribution of particle deposition profiles, clogging is roughly categorized into: surface clogging, internal clogging, and unimpeded static permeation [4], [8], [12].

- Surface clogging
  While the size of particles is greater than the pore size of porous media, the particles will plug the pores directly. Thus, the particles are mainly retained at the surface of the porous medium. Surface clogging is characterized by a rapid decrease in filtration efficiency because the clogging layer restricts the flow of fluid. This type of clogging is relatively easy to resolve by physical cleaning or backwashing.

- Internal clogging
  Internal clogging occurs in the internal pores or channels of the porous media. This form of clogging involves smaller particles relative to pore size that can pass through the surface layer and enter the internal structure of the media. Once these particles collect in the pores, they reduce permeability efficiency and increase resistance through the media. Internal clogging may be more difficult to resolve through conventional cleaning methods because the clogging material is located deep inside the media.

- Unimpeded static permeation
  Unimpeded static permeation occurs when the pores of the media are sufficiently larger than the size of the particles, which will allow the particles to pass directly through the pores without clogging occurring.

1.2.3 Factors affect clogging

It has been shown by the numerous column experiments studies that suspension injection velocity, concentration, medium grain size and suspended particle size are the main factors affecting the clogging phenomenon [8]–[10], [31]. Here, we mainly introduce the results on particle size ratio and concentration.

Particle size ratio

The size of particles relative to the pore size of porous media (or medium grain size) is widely recognized as an important indicator for clogging phenomena [12]. The ratio

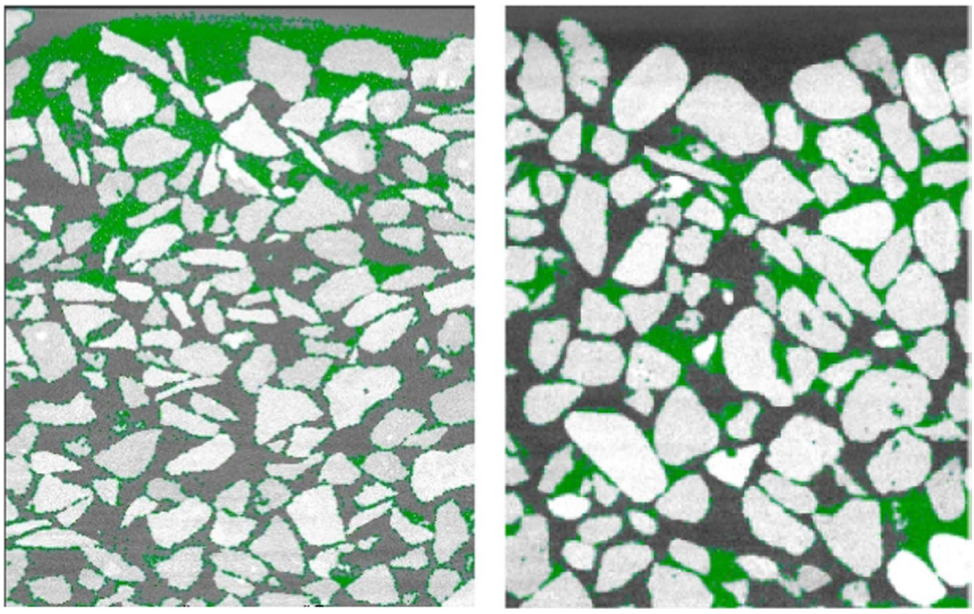

Figure 1.3: The slice of deposition profile in a column experiment extracted by the X-ray scanning; the green part represents the deposited fine particles; the white part represents the gravel medium; black part represents the liquid among gravel grains [11]. Besides, the left figure shows the surface clogging and the right shows the internal clogging.

between them is widely used as one of the parameters to demonstrate clogging, which is called particle size ratio (α):

$$\alpha = \frac{d_p}{D_f} \tag{1.1}$$

or:

$$\alpha = \frac{d_p}{e_p} \tag{1.2}$$

Where d_p is suspended particle size, D_f is the medium grain size, and e_p is the pore size of the porous medium. In our study, we use Eq.1.2 to calculate the α.

α can be larger than 1 or smaller than 1. In the case of $\alpha > 1$, particles will be blocked directly. It showed while α is close to 1, the pores inside the medium are narrow relative to the particle size. This would block particles easily at the surface and the formed clogging layer will further filter the subsequent particles. While decreasing α, the particles tend to deposit inside the medium. Once the clog happens, the subsequent particle will deposit and clog the whole medium. Sometimes, the temporarily retained particles can be destabilized and a balanced state between clogging and filtration could be realized in the end [11]. Continuing decreasing α, particles can pass through medium without clogging

[8], [10]–[12].

Table.1.1 shows some critical values identifying clogging occurrence under specific conditions. The formation of clogging is mainly attributed to larger suspended particles as well as smaller media particles. Therefore, $D_{15,f}$ and $d_{85,p}$ were used as indicators in many studies, in which the $D_{15,f}$ and $d_{85,p}$ denote the size corresponding to 15% and 85% of the cumulative distribution of particle sizes. There are some differences in these critical values due to different experimental conditions. Huston et al. proposed that the adjusted particle size ratio ($D_f/d_p c_u$, c_u is the uniform coefficient.) can better predict the occurrence of clogging through regression analysis of a large amount of experimental data. This reflects that in clogging studies, it is necessary to consider not only the particle size and distribution but also the complexity of the internal structure of the substrate mixture, as well as the distribution and interaction of pores on different scales. The occurrence of clogging further affects the maximum depth of penetration that the particles can reach, which would in turn lead to different deposition profiles [12].

Table 1.1: The threshold of particle size ratio for identifying the clogging occurrence

Authors	Form of indicator	Value
Sakthivadivel and Einstein [32]	D_f/d_p	20
Gibson et al. [33], [34]	$D_{15,f}/d_{85,p}$	15.4
Brunke.[35]	$D_{15,f}/d_{85,p}$	5
Valdes et al. [36]	e_p/d_p	4 or 5
Tang et al. [11]	$D_{50,f}/d_{50,p}$ and $D_{50,f}/d_{50,p}c_u$	15, 12 for zeolite medium.
Tang et al. [11]	$D_{50,f}/d_{50,p}$ and $D_{50,f}/d_{50,p}c_u$	12, 10 for gravel medium.
Huston et al. [12]	$D_f/d_p c_u$	27

Concentration

Fig.1.4 shows permeability decline over time at different concentrations, which is measured by Du et al.[8]. They concluded the concentration of the suspension affects the rate at which permeability decreases, with higher concentrations leading to faster reductions in permeability compared to lower concentrations. An increase in concentration causes more suspended particles to enter the interior of the medium per unit of time, which in turn leads to rapid onset and development of clogging [9], [10]. Also, it showed the effect of

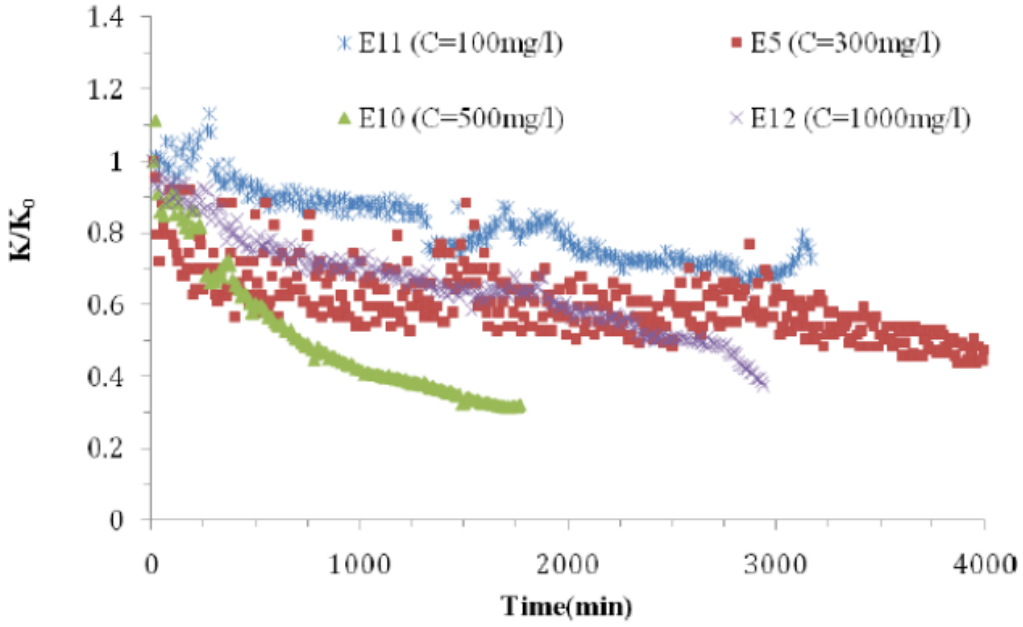

Figure 1.4: Decline of permeability (K/K_0) over time at different suspension concentration; K_0 is the initial permeability; K is the permeability with time; $E11$, $E5$, $E10$, and $E12$ are the test sample with a different concentration in the study of Du et al [8].

concentration on clogging is dependent on the particle size ratio [9]. When the suspended particles are smaller, it leads to a greater depth of penetration; when the particles are larger, it leads to more particles being deposited on the surface. Besides, although the concentration of suspended particles plays a role in the transient phase of the clogging process, it is reported that fully clogged substrates exhibit similar permeability [4].

1.3 Involved forces during filtration

The initiation of a clog is the result of complex forces interaction involved during the filtration process. Following introduce the related forces that affect the transportation and deposition of suspended particles [14].

1. Gravity and buoyancy force:

$$F_{net} = \frac{4}{3}\pi \left(\frac{d_p}{2}\right)^3 (\rho_p - \rho_l)\, g \tag{1.3}$$

F_{net} is the sum of gravity and buoyancy force, g is the gravity acceleration, ρ_p and ρ_l are the density of particle and liquid.

2. Drag force ($\vec{F_d}$):
   When the particle moves relative to the fluid, drag force is generated due to the friction between the particle surface and the surrounding fluid, as well as the different pressure distributions around the particle caused by fluid flow. This force is opposite to the direction of the particle's velocity. For a small sphere moving under low Reynolds number conditions, the drag force (or Stokes force) can be expressed by the following formula:
   $$\vec{F_d} = 6\pi\mu r\left(\vec{v_f} - \vec{v}\right) \tag{1.4}$$
   r is particle radius, $\vec{v}$ is particle velocity, $\vec{v}_f$ is the fluid velocity, μ is liquid viscosity.

3. Inertial force:
   Inertial force describes the tendency of a particle to maintain its current state of motion ($\vec{F_i}$):
   $$\vec{F_i} = \frac{4}{3}\pi\left(\frac{d_p}{2}\right)^3 \rho_p \frac{d\vec{v}}{dt} \tag{1.5}$$

4. Lubrication force:
   It occurs while a particle slides along the wall of the porous medium due to the viscous resistance of the fluid film:
   $$\vec{F_l} = 6\pi\mu\left(1 + \frac{d_p}{2h}\right)\frac{d_p}{2}\vec{v}_f \tag{1.6}$$
   h is the thickness of the fluid film.

5. Contact force:
   Due to the large inertia of the particles and the blockage of the medium to the movement of the particles, contact forces are generated between the particles or between the particles and the medium. Calculating the contact forces between particles is a key step in the kinetic simulation of multi-particle systems (e.g., particle flow). The contact forces between particles usually include both positive (normal) and tangential forces, and the calculation of these forces needs to take into account the physical properties

of the particles, the interaction forces between the particles, and the adhesion forces that may be present [37].

Normal force is the force between two particles along the direction normal to their point of contact. One of the most commonly used models is the Hertz contact force model for elastic contact. The Hertz model calculates the normal force based on the elastic modulus of the particles, Poisson's ratio, and the amount of overlap between the particles [38], [39]. The basic form of the Hertz model is shown below:

$$F_n = \frac{4}{3} E^* \sqrt{r^*} \delta^{3/2} \tag{1.7}$$

E^* is the equivalent modulus of elasticity. r^* is the equivalent particle radius. δ is the amount of overlap between particles or particles and medium grain. The equivalent modulus of elasticity and the equivalent radius can be calculated from the physical properties of the particles.

The tangential force is the force generated when the particles slide or roll on the contact surface. Commonly used models include the Mindlin and Deresiewicz model, which takes into account sliding friction and the roughness of the particle surface. The calculation of the tangential force usually depends on the normal force, the coefficient of friction, and the relative sliding distance between the particle surfaces.

$$F_t = \min\left(f_s F_n, k_t \delta_t\right) \tag{1.8}$$

f_s is the coefficient of friction, k_t is the tangential stiffness, δ_t is the tangential displacement.

1.4 The behaviors of particle capture

During filtration, the gradual deposition of particles within the medium can lead to eventual clogging. Here, we describe the behavior of medium-capturing particles under different mechanical forces dominating the process [6], [14]. In practice, we often superimpose the particle capture performance due to different mechanical forces to estimate the overall particle capture efficiency in complex conditions [6], [22].

(1) Sedimentation

If the particle's density is significantly greater than that of fluid, indicated by SG (equal to ρ_s/ρ_l), they would move at a constant velocity relative to the fluid along the gravity direction, which make particles deviate from streamline and be settled out [6]. According to the Stokes law, the terminal sedimentation velocity (or Stokes velocity) of a small particle in the liquid can be estimated as:

$$v_s = \frac{2}{9}\frac{r^2 g\left(\rho_{\mathrm{p}} - \rho_l\right)}{\mu} \tag{1.9}$$

And the dimensionless Archimedes number (Ar) is used to evaluate this behavior [15]:

$$Ar = \frac{\text{Terminal velocity}}{\text{Flow velocity}} = \frac{g d_p^2\left(\rho_p - \rho_l\right)}{\mu v_f} \tag{1.10}$$

(2) Inertial mechanism

By calculating the ratio between the response time of the particle and the response time of the fluid field, i.e., St, we can estimate if the particle will follow the streamlines while there is a change in flow field [15].

$$St = \frac{\rho_p d_p^2 v_f}{18\mu D_f} \tag{1.11}$$

When St is greater than 1, the response time of the particle is longer than the change time of the fluid field. This means that the particles cannot adapt quickly to the change in fluid velocity due to their higher inertia, so they tend to continue moving along their original trajectory even though the direction of the fluid flow has changed, as shown in Fig.1.5. At high Stokes numbers, the particles may not follow the fluid streamline closely, especially in regions where the fluid is changing rapidly. When St is less than 1, the response time of the particles is shorter than the change time of the fluid field. This indicates that the particles can quickly adjust their velocity to match the change in velocity of the surrounding fluid, and thus they can closely follow the fluid streamline. At low Stokes numbers, the motion of the particles in the fluid is more governed by the fluid dynamics and better reflects the fluid flow characteristics.

Tien et al. [40] demonstrated that a critical threshold exists for the Stokes number: below this value, the deposition of particles through inertial impact becomes negligible. J.S. Andrade Jr et al. [41] numerically investigated the capture efficiency

under the influence of geometry and inertial effects. In the absence of gravity (in Fig.1.6 (a)), they found a typical second-order transition between non-trapping and trapping of particles that can be expressed as $\lambda \sim (St - St_c)^{\kappa}$, with an exponent $\kappa \approx 0.5$, where St_c is the critical Stokes number. For the particles considering gravity (in Fig.1.6 (b)), it will decrease the value of St_c to 0 and change the κ to 1. However, the three assumptions they made lead to certain limitations in the results: the particles are point-like; the influx of suspended particles is so small that the fluid phase is not affected by changes in the particle volume fraction; particle-particle interactions are negligible.

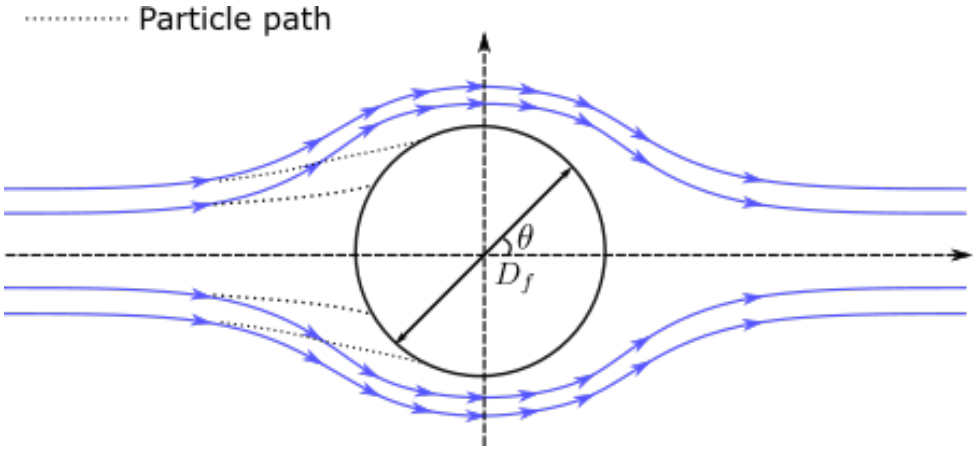

Figure 1.5: Inertial mechanism[37]

(3) Hydrodynamic action

Fluid flow in the pores of porous media has laminar characteristics, similar to the Poiseuille flow observed in capillaries. In each pore space, the velocity gradient varies, starting at zero at the grain surface boundary and peaking towards the center of the pore space. However, due to the complex nature of the pore space with expansion and contraction, the velocity distribution deviates from the typical parabolic shape of Poiseuille flow. This deviation is attributed to the complex geometry of the pore space, which makes the flow pattern more irregular [6].

Within the pore space, the velocity gradient creates a shear field. In the presence of a uniform shear field, the spherical particles rotate, resulting in a spherical flow pattern around them. This rotation drives the particles through the shear field. However, in a filter pore, the shear field is inhomogeneous and the motion of the particles will be destabilized by different shear forces and will not follow a predictable

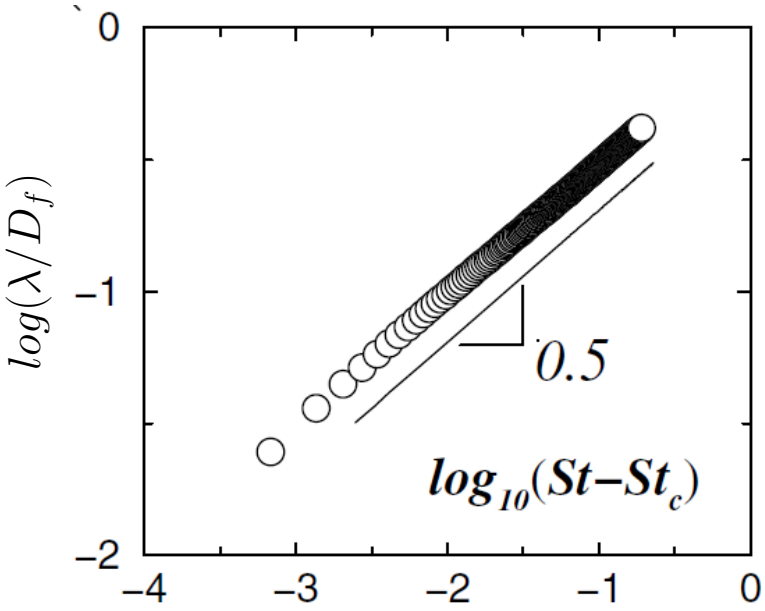

(a) Without gravity

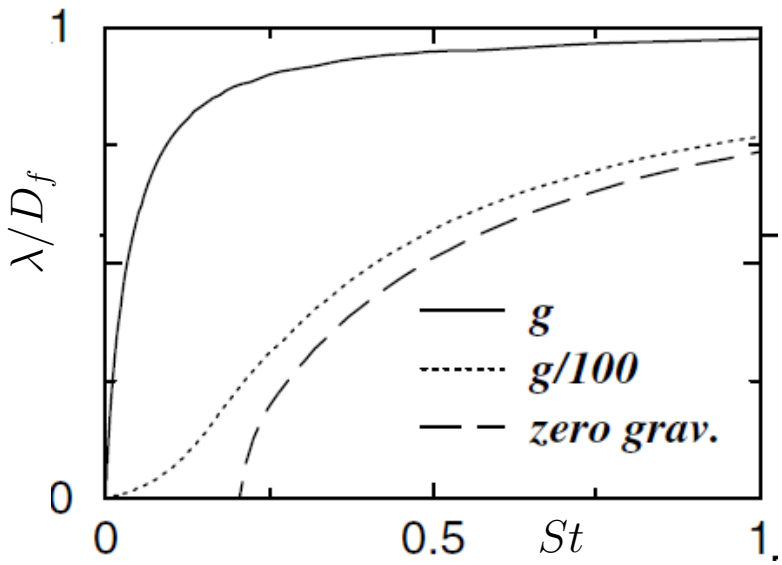

(b) With gravity

Figure 1.6: The capture efficiency with Stokes number without and with gravity [41].

path. Additionally, when the particles deviate from their spherical shape, additional asymmetric forces are encountered that push the particles across the flow line in a more unpredictable manner. This complexity is further amplified if the particles can deform, leading to even more unpredictable and irregular motion: a random, drifting motion across the streamlines, and, in turn, contact with the collector surface. Although much effort has been invested in the theoretical study of particle motion in fluid shear fields, the complex geometry of the filter pores still makes theoretical analysis difficult to implement [6].

(4) Straining

While particles are large enough compared with the size of the pore throat, they will be strained and clog the pore directly. Or while the many particles are transported and stopped simultaneously at the pore throat, they would accumulate, form a particle bridge and plug the pore in the end. These phenomena will keep working throughout the whole filtration process and affect the development of the process in time [6], [13]. As shown in Fig.1.7, 0.154 is the limit value for one particle in a purely geometric capture, greater than which the particle will be blocked. For the configuration of three and four particles, the threshold values are 0.10 and 0.082 respectively [42]. These limits obey to the following relations respectively:

$$\frac{d_p}{D_f} = \frac{2}{\sqrt{3}} - 1 = 0.154 \tag{1.12}$$

$$\frac{d_p}{D_f} = 5 - \sqrt{24} = 0.101 \tag{1.13}$$

$$\frac{d_p}{D_f} = \frac{1}{3}\left[1 + \frac{2}{\sqrt{3}}(1 - \sqrt{1+\sqrt{3}}\right] = 0.082 \tag{1.14}$$

1.5 Micro studies on filtration

Many visualization techniques are used to obtain clogging information at the pore scale, such as high-speed cameras, x-ray inspection, and observation of different slices of a sample [13]. As a result, researchers have observed pore-scale clogging phenomena under different

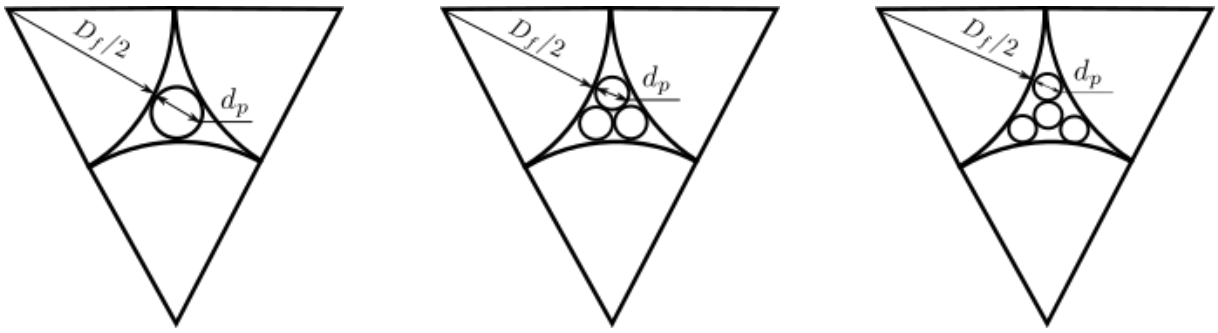

(a) 0.154 (b) 0.101 (c) 0.082

Figure 1.7: Configuration of straining [37], [43]

conditions, which in turn demonstrates the various factors that influence the occurrence of clogging.

1.5.1 Micro clogging process

As shown in Fig.1.8, Liu et al. [15] explained schematically that the collision between particles and medium grains induced by the large inertial or sedimentation would retard the particle motion, especially where there is flow that curves and changes in flow velocity. This would lead to the accumulation of particles and an increase in local concentration. High localized concentrations, especially at pore constrictions, will promote the formation of particle bridges. This is the reason why they do not see the clog occurrence for 5 μm, which is due to the small inertial effect compared with 10 μm. Frey et al. [17] also observed curvature and stagnation points in the flow line create low-velocity regions that are more likely to accumulate particles. When the flow is predominantly in one direction (anisotropy ratio of 0, as showed in Fig.1.9 (c)), the low-velocity regions and curvature changes in a particular direction will become primary locations for deposition, resulting in deposition growing upstream in that direction. Accumulation of particulate deposits will alter the local flow field, making previously low-velocity regions more pronounced, further promoting deposition. This process is self-reinforcing and results in deposition growing along a specific path. Non-uniform anisotropy ratios lead to fluid flow with different properties in different regions, resulting in more complex deposition patterns in pore media. The deposited particles under different anisotropy ratios are shown in Fig.1.9.

Bacchin et al.[16] observed clogging in different configurations: straight microchannels, and aligned and staggered square pillars. In Fig.1.10, for a straight microchannel, the

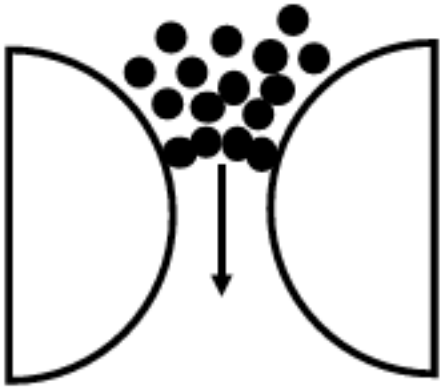

Figure 1.8: Sketch of the retardation-accumulation bridging process [15].

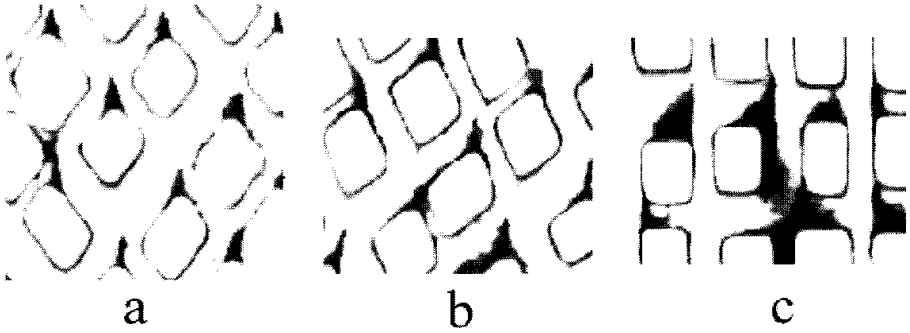

Figure 1.9: Experimental deposits with different anisotropy ratio, the flow is from top to bottom [17]; anisotropy ratio is related to the average direction of the main flow in the etched network: while anisotropy ratio equals to 0, meaning the fluid flow is mainly in one direction, as shown in (c); anisotropy ratio equals to 1, meaning the fluid flow is the same in all directions in the etching network, as shown in (a); anisotropy ratio in (b) is 0.5.

particles would accumulate on pillars at the entrance and clog the pores eventually. For staggered pillars, particles would deposit due to the blockage of the medium and plug pores inside gradually, then this behavior progresses upward, leading to a dense surface deposit. For aligned pillars, the initial particle depositions would produce the flow at the dead zone inside the medium. Then the particles can be captured continuously and clogging will develop inside due to the curved streamline as staggered square pillars.

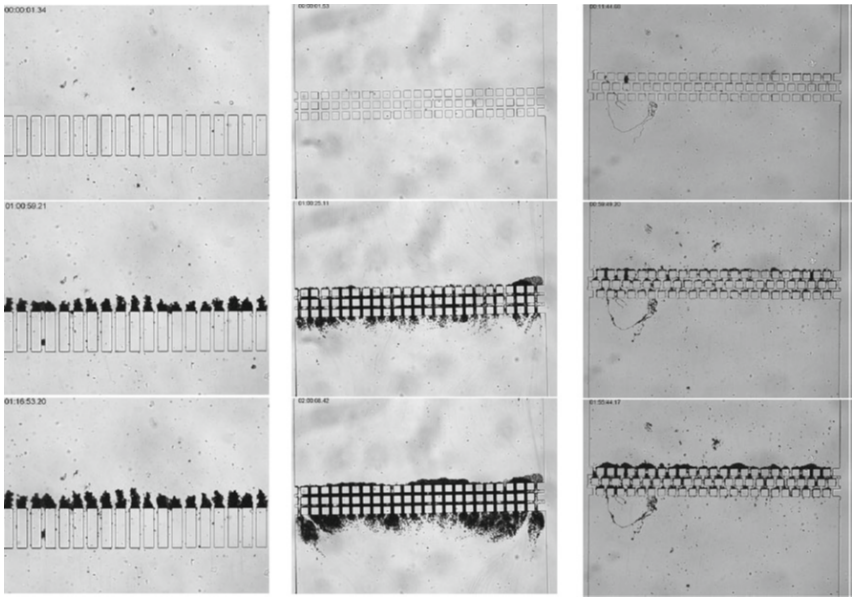

Figure 1.10: The influence of porous medium structure on clogging [16].

1.5.2 Dynamic deposition profile

By using Nuclear Magnetic Resonance detection techniques, Gerber et al. [19] observed the dynamic deposition process of non-buoyant particles (50 μm with the same density as carrying fluid) due to size exclusion effects only (particles are physically blocked in channels in porous media) under the laminar flow condition and random close beads packing medium. As shown in Fig.1.11, they saw the particles deposited at any depth of the medium increase linearly with time. They explained that even though parts of the interior of the medium were clogged, the fluid would bypass the area where the clogging occurred and thus continuously transport particles into the depth of the medium. And when the volume fraction at the inlet ($x = 0$) reaches about 0.45 ± 0.05, most particles begin to deposit on the surface of the medium, i.e., caking.

1.5.3 Clogging probability

The mechanism of particle bridge formation at pore constriction (such as Fig.1.8) has likewise attracted the interest of many researchers. It has been studied in the simplest case by observing the particle flow passing through a single orifice [18], [36], [44], as shown in Fig.1.12. The results show that the formation of particle bridges is independent of time, and many factors affect the clogging occurrence [18], [36]. Besides, it was found that the

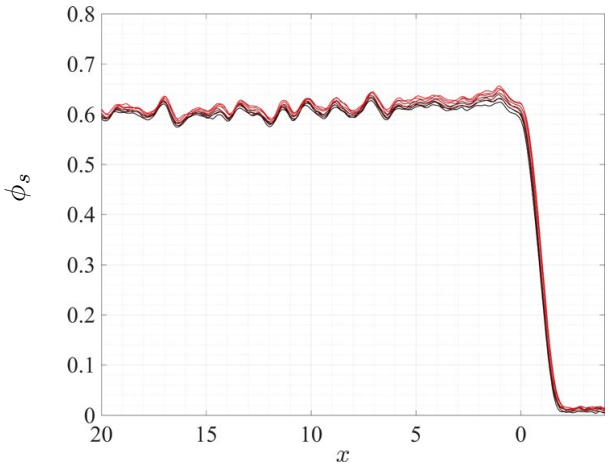

(a) $\alpha = \frac{d_p}{D_f} = 0.067$

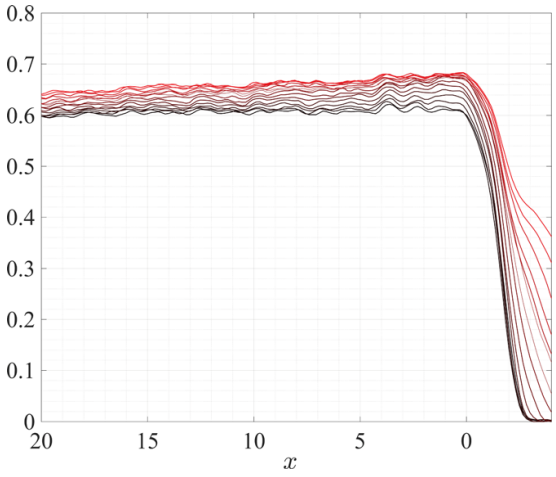

(b) $\alpha = \frac{d_p}{D_f} = 0.11$

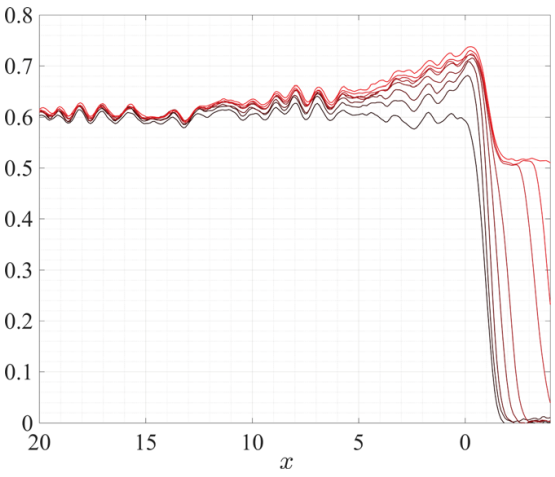

(c) $\alpha = \frac{d_p}{D_f} = 0.13$

Figure 1.11: The deposition profile over time (arranged from bottom to top) with successive injections of the same number of suspended particles (5.0×10^5) in bead packing media under different α values; The lowest profile (darkest color) represents the initial state, in which ϕ_s in the medium is about 60% [19].

probability of clogging would be exponentially related to the particle size ratio (α) [45]. Gella et al. [18] further independently analyzed the effect of the kinematic properties of the sphere particle flow on the occurrence of clogging by controlling the outflow velocity (discharge) at the outlet. They found that at higher outflow velocity (large discharge), a more complete continuous flow was observed, and therefore the probability of clogging was lower. When the outflow velocity was small (small discharge), the particles tended to stay at the outlet, causing the flow to become intermittent - the particles sometimes flowed and sometimes stopped, thus leading to a higher probability of clogging. Therefore, the improved clogging probability formula considering the influence of particle flow is [18]:

$$P = (a + bv_o)^{-(e_p/d_p)^2} \tag{1.15}$$

Where v_o is the velocity that particles flow out when particles accumulate at the orifice, a reflects the effect of particle inertia and b reflects the effect of particle velocity on clogging. This formula was further validated to apply to a wide range of scenarios, such as free settling, for different particle diameters.

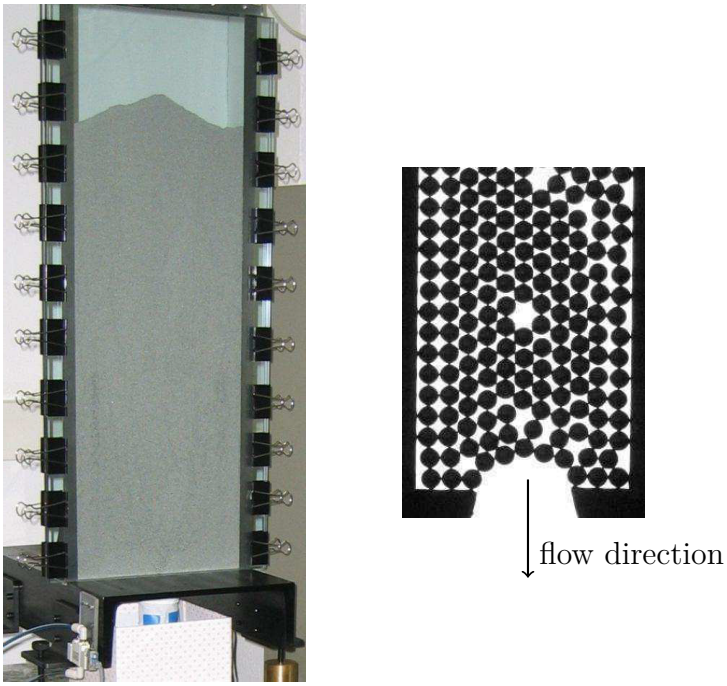

Figure 1.12: Left: the two-dimensional silo employed in experiment; Right: the schematic diagram of silo [44].

1.6 Conclusion

Transportation of particles and clogging phenomena are involved in many areas of civil engineering. Eventual clogging affects the working performance of porous media and their economy. Therefore, there is a great need for a more in-depth study of clogging phenomena. Classical column experiments can better reflect the rich clogging phenomenon under different conditions, such as the clogging process, the deposition profile, the effect of particle size ratio, and the suspension concentration. However, the lack of information on particle deposition inside the column, the complex mechanical interactions between particles, fluids, and media, and the heterogeneity of various parameters in the clogging process lead us to still have difficulties in quantitatively describing or predicting the clogging phenomenon. This promotes the study of clogging at the microscopic scale. For suspended particles, the transportation of particles in the pores mainly involves the effects of gravity, buoyancy, inertia, drag, lubrication, and contact forces. Under the dominance of different forces, particle sedimentation, particle inertia, fluid forces, and straining will cause the particles to continuously deposit on the media grains and form clogs. Through visualization techniques, more information on the pore scale is presented. The results show that the inertia of the particles plays an important role in the deposition of particles and the development of clogging, especially at the constriction of the pore throat (change of flow field). Also, the structure of different media leads to different processes of clog formation. The detection of dynamic deposition processes for non-buoyancy particles and the study of the probability of clogging at a single orifice provide models to quantitatively describe clogging at the pore scale. More studies can further refine these models by exploring the effects of additional variables (e.g., media scale, particle size) or considering more complex flow patterns.

Therefore, in this study, we explored the free settling characteristics and ultimately the clogging behavior of different particle diameters and particle numbers in different media structures by using image detection techniques, further to reveal their effects.

Chapter 2

Visualization experiment setup

2.1 Introduction

In this study, we chose to visualize and analyze the behavior of particles at the pore scale. This chapter focuses on describing in detail the visualization experimental equipment as well as the subsequent image detection techniques and data processing. First, we describe the experimental setup, including the assembly of the equipment, the physical parameters of fluids, particles, and the porous medium involved in the experiment, the parameters of the equipment, and the execution procedure of the experiment. The experimental setup allows us to acquire a series of images of the dynamic settling of particles. Then, we describe the steps and algorithm principles for importing the images into the software FIJI [20] and using Trackmate [21] for particle trace detection. Next, with the obtained particle trace information and the corresponding time series, we describe how to further calculate the particle dynamics characteristics, including particle velocity, travel time, particle number counting, local area concentration, contact among particles or between particles and pillars. Finally, the accuracy of the above experiment setup is verified by detecting the static and dynamic processes of individual particles.

2.2 Experimental Setup

2.2.1 Experiment device

To observe the behavior of the particles in the porous media, we established a visualization experimental setup to record the images of the particle motion. As shown in Fig.2.1, a transparent container was placed on a horizontal experimental platform. The length (in the x-axis), width (in the y-axis), and height (in the z-axis) of the container are 44 cm, 6 cm and 20 cm respectively. Inside the container, we will reproduce the particle settling phenomenon under different conditions by setting different media (confined media of two

plates or porous medium in liquid) and changing the particle number and size. The liquid, the media setup as well as the physical parameters of the particles, and the injection method are described in detail in the following sections. A camera system is placed in front of the container (in the y-axis direction) to record the settling motion of the particles in the plane of the x-z axes. At the same time, a light source positioned at the back is used to enhance the contrast between the black-painted particles and the white background (due to the transmitted light), thereby facilitating particle detection. Simultaneously, a white translucent paper was placed between the container and the light source to reduce the intensity of the light. The container (the observation area for particle settling), the camera, and the light source need to be set at the same height. The camera and the light source need to be aligned and perpendicular to the container. This could prevent obstacles in the container from creating shadows in the image due to light deviations, which in turn affects the subsequent image detection.

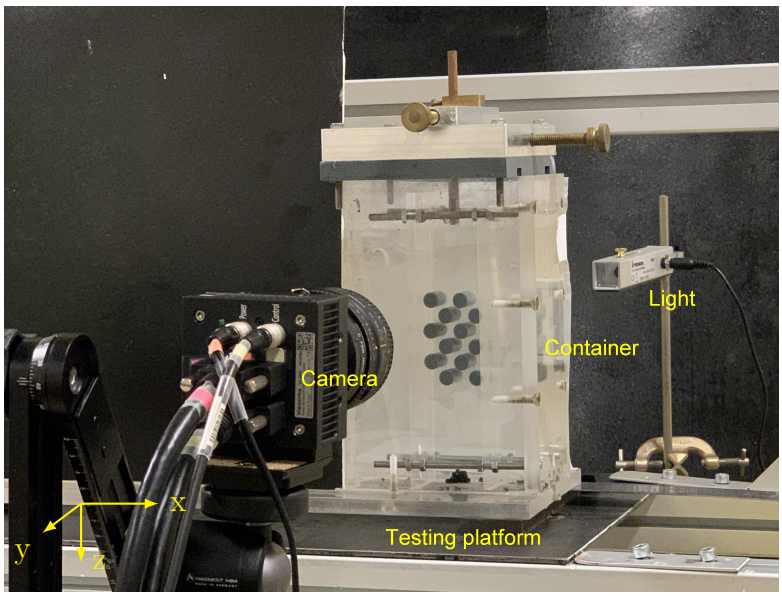

Figure 2.1: Experimental device.

2.2.2 Fluid employed in experiment

After some preliminary experiments, we chose to use a mixture of water and glycerol instead of water to increase the viscosity of the fluid and thus reduce the settling velocity of the particles. Also, this allows us to reduce the frame rate. In this study, we used the

model proposed by Cheng et al. [46] to calculate the density and dynamic viscosity of the mixtures for different ratios of water and glycerol as well as temperature. In Eq.2.1, μ is the dynamic viscosity of the mixture. The subscripts w and g in μ_w^γ and $\mu_g^{1-\gamma}$ denote water and glycerol.

$$\mu = \mu_w^\gamma \mu_g^{1-\gamma} \tag{2.1}$$

The γ is the weighting factor varying from 0 to 1, which is calculated by Eq.2.2. γ is the function of glycerol fraction in mass (C_m).

$$\gamma = 1 - C_m + \frac{abC_m\,(1 - C_m)}{aC_m + b\,(1 - C_m)} \tag{2.2}$$

$$C_m = \frac{\rho_g V_g}{\rho_g V_g + \rho_w V_w} \tag{2.3}$$

The a and b are the fitted coefficients based on the measured data, which are the function of temperature (T, in units of $^\circ C$).

$$a = 0.705 - 0.0017T \tag{2.4}$$

$$b = (4.9 + 0.036T)a^{2.5} \tag{2.5}$$

In addition, the density of the mixture is estimated by Eq.2.6:

$$\rho_l = \rho_g C_m + \rho_w\,(1 - C_m) \tag{2.6}$$

where ρ_g and ρ_w are the densities of pure glycerol and water respectively given by:

$$\rho_g = 1277 - 0.654T \tag{2.7}$$

$$\rho_w = 1000\left(1 - \left|\frac{T-4}{622}\right|^{1.7}\right) \tag{2.8}$$

The glycerol fraction in volume C_v is given by:

$$C_v = \frac{V_g}{V_g + V_w} \tag{2.9}$$

Fig.2.2 and Fig.2.3 show the variation of dynamic viscosity and density with the change of glycerol fraction in volume (C_v, Eq.2.9) at the temperature of $20^\circ C$ based on the pre-

sented model. It is observed that in the interval 0.7 to 1 of C_v, the viscosity increases rapidly. Whereas in the interval 0 to 0.7, the viscosity increases very slowly, which means that adding glycerol at this point does not have a great effect on the viscosity of the liquid mixture. The density curve shows that as the glycerol content increases, the density of the liquid mixture gradually increases until it reaches the density of pure glycerol.

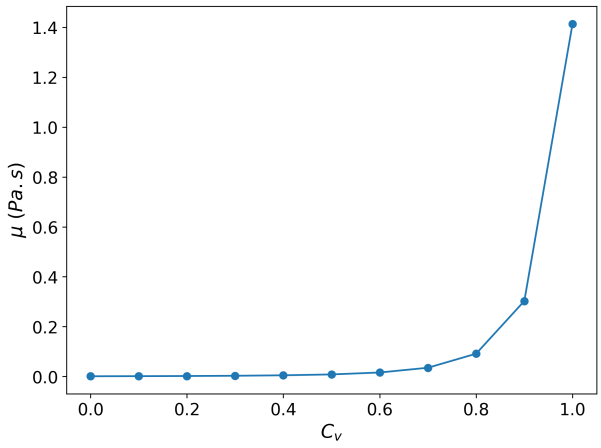

Figure 2.2: Dynamic viscosity of liquid mixture with various of volume fraction of glycerol (C_v) for T =20°C.

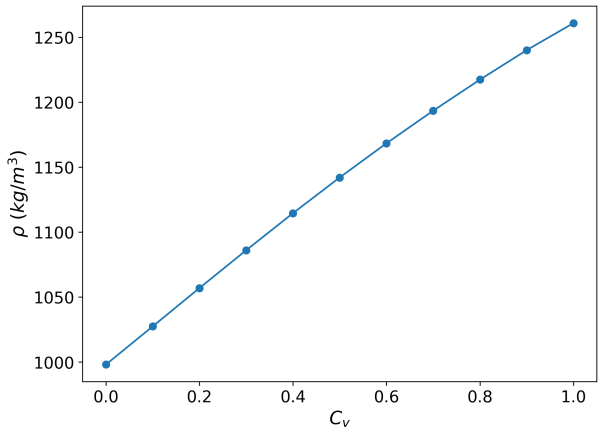

Figure 2.3: Density of liquid mixture with various of volume fraction of glycerol (C_v), T =20°C.

Fig.2.4 and Fig.2.5 show the variation of dynamic viscosity and density of the liquid mixture with temperature while $C_v = 0.65$. It can be seen that as the temperature gets higher, the dynamic viscosity (μ) produces a large decrease. The temperature in the laboratory

is maintained between 20°C and 30°C. For estimating the temperature influence on viscosity during the day, we calculated the viscosity values for every 2°C interval based on the model. Then we could calculate the percentage change in viscosity per 2°C difference based on Eq.(2.10). Averaging the μ_ϵ at different T (from 20°C to 30°C in the interval of 2°C) yielded a mean of 5% under 2°C difference during the day.

$$\mu_\epsilon = \frac{\mu_T - \mu_{T+2}}{\frac{\mu_T + \mu_{T+2}}{2}} \tag{2.10}$$

μ_T is the viscosity of the liquid mixture at a temperature of T, μ_ϵ is the percentage change in viscosity of liquid mixtures in response to temperature fluctuations (2°C here).
Fig.2.5 shows that temperature produces a smaller effect on the density of the mixture, which changes by 1.1% when the temperature changes from 14°C to 36°C.

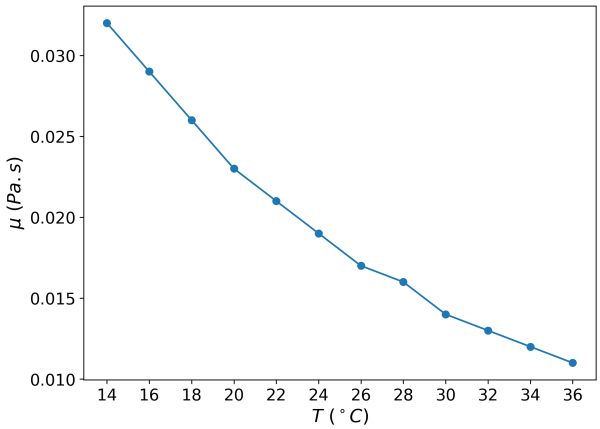

Figure 2.4: Dynamic viscosity of liquid mixture versus temperature (T) for $C_v = 0.65$.

2.2.3 The medium studied

In this study, we have focused on two types of media: confined media and porous medium. Their settings as well as their physical parameters are described following.

Confined medium

As shown in Fig.2.6, the left and right plates are used to form the confined media, and the distance between them is G. As we vary the magnitude of G, we can explore the effect of different G on particle settling, which is presented in Chapter 3.

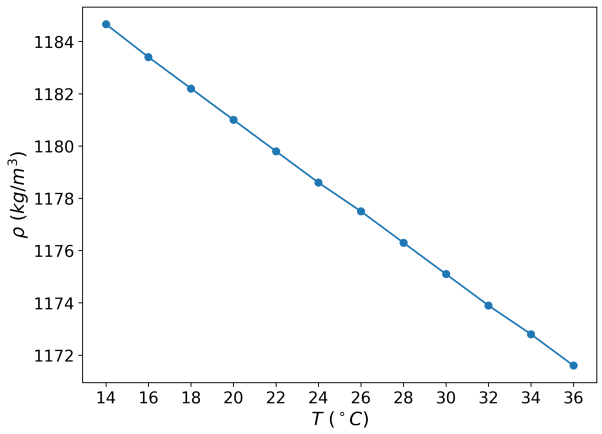

Figure 2.5: Density of liquid mixture versus temperature (T) for $C_v = 0.65$.

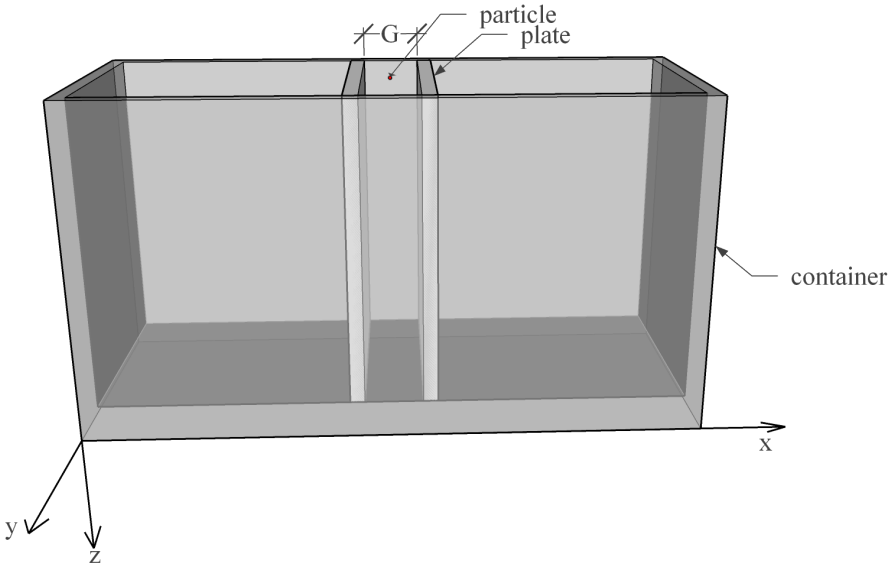

Figure 2.6: Schematic diagram of confined media.

Porous medium

Meanwhile, in the confined media, we further add obstacles to form a porous medium and explore the effect of different obstacles on particle settling. As shown in Fig.2.8, the obstacles in the confined media are composed of pillars passing through the flat plate. The apertures on the plate are equal to the diameter of the pillars so that the pillars can be fixed at the corresponding positions. The pillars are arranged periodically as shown

in Fig.2.7. Therefore, the parameters e_x and e_z control the geometric composition of the obstacles. In this study, the diameter of the pillars (D_f) is 10 mm, and the parameter e_x is set equal to e_z. 12 pillars are used, and they are arranged based on the principle in Fig.2.7 to form the layout shown in Fig.2.8. The parameters e_x and e_z were set to 10 mm, 9 mm, and 8mm to compose three different media structures (M1, M2, and M3 respectively). According to Eq.(2.11), they correspond to radial pore size (e_p) of 4.14 mm, 3.44 mm, and 3.08 mm respectively.

$$e_p = \sqrt{\frac{(D_f + e_x)^2}{4} + \frac{(D_f + e_z)^2}{4}} - D_f \tag{2.11}$$

In addition, the settling of particles is a 3-dimensional motion. Therefore, when multiple particles are injected at the same time, the motion of the particles in the y-axis direction causes an overlap among particles in the recording plane (plane of z-x axis) of the camera, resulting in difficulty in image detection. To minimize this effect, the distance between the front and back plates (G) was set to be 1.5 times the diameter of the injected particles (d_p): 1.5 mm, 3 mm, and 4.5 mm corresponding to 1 mm, 2 mm, and 3 mm of d_p. This could reduce the overlap of particles in the y-direction while also giving the particles some space in the y-direction, reducing the effect of the front and back flat plates on particle settling. Moreover, according to this setup and Eq.(2.12), the porosity (ϕ) of the three types of media were 60.75%, 56.51%, and 54.13%, corresponding to 10 mm, 9 mm and 8.5 mm of $e_x = e_z$ respectively. The final assembled porous media are shown in Fig.2.8.

$$\phi = 1 - \frac{\pi \left(D_f\right)^2}{2 \left(D_f + e_x\right) \left(D_f + e_z\right)} \tag{2.12}$$

2.2.4 Particle employed

In our experiments, we used glass spheres as injected particles. The surface of the particles was covered with black paint to block the passage of light and thus facilitate the subsequent detection of the apparent surface of the particle in the image. If we consider the particles as spheres of diameter d_p, the apparent surface is a circle of diameter close to d_p. The d_p used were 1 mm, 2 mm and 3 mm. The density of the particles (ρ_p) was measured to be 2470 kg/m^3 by using a pycnometer.

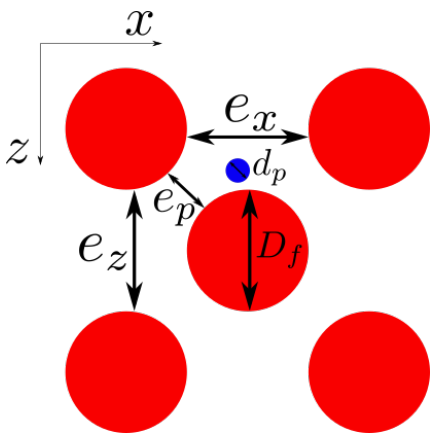

Figure 2.7: Periodical arrangement of pillars.

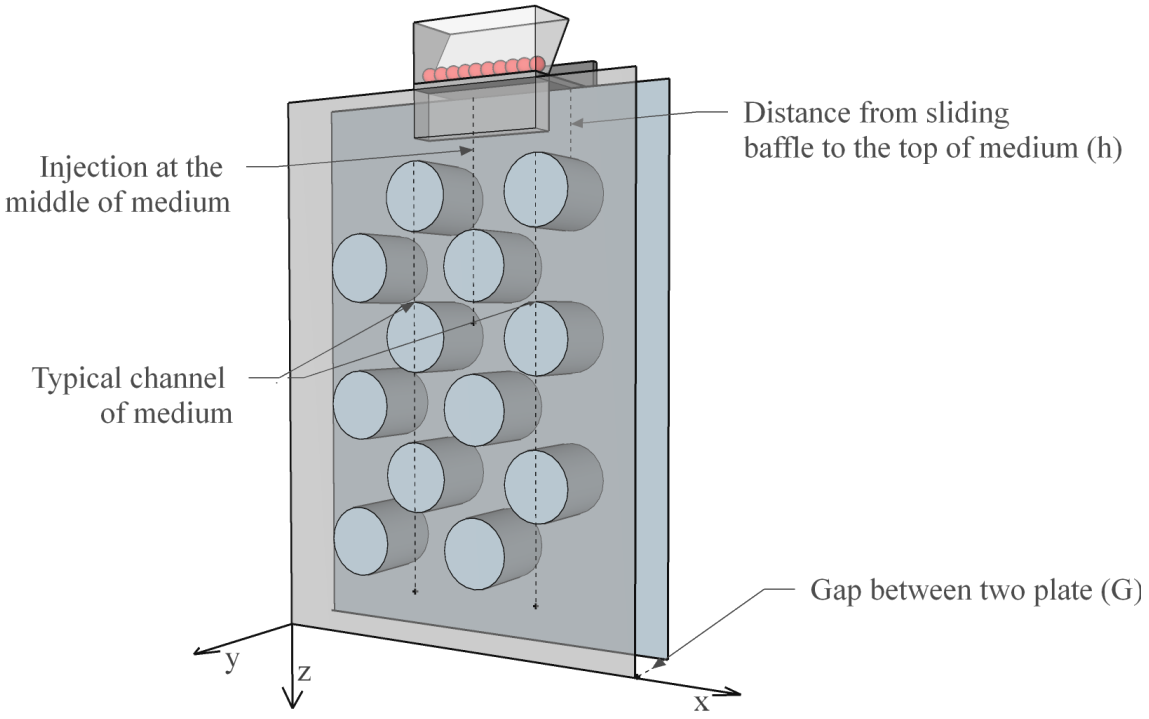

Figure 2.8: Schematic diagram of porous media.

2.2.5 Injection of the particles into the medium

Single particle injection

For individual particles, we chose an injection tube to inject them. The injection tube is held in place by a base placed on top of the container as shown in Fig.2.9. Its height can be adjusted by adjusting the fixed position on it. The bottom of the injection tube was set below the liquid surface, to ensure that the particles could enter the liquid directly. In the experiment, the distance of the injection tube below the liquid surface was about 2 *cm*. Moreover, because the particle does not always flow out of the center of the injection tube, the diameter of the injection tube was selected close to the diameter of the particles, which could reduce the deviation of the injection position at the outlet. The position of the injection tube in the x and y planes can be adjusted by rotating the nuts on both sides of the base.

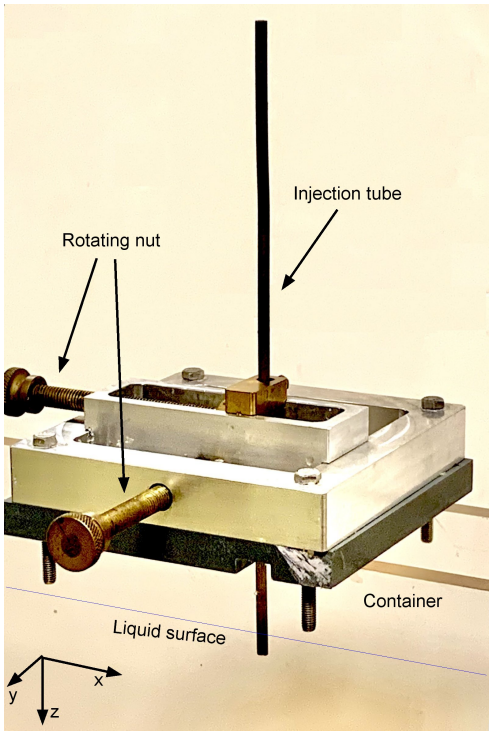

Figure 2.9: Schematic diagram of the injection method for a single particle.

Particle group injection

In the case of a group of particles, an injection box was designed. As illustrated in Fig.2.10, the injected particles should be placed within the injection box manually first. When we withdraw the sliding plate, the particles will be injected into the medium almost simultaneously under the effect of gravity. The entire injection box is placed under the liquid surface level. Consequently, the injection process is also conducted below the liquid surface. For all cases of the experiment, the length of the injection box (L) was fixed at 20 mm. The width (W) was equal to the distance (G) between the front and back plates in the y-axis of the medium, as shown in Fig.2.8.

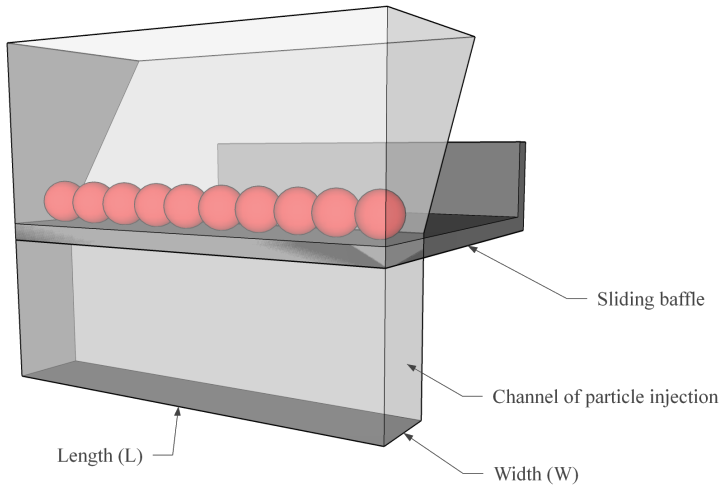

Figure 2.10: Schematic diagram of the injection method for group particles.

2.2.6 Visualisation tools

Light source

We used a light source from the PIERRON brand, model 08420. This light source utilizes a very bright white LED. It is equipped with a condenser lens at the front. The distance between the LED and the condenser lens is adjustable; this allows for the creation of a beam of parallel light rays or various divergent beams. In our experiment, it is necessary to align the center of the light with the center of the observation area inside the container (in the y-axis direction), to ensure, as much as possible, the production of parallel light rays in the observation area. In our experiments, we observed the imaging of the particles

in the camera to determine whether further adjustments to their positions were needed.

High-speed camera

We used a high-speed camera system to record the settling images of the particles. The software Camera tool controls the frequency of the high-speed camera and the photo size. Throughout the experiment, the photo size was set to 2000×1088 pixels (length and width of the image in the unit of pixel respectively). The camera frequency (f) can be set to a maximum of 330 Hz and the camera is connected to a signal synchronizer (EG), which records the time of each camera shot and outputs a time list of the corresponding image sequences. The Hiris software controls the startup, recording, and stopping of the entire camera system, and ultimately outputs the sequence of recorded images and corresponding time series file. The images obtained with this technique are grayscale. The software and the camera are manufactured by the company R&D Vision.

2.2.7 Experiment procedure

For the experiment under different conditions, the general operational steps are presented below:

- Collect materials employed in the experiment: including liquid, the pillars, plates for assembling media, glass particles, injection box, and corresponding injection method;
- Experimental assembly: mounting the assembled porous media and injection device in the transparent container; filling with prepared liquids; placing the container on the experimental platform; setting as well as adjusting the position of containers, cameras, and lights;
- Calibration of the camera: focusing the camera within the plane of particle settling; measuring the image scale (S): 1) placing a ruler in the plane of particle settling; 2) taking an image containing the ruler; 3) measuring the distance of pixels at any distance from the ruler by the measure function of the FIJI software; 4) the scale of the image can be obtained by the ratio of the pixel distance to the corresponding ruler distance;
- Conducting experiment and recording: performing the particle injection operation and recording the particle settling image;

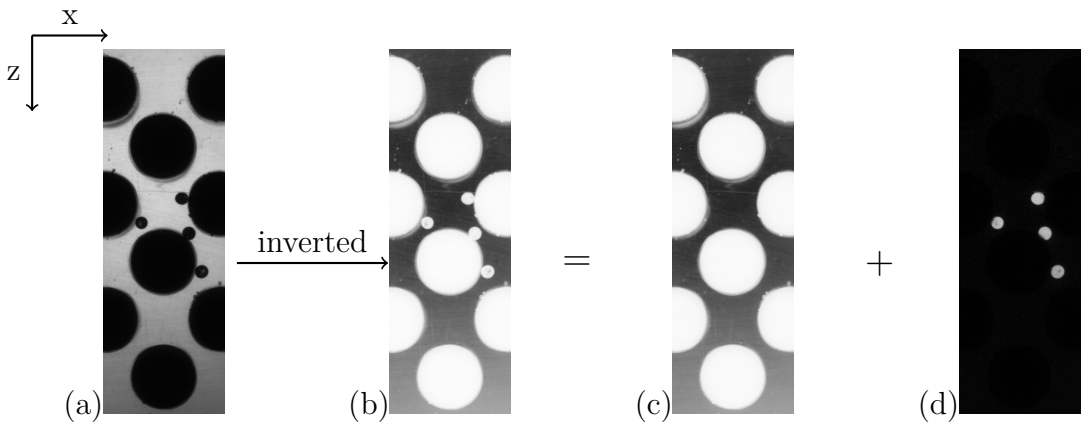

Figure 2.11: Example of image preprocess: (a) Original image sequence; (b) Inverted original image sequence; (c) Inverted background; (d) Subtracted image sequence.

- Output and save the recorded images as well as the time series files from Hiris software.

2.3 Image analysis

We applied a particle detection method to the image to extract the position of the particle coordinates in each frame. The availability of these positions over time allows us to analyze the behavior of the particles, such as particle traces, velocity, travel time, concentration, etc. This section begins with a detailed description of the image processing and detection algorithms. Then the post-processing algorithms for the obtained data are presented.

2.3.1 Process and algorithm of image detection

Preprocess of image

In order to minimize the interference of other objects (like the presence of pillars or noise) in the following particle detection, the original image sequence was preprocessed first. As shown in Fig.2.11, the original image sequence was imported into the Fiji software [20], and inverted. The frame of the sequence (background without particles) was imported again and also inverted. Then the inverted image sequence was subtracted by the inverted first frame image to obtain the image with only white particles and a black background. These subtracted images were used in the following image detection.

Particle detection and connection

After preprocessing the image, the Trackmate [21] plugin in Fiji was employed to detect and connect the positions of each particle among different frames. Trackmate is a plugin for analyzing time-lapse image data that can be used to track objects such as spots. It provides several particle detection and connection methods. The Laplacian of Gaussian (LOG) particle detection method [47] and Linear Assignment Problem (LAP) [48] connection method are used here referring to the similar research [49].

1. Laplacian of Gaussian (LOG) particle detection method
   LOG [47] is a commonly used featured detection algorithm in image detection. Its main function is to detect the edge, where the gradient of pixel value (how sharply the pixel values change) is very high. The principle of the LOG algorithm is shown in Eq.(2.13).

$$\mathrm{LoG}_\sigma = -\sigma^2 \left(\frac{\partial^2}{\partial x^2} + \frac{\partial^2}{\partial z^2} \right) * G_\sigma * I \tag{2.13}$$

   G_σ is a Gaussian filter that is used to smooth the image. It serves to reduce the noise in the image. σ is the standard deviation of the Gaussian filter, which determines the width of the filter. The larger the value of σ, the wider the filter. The Laplace operator could highlight rapidly the changing areas of the image, i.e. edges. $-\sigma^2$ is used to adjust the strength of the Laplace operator. $*$ indicates a convolution operation. In the specific calculation, LOG will first use the Gaussian filter G_σ to smooth the original image I. Then, the Laplace operator is applied to the smoothed image, and the zero-crossing point in the result is the edge to be recognized.
   For the detection of circular particles in Trackmate, the value of σ is adjusted according to the particle radius input by the user: $\sigma = r/\sqrt{n_{dim}}$, where n_{dim} is the dimension of the source image (2 Dimension for 2), and r is the particle radius. For Gaussian-like particles, a maximum value could be generated at the center of the particles after the LOG algorithm is computed. Therefore, in the filtered image, Trackmate looks for local maxima to indicate spot detection. Each detected spot is assigned a quality value (Q) by taking the local maximum in the filtered image. Spots with a quality lower than the detector's configured value (input by the user) are immediately discarded. If desired, the location of the retained spot can be finely tuned using a quadratic fitting-based scheme proposed by Lowe et al [50].

2. Simple LAP tracker
   In this study, we used the Simple LAP tracker in Trackmate to link the trajectories of particles in the image sequence. The Simple LAP tracker first checks for possible links between two consecutive frames. For each object detected in the previous frame, there is the possibility of choosing to link or not to link with any other object in the next frame. This potential linking relationship is represented by constructing $(c+d) \times (c+d)$ cost matrix, where c and d are the number of objects in two consecutive frames, respectively. This matrix (in Fig.2.12) is divided into four quadrants representing different types of linking costs: linking spots in two frames at top left quadrant, spots in one frame that are not linked to the next frame (end of segment) at bottom left quadrant, spots in the next frame that are not linked to the previous frame (beginning of segment) at top right quadrant, and an auxiliary block required for the Linear Allocation Problem (LAP) at bottom right quadrant. For the Simple LAP tracker, the linking cost is mainly considered for the distance between particles as well as for the input maximum linking distance d_{max}. If the distance between the spots exceeds the maximum distance allowed, the link is disabled and the cost is set to ∞. The final allocation scheme can be derived by calculating the minimum sum of costs for the entire matrix. In this way, all pairs of frames can be efficiently linked frame-by-frame to generate a series of non-branching trajectory segments. Next, these constructed trajectory segments are further provided for interlinking. The Linear Allocation Problem (LAP) framework is used again. At this stage, the user can also provide a maximum time difference for linking, beyond which no linking will be provided.

Fig.2.13 illustrates the specific procedure of image analysis and the estimation method of the parameters to be input.

2.3.2 Post processing of data

Schematic of particle behavior analysis

Firstly, with the camera, we record the settling of a single particle at different times. Therefore, we mainly calculated the velocity profiles and trajectories of the particles to show the effect of different settings on the particle settling behavior.
For the porous medium, we analyzed the particle settling behavior from two perspectives.

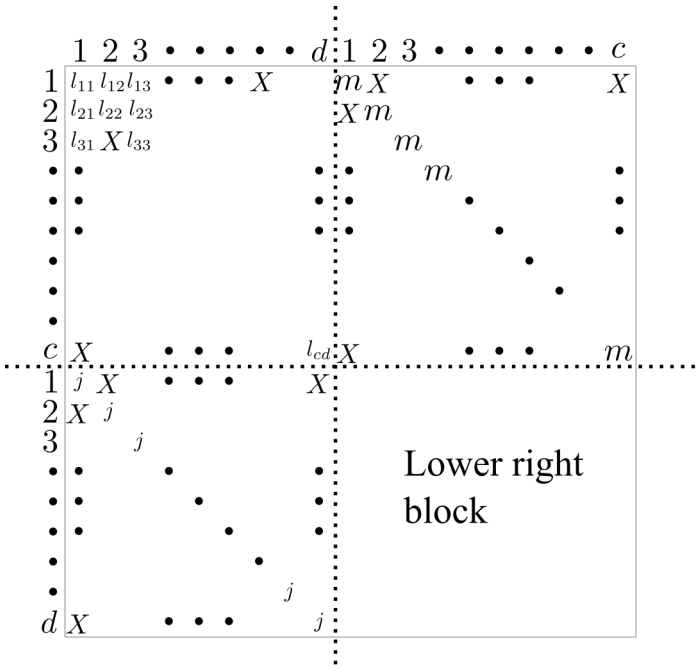

Figure 2.12: Example of cost matrix for Simple LAP linking between two consecutive frames; In previous frame, there are several c of particles, and number of d in the next frame; l_{cd}: the cost for particle c to connect particle d in next frame, which is the distance between them; X: impossible link whose cost exceeded the d_{max}; m and j: cost for no linking; The lower right block is an auxiliary block required to satisfy the topological constraints of the LAP. [48]

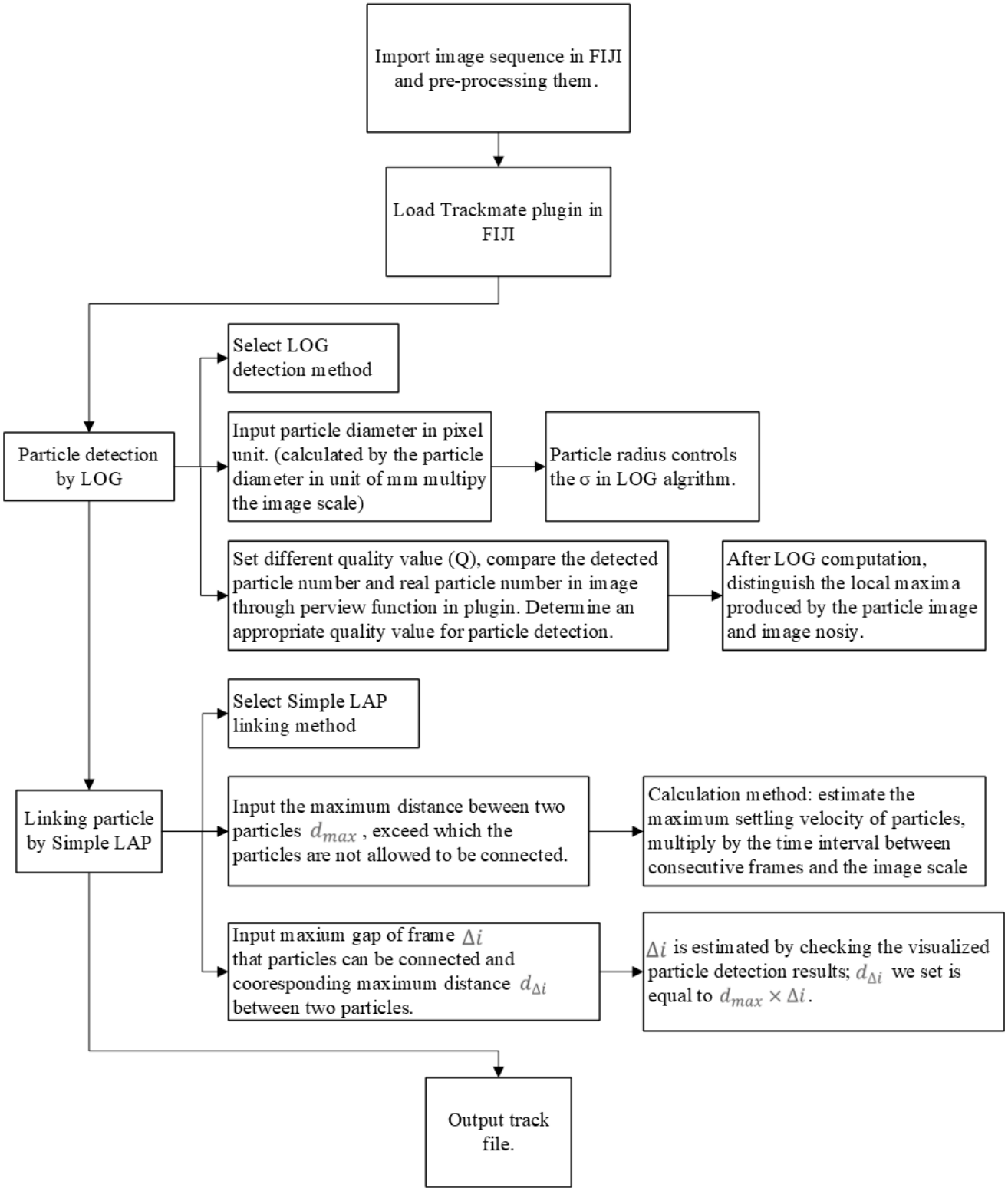

Figure 2.13: Flowchart of image analysis in FIJI

One of them is at the pore space, as shown in Fig.2.14, where the intersection between the upper and lower pillars will constitute the pore structure. Therefore, according to the layout of the medium, we partitioned five pore regions along the depth of the medium. The upper boundary of each pore region corresponds to the center of the upper pillar and the lower boundary corresponds to the center of the lower pillar. The upper and lower boundaries are also the inlet and outlet of the pore region, respectively. The left and right boundaries correspond to the centers of the leftmost and rightmost pillars, respectively. The other one is over the entire medium height. As shown in Fig.2.14, the upper and lower boundaries of the region of the medium are at the inlet and outlet, and the left and right boundaries are also the centers of the leftmost and rightmost pillars. The inlet and outlet (z_{inlet}, z_{outlet} corresponding to the pore region and medium are used for the following analysis.

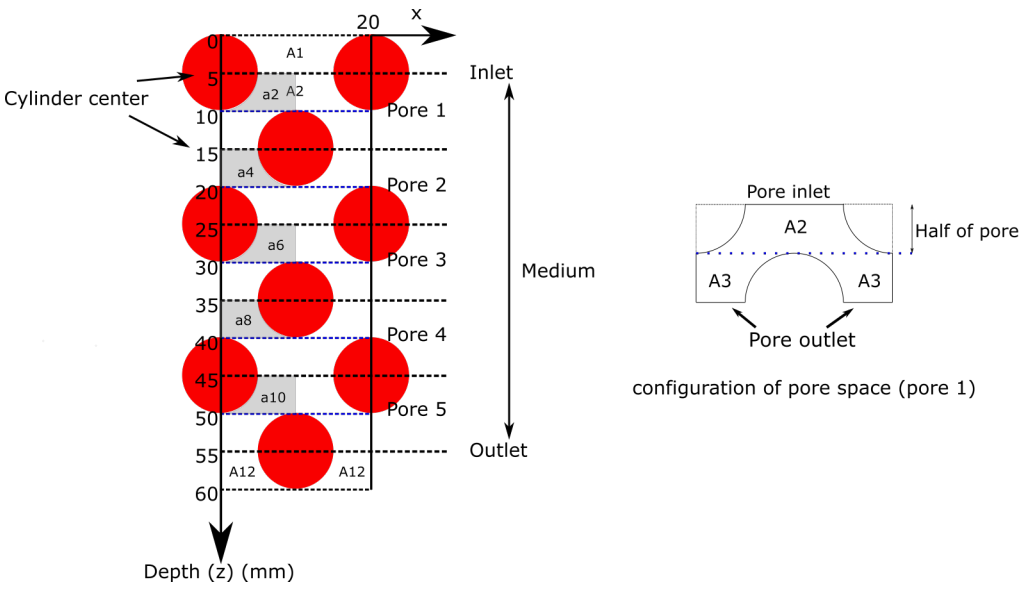

Figure 2.14: Diagram of dividing the medium into zones for the behavior analysis (Example while $e_x = e_z = 10mm$)

Particle trajectory

After image detection (particle detection and linking), we can obtain the trajectories of each particle and their corresponding time series, as shown in Table.2.1. Then, we can extract more properties of particle motion by post-processing of data, like particle velocity, travel time, particle number, concentration in a specific area, contact number

Table 2.1: Sample of time data and particle position

Frame number (i)	Recording time (t_i)	Detected particle coordinates
1	t_1	x_1, z_1
2	t_2	x_2, z_2
3	t_3	x_3, z_3
⋮	⋮	⋮
i	t_i	x_i, z_i

among particles, and contact number between particle and pillar.

Particle velocity

The particle velocity is:

$$\vec{v} = v_x\vec{x} + v_z\vec{z} + v_y\vec{y} \tag{2.14}$$

where $\vec{x}, \vec{z}$ and $\vec{y}$ are the unit vector along x, z and y direction.
In this study, the particle velocity ($\vec{v}$) is set in the x-z plane and composed of velocity components in the x, z direction. v_x, v_z can be calculated by:

$$v_x = \frac{x_i - x_{i-step}}{t_i - t_{i-step}} \tag{2.15}$$

$$v_z = \frac{z_i - z_{i-step}}{t_i - t_{i-step}} \tag{2.16}$$

v_x, v_z are the average velocity between the time interval of frame $i - step$ to frame i. The *step* is not necessarily equal to 1.
We use v to denote the scalar velocity of the particle, and it can be calculated by:

$$v = ||\vec{v}|| = \sqrt{v_x^2 + v_z^2} \tag{2.17}$$

In addition, for medium with obstacles, to counteract the effect of the front and back flats and show only the delay of the obstacles to the particles, we use a normalized variable. The final steady settling scalar velocity of the particles in the case of only front and back flat media is v_{plate}, and the normalized setting scalar velocity for a particle is:

$$v^* = \frac{v}{v_{plate}} \tag{2.18}$$

Travel time

Travel time is the time it takes for a particle to pass a specific distance. It can reflect the degree of delay experienced by the particles due to the confinement or the obstacles. Travel time is calculated at both the medium height and pore space. The starting z_{inlet} and ending z_{outlet} line of the calculation correspond to the inlet and outlet of the medium and pore regions, respectively. First, we find the number of frames corresponding to when the particles are located at z_{inlet} and z_{outlet} by calculating the minimum values of $|z_i - z_{inlet}|$ and $|z_i - z_{outlet}|$, and then we obtain the travel time of the particles by $t_{outlet} - t_{inlet}$. For each particle, t_m and t_p are the travel time corresponding to the medium and pore region. Similar to normalization in velocity calculation, the time taken within the same distance from z_{inlet} to z_{outlet} in the case of front and back plates can be obtained by:

$$t_{plate} = \frac{z_{inlet} - z_{outlet}}{v_{plate}} \tag{2.19}$$

So the normalized travel time for the particles to pass through the obstacles at medium and pore space are:

$$t_m^* = \frac{t_m}{t_{plate}} \qquad t_p^* = \frac{t_p}{t_{plate}} \tag{2.20}$$

Besides, we use $\bar{t}_m$ and $\bar{t}_p$ to denote the mean travel time of their passage through the corresponding region for multiple particles:

$$\bar{t}_m^* = \frac{1}{N_p} \sum_{j=1}^{N_p} t_{mj}^* \tag{2.21}$$

$$\bar{t}_p^* = \frac{1}{N_p} \sum_{j=1}^{N_p} t_{pj}^* \tag{2.22}$$

t_{mj}^* and t_{pj}^* are the travel time across the medium and pore space of particle j.
$\bar{T}_m$ and $\bar{T}_p$ are used to denote the mean travel time of multiple tests.

$$\bar{T}_m^* = \frac{1}{N_t} \sum_{j=1}^{N_t} \bar{t}_{mj}^* \tag{2.23}$$

$$\bar{T}_p^* = \frac{1}{N_t} \sum_{j=1}^{N_t} \bar{t}_{pj}^* \tag{2.24}$$

$\bar{t}_{mj}^*$ and $\bar{t}_{pj}^*$ are the mean travel time across medium and pore space of test j.

Particle number entered, exited, and retained

Depending on the setting of the media area and the pore area, we counted the number of particles passing through the inlet of the corresponding area ($N_{entered}$) and the number of particles passing through the outlet of the corresponding area (N_{exited}). The calculation procedure for determining the passage of particles through the inlet and outlet is shown below (using the inlet as an example). The inlet consists of a straight line linked from point 1 (x_{p1}, z_{p1}) to point 2 (x_{p2}, z_{p2}). The coordinates of the particle between two consecutive frames are x_i, z_i and x_{i+1}, z_{i+1}. Calculate the cross product of the particle coordinates in the two frames with the line vector $(x_{p2} - x_{p1}, z_{p2} - z_{p1})$:

$$C_1 = (x_i - x_{p1})(z_{p2} - z_{p1}) - (z_i - z_{p1})(x_{p2} - x_{p1}) \tag{2.25}$$

$$C_2 = (x_{i+1} - x_{p1})(z_{p2} - z_{p1}) - (z_{i+1} - z_{p1})(x_{p2} - x_{p1}) \tag{2.26}$$

If the signs of C_1 and C_2 are different, it means that the particle has crossed the line (they are on different sides of the line). If the signs of C_1 and C_2 are the same, then the particle has not crossed the line.
By performing the above calculations on the obtained particle trace data, it can be determined whether the particles have entered the corresponding pore or medium region in each test. $\bar{N}_{entered}$ and $\bar{N}_{exited}$ are used to represent the average value of many tests (N_t) under the corresponding conditions:

$$\bar{N}_{entered} = \frac{1}{N_t} \sum_{j=1}^{N_t} N^j_{entered} \tag{2.27}$$

$$\bar{N}_{exited} = \frac{1}{N_t} \sum_{j=1}^{N_t} N^j_{exited} \tag{2.28}$$

$N^j_{entered}$ and N^j_{exited} are the particle number entered and exited in test j. Moreover, the difference between $\bar{N}_{entered}$ and $\bar{N}_{exited}$ is to show the particle number retained ($\bar{N}_{retained}$) in the corresponding region.

Particle flow rate at inlet and outlet

By using Eq.(2.25) and Eq.(2.26), when C_1 and C_2 have opposite signs, we can also obtain the number of frames (i) and the time (t_i) at which the particles entered in the region.

Therefore, we can approximate the inlet particle flow from time t_j to $t_j + \Delta t$ by:

$$q_{in}^{t_j+\frac{\Delta t}{2}} = \frac{N_{entered}^{\Delta t}}{(t_j + \Delta t) - t_j} \tag{2.29}$$

Particle concentration

The gradual accumulation of particles at the pore throat leads to the eventual clogging phenomenon. [15] Therefore, half of the area of the pore space is used to calculate the concentration as shown on the right side of Fig.2.14. This can highlight the accumulation behavior of particles within the upper pore area. Therefore, the concentration of particles within the region can be calculated by the following equation:

$$c = \frac{N_{retained}\pi(\frac{d_p}{2})^2}{A_*} \tag{2.30}$$

$$A_* = \frac{\frac{1}{2}(e_x + D_f)(e_z + D_f) - \pi(\frac{D_f}{2})^2}{2} \tag{2.31}$$

$N_{retained}$ is the particle number retained in the corresponding region, A_* is the surface area of half pore region, which corresponds to the $A_1, A_2, ...A_{12}$ in Fig.2.14. Therefore we could calculate the distribution of particle concentration along the depth for each frame. Moreover, we can focus on how the concentration in a region changes between frames to show the process of particle accumulation and passage.

Determination of contact

Based on the particles' position in each frame, the distance (d_i) between each two particles (k, l) can be calculated:

$$d_i = \sqrt{(x_i^k - x_i^l)^2 + (z_i^k - z_i^l)^2} \tag{2.32}$$

And if:

$$d_i \leq (r_k + r_l - d_\epsilon) \tag{2.33}$$

the two particles are overlapping and can be thought in contact [37]. d_ϵ is the experimental error, which is set to be the 0.2 of d_p. Therefore, we can further count the contact number among particles CN_p or between particle and pillar CN_{pc} at medium or pore space as time.

Clogging probability

Some models of clogging probability have been proposed based on the particle size exclusion effect or kinematic properties [18], [19]. When particles clog a pore throat, the concentration in the clogged area will increase first and tend to be constant in the end [19]. Thus, we can search if $c > 0$ (the initial c equals 0) at the end to judge if a clog happens. But there is another case where the particles just deposited in the upper part of the pillar. This also causes a constant concentration eventually. Since the sides of the pillar are curved, only a few particles can stay above the pillar. Therefore, to avoid recognizing the deposition of particles on the pillar as a clogging event, we set a limiting concentration (c_{lim}). When $c > c_{lim}$ at the end of sedimentation, clogging is considered to have occurred. Then, we can obtain the probability of clogging under the corresponding conditions:

$$P = \frac{N_{clogged}}{N_t} \tag{2.34}$$

$N_{clogged}$ is the number of clogged tests by judging if $c > c_{lim}$.

2.4 Validation of the experiment setup

To verify the accuracy of the experimental setup, we first used the device to detect the position of a stationary particle in the image sequence to show whether the device could accurately acquire the position of the particle in the image; then we detected the free settling behavior of individual particles in the liquid and compared the final stable settling velocity with the theoretical value calculated by the Stokes' law to show whether the device can accurately detect the particle's motion behavior.

2.4.1 Detection of static particle

Experiment setup

As shown in Fig.2.15 (a), a 1 mm particle is put statically on the top of a circular pillar under a liquid surface. All of these are set inside the transparent container and recorded by the camera in front. Two image scales (S), 17.9 pixel/mm and 27.1 pixel/mm, are used to detect the static particle position. The image frequency (f) is 330 Hz. In each case, particles were recorded a thousand times to see if there was a larger fluctuation in the

detected position for the static particle, which is fixed in fact. The detected coordinates are obtained through the image analysis method above (Fig.2.15 (b)). By this comparison, we can see if the experiment setup could detect a particle position accurately or how many errors it could produce in detection.

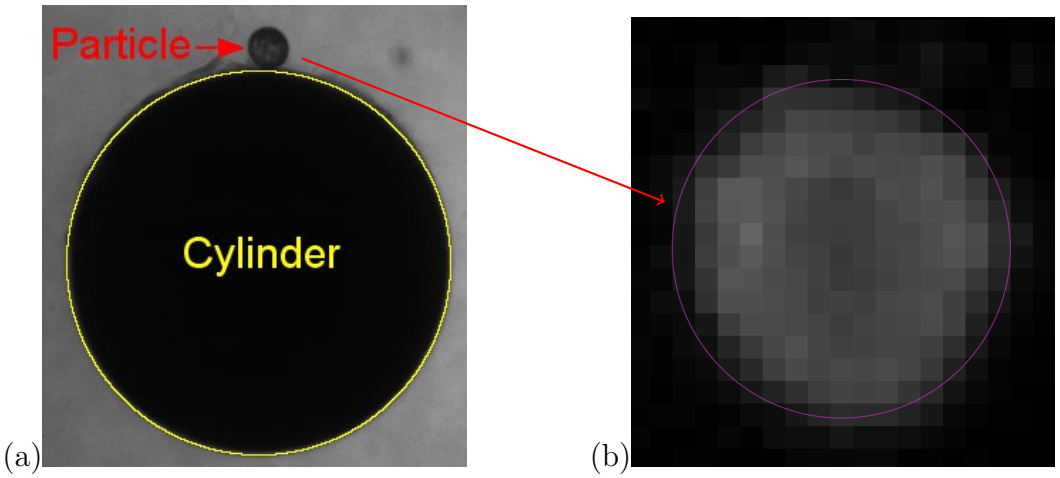

Figure 2.15: (a) Experiment setup of static particle detection; (b) Subtracted image of the particle (white spot) and detected particle in Trackmate (pink circle).

Results

The distribution of the position coordinates of the detected stationary particle at the scale of 17.9 pixel/mm is shown in Fig.2.16, where the blue points are the center of the detected particle. It can be seen that the detected center coordinates have some fluctuations in both the x and z axes. We calculated the mean as well as the standard deviation between the coordinates in the x-axis, and z-axis, respectively. The detected mean coordinates are (202.64, 117.71) (red point in Fig. 2.16) and standard deviations corresponding to 0.0158 and 0.0267. When we draw a circle with the mean value as the center (red point) and 3 times the standard deviation of the z-axis (0.0267) as the radius (the 3 times selected here just try to fit the distribution of data points), we can see that most of the coordinate points are included in this area. Thus we can conclude roughly that at the scale of 17.9 pixel/mm, the experimental setup leads to a detection fluctuation of ± 0.08 pixel (± 0.004 mm). We did the same analysis at the scale of 27.1 pixel/mm and obtained a detection fluctuation of ± 0.048 pixel (± 0.002 mm). This shows that when we increase the image scale, it could reduce the image detection fluctuation. Overall, the fluctuations produced

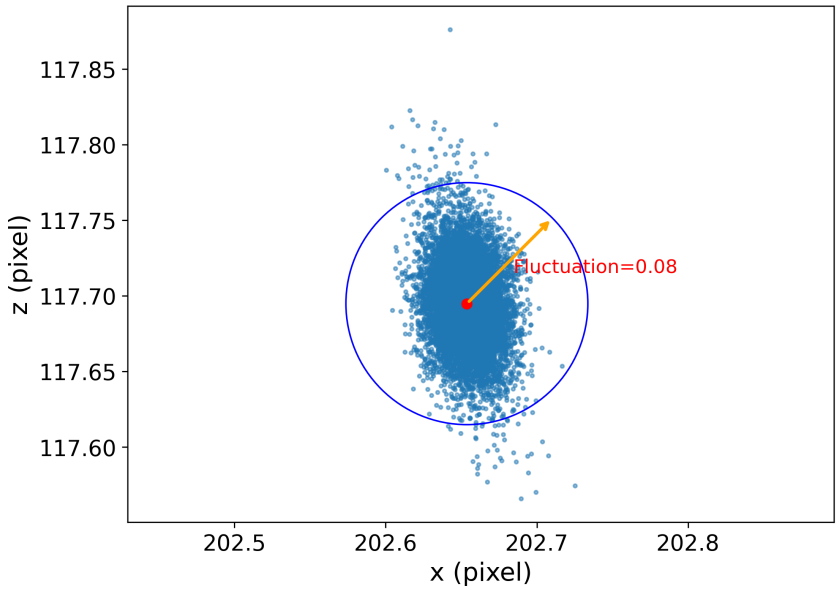

Figure 2.16: Distribution of detected particle positions with image scale $S = 17.9$ $pixel/mm$; the blue points are the center of detected particle position; the red point is the mean among detected particle positions; the radius equals 3 times the standard deviation of coordinates in the z-axis (0.0267).

by the detection methods are very small and they can detect the coordinates of the particles accurately.

2.4.2 Detection of particle free sedimentation

Experiment setup

In this section, we would like to verify whether the experimental setup can accurately detect the motion behavior of the particle. We used the tube injection method to inject a 1 mm particle into the liquid medium in the container. The injection location was located at the top center of the container. The size of the container was large enough so that the particles did a free settling motion inside the container. The camera recorded the settling motion of the particle after it left the injection tube. The above-mentioned image detection, as well as data processing methods, were used to detect the particle traces as well as velocity profiles. The experiment was repeated twice. The relevant experimental parameters are shown in Table.2.2.

Table 2.2: Experiment parameters for particle sedimentation

Liquid	μ	0.91	$\mathrm{Pa} \cdot \mathrm{s}$
	ρ_l	1260	$\mathrm{kg/m^3}$
Particle	ρ_p	2470	$\mathrm{kg/m^3}$
	d_p	1	mm
Recording	Image scale (S)	21.3	$pixel/mm$
	Camera frequency (f)	330	Hz

Results

Fig.2.17 illustrates the detected particle settling traces of two individual particles. From the beginning to the end of the trace, the particles produced an average vertical settlement of 89.6 mm in the image and lateral displacements of 0.41 and 0.22 mm. As can be seen from the magnified traces, the settling of the particles is accompanied by small lateral movements. The accumulation of these transverse motions causes the traces to be shifted in the x-direction and increase in the lateral displacements. This may be due to the imperfect sphericity of the particles as well as the small initial lateral injection velocity. In general, the lateral displacement only results in an average percentage of 0.35% relative to the vertical displacement, which also shows that the particles are mainly doing vertical settlement.

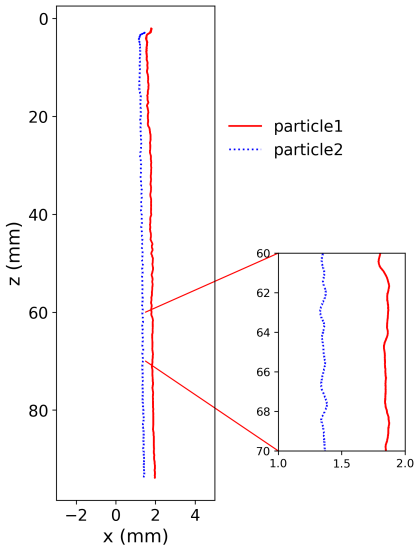

Figure 2.17: Detected sedimentation trajectories of the two particles.

Fig.2.18 illustrates the velocity variation of the particles at different settling positions (z-axis). We can see that the velocity profile produces large fluctuations when the selected velocity calculation parameter *step* is 1 (Eq.(2.15 and 2.16)). When we increase the *step* to 10 and 70, the fluctuation of the profile decreases gradually. This is because, in the position detection of the particles, there is a certain amount of position fluctuation. In two adjacent frames, the displacement of the particle is less than the position fluctuation generated by the detection, thus leading to the fluctuation of the velocity value. When we increase the calculation *step*, the actual displacement of the particle between the two frames is much larger than the position fluctuation in the detection, so we can get a more stable velocity curve. This means that we need to ensure a suitable interval in the velocity calculation, which can be achieved either by increasing the calculation parameter *step* or by directly reducing the recording frequency f of the camera. At the same time, we also need to avoid excessive averaging to lose some of the particle motion details. And in this case, we use *step* of 70 for the following analysis.

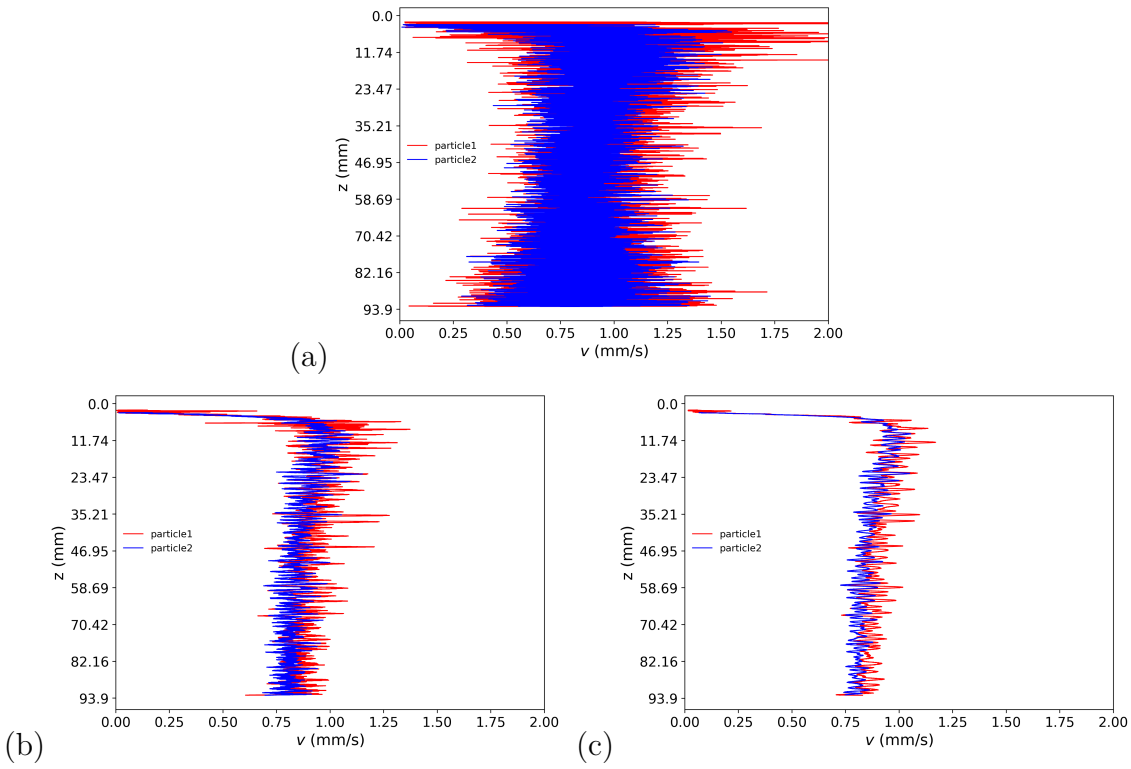

Figure 2.18: Calculated particle velocity profile (v_i) along z axis; (a) step=1; (b) step=10; (c) step=70.

Fig.2.19 shows the variation of the velocity during particle settling (z-axis) and the variation of the velocity component in the x-axis, and z-axis direction. Through Fig.2.19 (a), we see that when particles have just exited the injection tube, they accelerate rapidly. As the particles move away from the injection tube, the resistance of the liquid increases and the velocity of the particles starts to decrease and reaches a steady state gradually. The final stabilized settling velocities of the two particles are 0.818 mm/s and 0.849 mm/s. This lies in the theoretical settling velocity interval of 0.79-0.87 calculated by the Stokes law when the size of the particles varies from 1-1.05 mm. Through Fig.2.19 (b) and (c), we can notice that the particles generate a certain small lateral velocity at the outlet of the injection tube (v is small at the beginning), but v_z/v remains around 1 quickly, which indicates that the vertical settling soon dominates the whole movement. The tiny velocity fluctuations in the x-axis direction also show the process of small displacement accumulation of the particle traces in the x-axis direction.

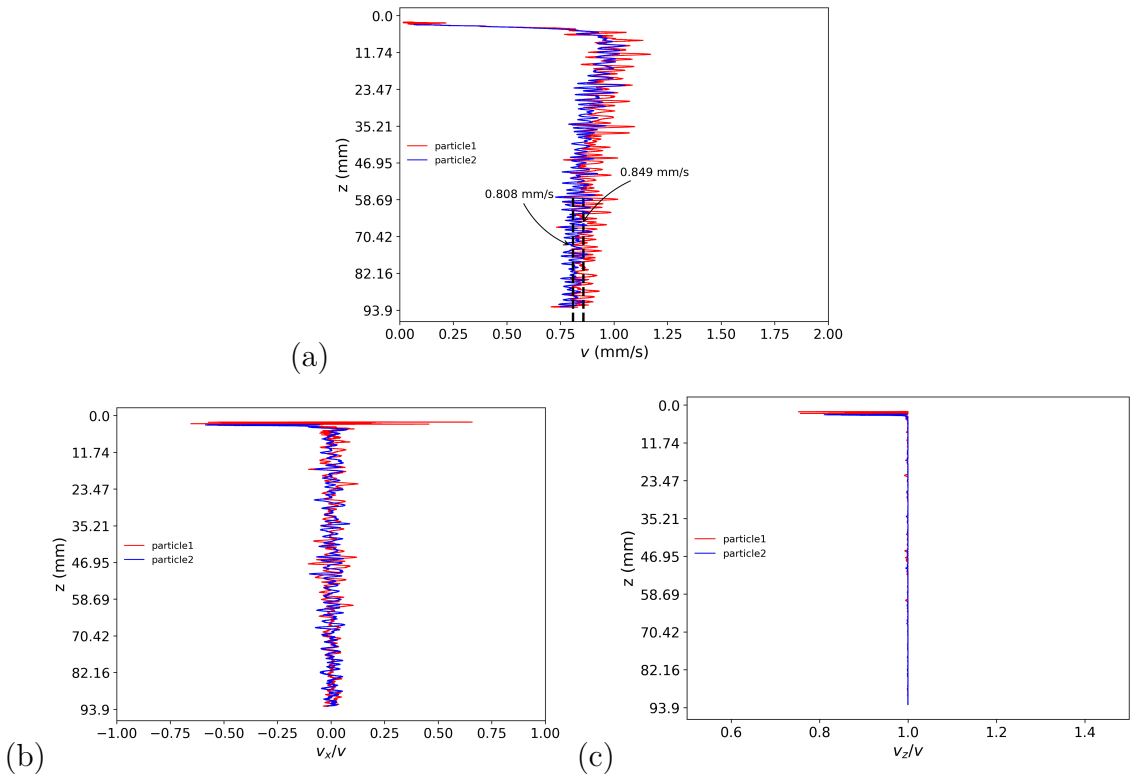

Figure 2.19: Particle velocity profile along z axis; (a) v; (b) v_x/v; (c) v_z/v.

Overall, the detected particle motion is consistent with the actual particle motion, so we

can use this experimental setup to observe the particle settling motion under different conditions.

2.5 Conclusion

In this chapter, we have described in detail the setup of the experiment, the process and algorithm of image processing, and the analysis and calculation of particle behavior. By detecting the position of a stationary particle, we have found that the experimental setup produces a small position fluctuation during particle detection, and this position fluctuation decreases as the image scale increases. However, when this detection method is used to track the free-settling motion of a particle in a fluid, position fluctuations are encountered, which of course induce velocity fluctuations. This is caused by the actual particle displacement being smaller than the detected position fluctuation. Therefore, we can minimize this effect by changing the computation interval (*step*) or reducing the camera frequency. The detection results of both experiments show that the whole experimental setup can better detect the coordinates of the particles and reflect the corresponding particle settling behavior. Therefore, we can go further to analyze more complex particle settling behaviors.

Chapter 3

Sedimentation of a single particle in confined media

3.1 Introduction

With the experiment setup in the previous chapter, we first investigate the influence of a confined medium on particle sedimentation. The sedimentation process of the particles with different sizes (1, 2, and 3 mm) is recorded as the gap between two plates of confined medium (G) decreases gradually. The trajectories and velocity profiles are further extracted to show their influence. Next, we change to the porous medium to see the particle motion inside the medium. Three medium structures (M1, M2, and M3) and three particle sizes (1, 2, and 3 mm) are tested. The motion characteristics of the particles under different combinations are presented in detail and the induced delay (travel time) is further compared. Both the effect of the confined medium and porous medium on particle sedimentation are shown in this chapter.

3.2 Particle sedimentation in confined media

In this section, we first describe the experimental setup for particle settling in the confined medium. Then, by analyzing the obtained trajectories and velocity profiles under different distances G between two plates and particle diameters, we show that how G and particle diameter influence the particle settling velocity.

3.2.1 Experiment setup

As shown in Fig.2.6, we place two flat plates inside a transparent container to form a confined medium. Particles are injected below the liquid level into the container by using the tube injection method at the upper center of the two plates. The camera set in

the y-direction records the settling motion of the particles in the x-z plane. We use the image processing and data processing methods described in the previous section.2.3.2 to calculate the settling traces and velocity profiles of the particles. In this experiment, 1, 2, and 3 mm particles are used. For each particle size, the interval G (in Fig.2.6) between the two flat plates is varied to test the effect of G on the settling behavior of different particle sizes. For each case, 4 times of tests are repeated. The relevant parameters in the experiment are listed in Table.3.1.

Table 3.1: Experiment parameters for particle sedimentation in confined media

Liquid	μ	0.91	$\mathrm{Pa \cdot s}$
	ρ_l	1260	$\mathrm{kg/m^3}$
Particle	ρ_p	2470	$\mathrm{kg/m^3}$
	d_p	1, 2 and 3	mm
Recording	S	21.3	$pixel/mm$
	f	330	Hz

3.2.2 Experiment results

Fig.3.1 shows the settling trajectory under different G and d_p. We can find that after the particles are injected at the center of the gap between the plates, they settle along the center of the gap. Through the enlarged trace subplot, it can be found that the particles are accompanied by certain transverse displacement fluctuations. The transverse fluctuations for G=9.5 mm, d_p=2 mm and G=11.5 mm, d_p=3 mm are larger than those of 1 mm (G/d_p is close). Among 4 tests, the mean value of the absolute difference between the x-coordinate of the starting point and the endpoint of the trajectories are 0.15 mm, 0.25 mm, and 0.25mm for these three conditions. Fig.3.2 shows the velocity profile along the z-axis, and the normalized velocity components in the x and z axes for G=4.5 mm, d_p=1 mm. The particles accelerate rapidly as they leave the injection outlet and then reach a steady state due to the resistance of the liquid. The lateral velocity of the x-axis fluctuates back and forth between -0.1 and 0.1, and the mean is -0.001 with a small standard deviation of 0.002. The velocity component in the z-axis is maintained at around 1. All these results show that the particles are mainly doing vertical settling motion, which is the same under different G and d_p.

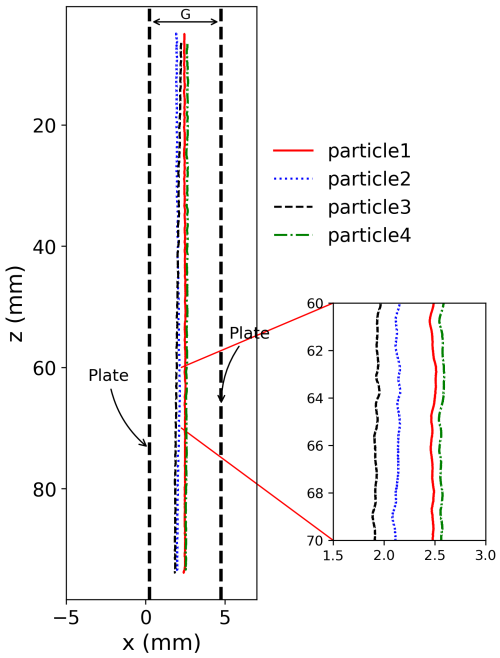

(a) G=4.5mm, d_p=1mm

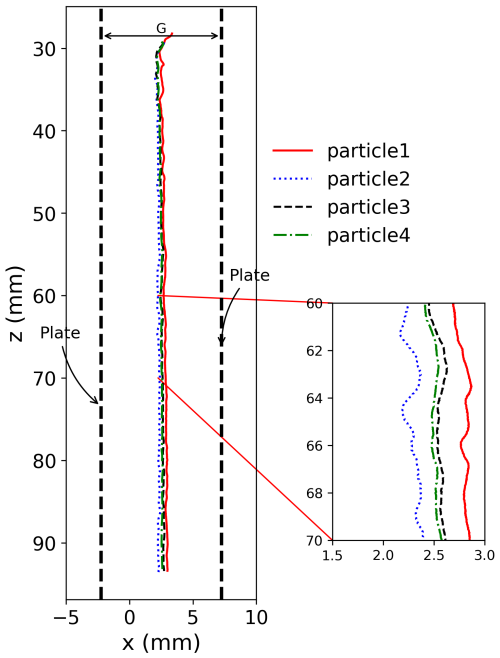

(b) G=9.5mm, d_p=2mm

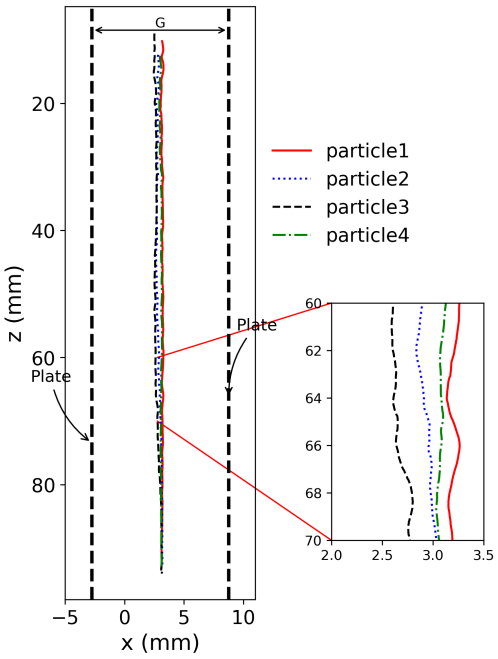

(c) G=11.5mm, d_p=3mm

Figure 3.1: Particle trajectories along the z-axis in confined media; Particles are injected individually.

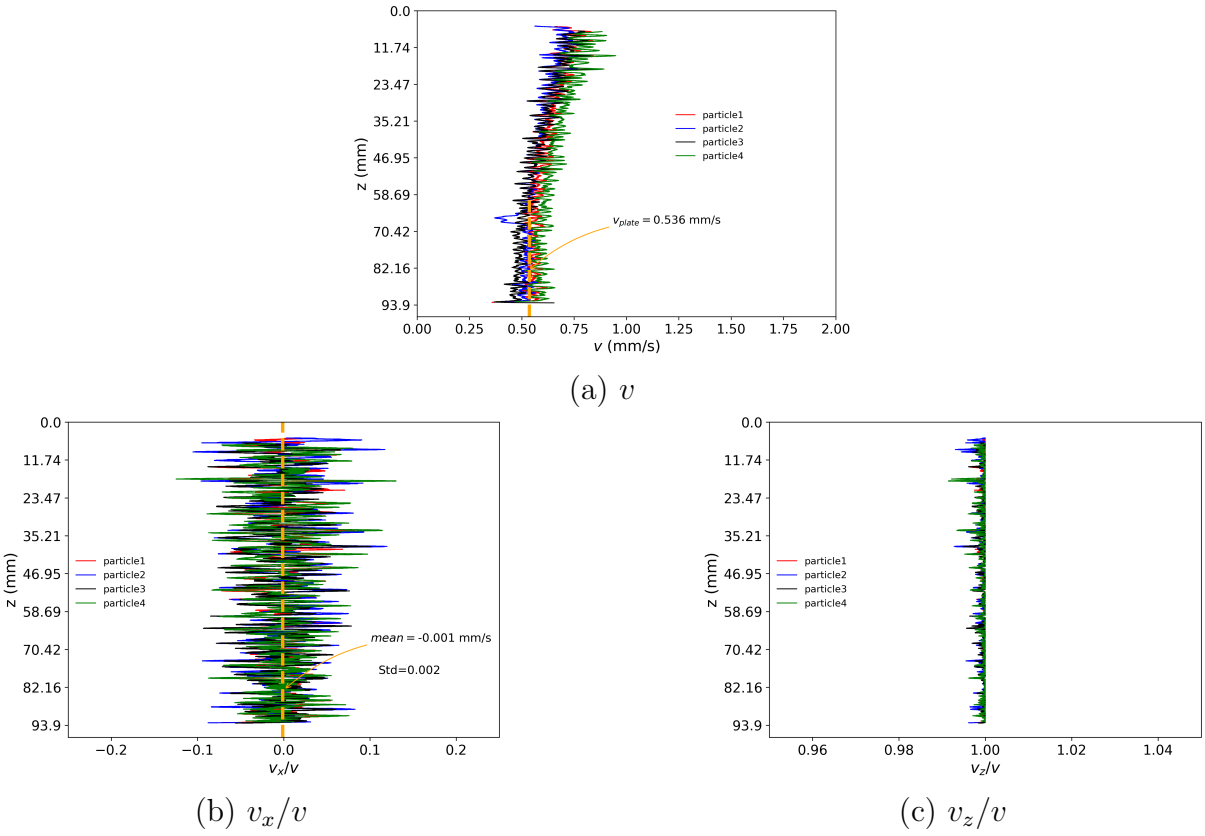

(a) v

(b) v_x/v

(c) v_z/v

Figure 3.2: Particle velocity profile along z axis in confined media for G=4.5mm, d_p=1mm.

We use v_{plate} (Fig.3.2 (a)) to denote the final stabilized settling velocity between the plates. The free settling velocity (v_s) of the particle under the same liquid and particle conditions are calculated by Stokes law. Fig.3.3 illustrates the variation of the final steady settling velocity (normalized, v_{plate}/v_s) of the particles with confining ratio (G/d_p). Also, we use the following equation to fit the detected data.

$$\frac{v_{plate}}{v_s} = a\left(1 - e^{\left(-b\frac{G}{d_p}\right)}\right) \tag{3.1}$$

The coefficients obtained from the fitting are shown in Table.3.2. The fitted coefficients a are in Table.3.2 are close to 1, suggesting the delay caused by the confinement tends to be 0 as the confining ratio increases. The coefficient b demonstrates the extent to which the confinement affects particle settling. In Table.3.2, b increases as the increase of particle size, reflecting in Fig.3.3 that larger particle size will have larger value of v_{plate}/v_s at a given G/d_p. Therefore, we can conclude that the particle size would affect the delay caused

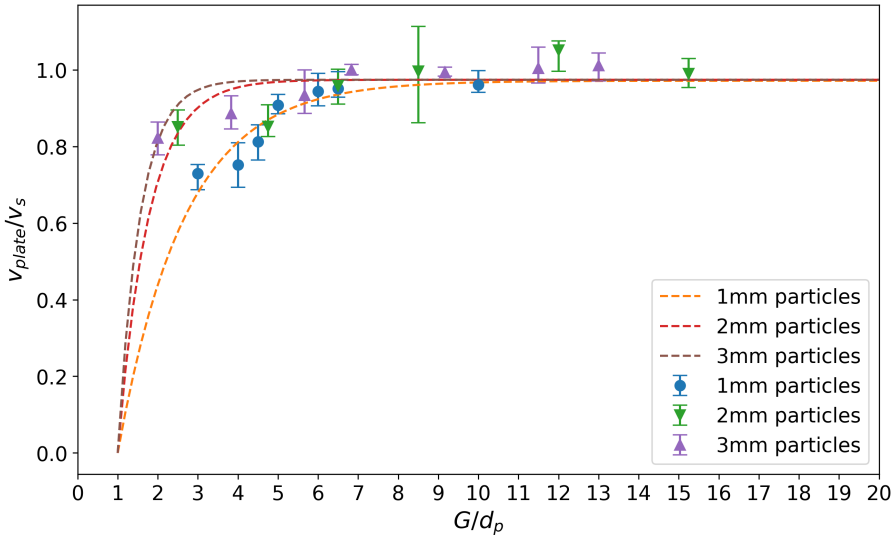

Figure 3.3: Velocity profiles with confining ratio

by confinement on their sedimentation. The larger the particle size, the relatively smaller delay induced by the confinement. In addition, v_{plate} is sensitive to minor experimental errors, such as variations in particle size (around 0.05mm), the sphericity of the particle, and viscosity changes (due to temperature), this produces a relatively larger standard deviation on the fitted value of b.

Table 3.2: The fitted value of coefficients

Particle size	a	b
1mm particle	0.97 ± 0.03	0.6 ± 0.08
2mm particle	0.97 ± 0.03	1.30 ± 0.37
3mm particle	0.99 ± 0.02	1.80 ± 0.32

3.3 Particle sedimentation in confined media with obstacles

In this section, we first introduce the experiment setup for the visualization of single-particle sedimentation in the porous medium. Then, we analyze the trajectories and corresponding velocity profiles to show the particle motion inside the medium and make a comparison among different cases. Next, we show the travel time for the corresponding conditions and give an explanation of particle delay induced by the obstacles.

3.3.1 Experiment setup

A porous medium is employed in this experiment. The sketch of the medium and injection box are shown in Fig.2.8. The obstacles are set on a plate, which is installed in a transparent container. The single particle sedimentation process in the media is recorded by the camera in front. To see the sedimentation behavior under different conditions, we have chosen to fix $e_x = e_z$ and varied them from 10 mm, 9 mm to 8.5 mm to form three porous media structures; three particle diameter (d_p) are used respectively: 1 mm, 2 mm, and 3 mm. For each combination of d_p and $e_x = e_z$ (except d_p=3 mm and $e_x = e_z$=8.5mm, because the corresponding e_p very close to d_p and particle will be blocked directly), 20 times injection of single particle are conducted but with different random locations (x_{in}) to show the influence of injection position. The relevant parameters of this experiment are shown in Table.3.3.

Table 3.3: Experiment parameters for single particle sedimentation in confined media with obstacles

Liquid	μ	0.023	Pa · s
	ρ_l	1181	kg/m^3
Particle	ρ_p	2470	kg/m^3
	d_p	1, 2, 3	mm
Medium	$e_x = e_z$	M1: 10, M2: 9, M3: 8.5	mm
	D_f	10	mm
	e_p	4.14, 3.44, 3.08	mm
	G	1.5, 3, 4.5 ($1.5d_p$)	mm
Recording	S	15.6	$pixel/mm$
	f	110	Hz

3.3.2 Particle sedimentation behavior inside medium

Firstly, we chose M1 and 1 mm particles to present the basic settling behavior of particles within the medium. Fig.3.4 illustrates the settling trace and corresponding normalized velocity profile of a 1 mm particle in M1. To display those around each row of pillars, we successively enlarge the trajectory and velocity profile on the left side of Fig.3.4 (a) and Fig.3.4 (b). We can observe that except for the difference in the trace at the first row (z_1), the trace and velocity profile of the particle have the same trend from z_2 to z_6. And due to the symmetry of the medium, the motion of the particle in the second and fourth rows (from z_2 to z_6) is symmetrical with the motion of the particles in the third and fifth

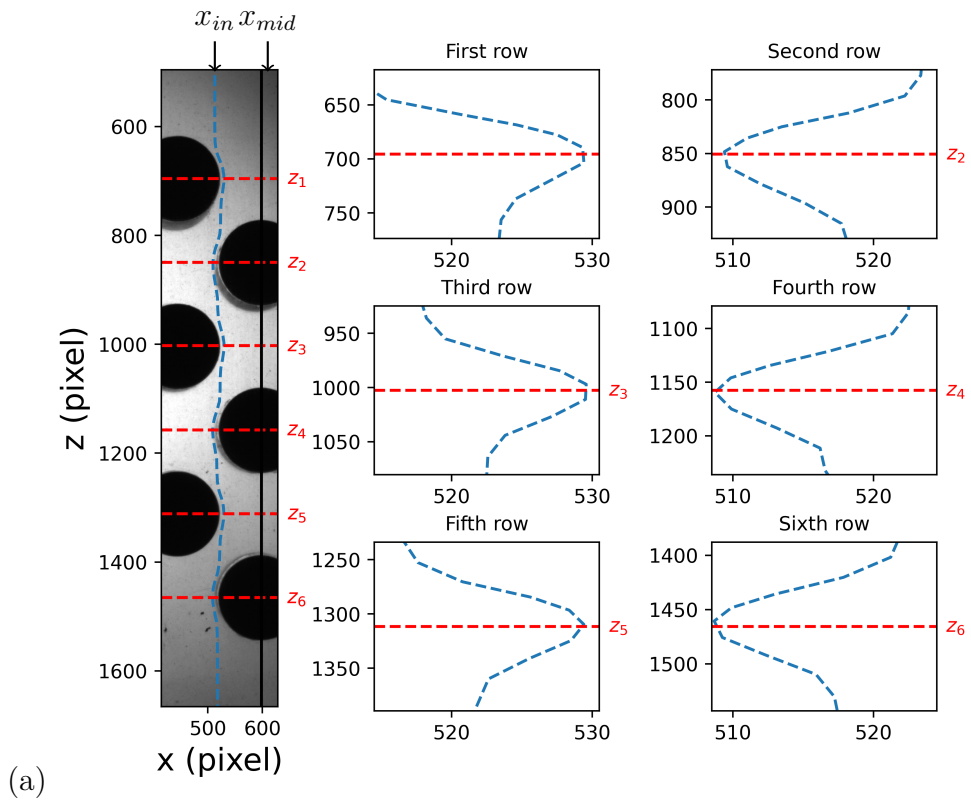

(a)

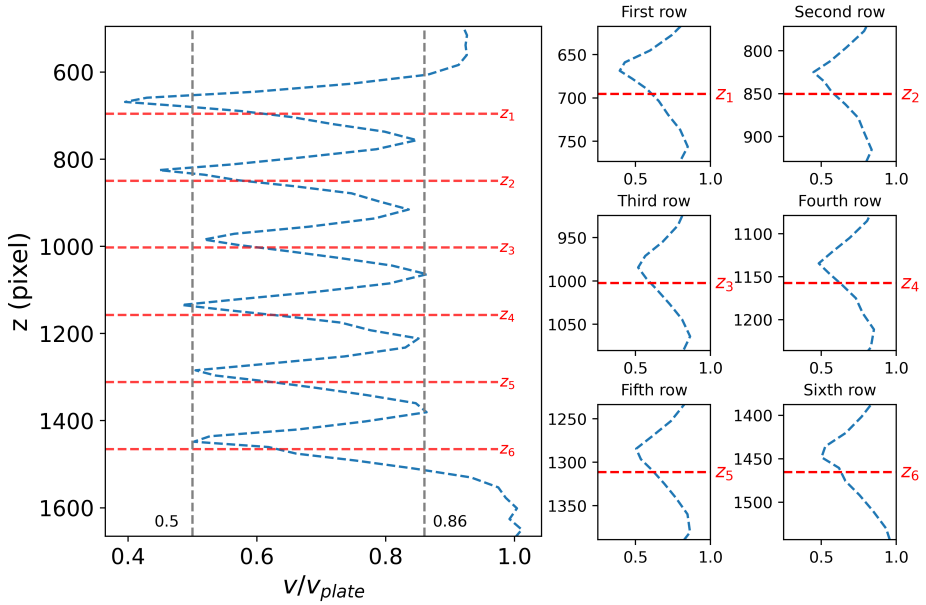

(b)

Figure 3.4: (a) Trajectory; (b) Velocity profile for a single 1 mm particle in M1; The vertical solid black line in (a) is the middle of medium (x_{mid}); the z_1, z_2, ..., z_6 correspond to the center height of each row of pillars; The curves within each row of pillars height in the left of (a) and (b) are successively enlarged to the plots on the right.

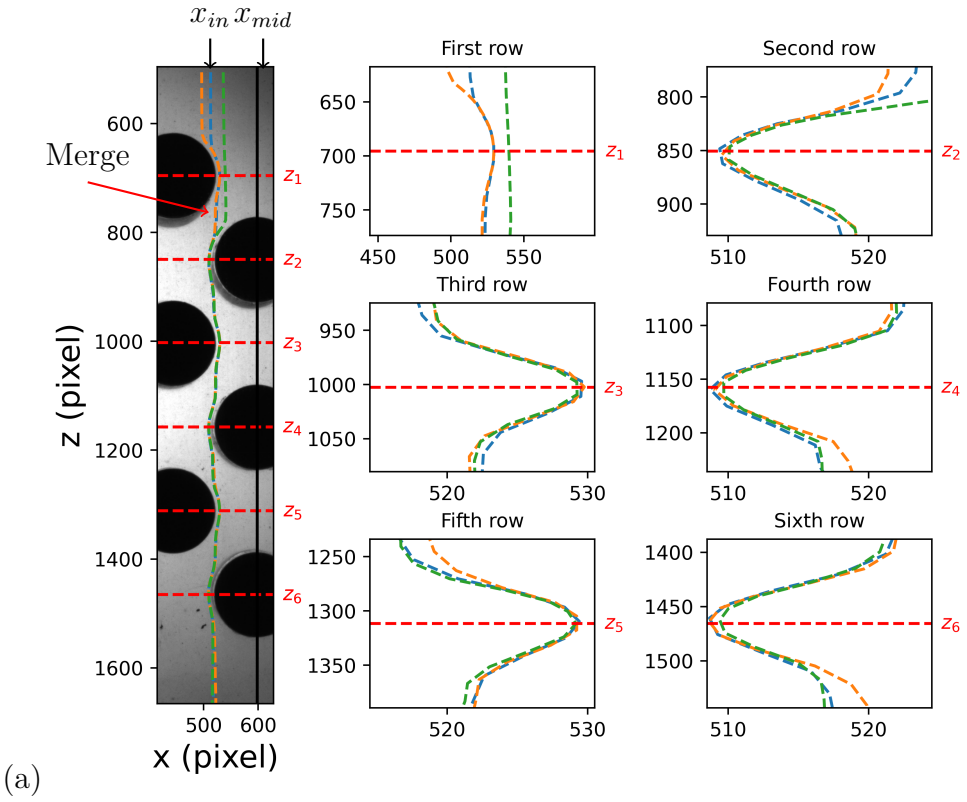

(a)

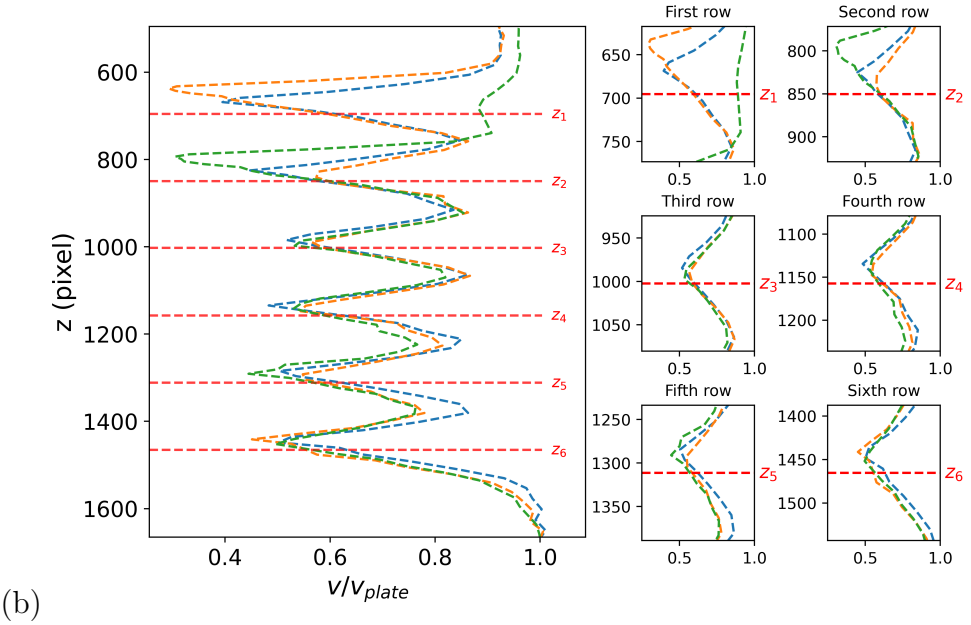

(b)

Figure 3.5: (a) Trajectories; (b) Velocity profiles under different injection positions (x_{in}, three particles were selected to serve as samples.) for 1 mm particle and M1; The vertical solid black line in (a) is the middle of medium (x_{mid}); the z_1, z_2, ..., z_6 correspond to the center height of each row of pillars. The curves within each row of pillars height in the left of (a) and (b) are successively enlarged to the plots on the right. The dashed lines and points lines of traces and velocity curve are to show the different injection positions (x_{in}).

rows. The trace oscillates back and forth in the range of x coordinate between 508-530 pixels and v/v_{plate} oscillates in the range of 0.5-0.86 (from z_2 to z_6). This shows that the motion of the particle through each row of pillars within the porous medium (from z_2 to z_6) follows the same behavior. Due to the symmetry of the medium, the particle makes a symmetric periodic settling motion within the medium. When the medium was changed to M2 and M3 with different combinations of particle sizes (2 mm, 3 mm), we all observed similar periodic motion as well as symmetry phenomena.

Because of this symmetry and periodic motion, we further enlarged the trace as well as the velocity profile at the fourth row (z_4) to show the basic characteristic of the particle motion at each row, which are shown in the top subplots in Fig.3.6. The motion of the particles through the pillar can be divided into two segments: the deceleration from B1 to D1 to approach the pillar and the acceleration from D1 to G1 to leave the pillar. At point B1, the particle has the maximum v/v_{plate} and the velocity is mainly in the z-direction, with a velocity in the x-direction of 0. After that, under the mechanical interactions, v_y/v_{plate} starts decreasing, $|v_x/v_{plate}|$ gradually increases, and thus the trace shifted to the left. At C1, v_y/v_{plate} continues decreasing and $|v_x/v_{plate}|$ reaches the maximum and start to decrease. At D1, which is a little higher than the middle of the pillar center height (z_4 or E1), both v_y/v_{plate} and v/v_{plate} reach minimum, and the deceleration process is completed.

Thereafter, the particle starts to accelerate. After D1, v_y/v_{plate} starts increasing and $|v_x/v_{plate}|$ continues decreasing, showing the deceleration movement toward the left. At E1, the center height of the pillar, $|v_x/v_{plate}|$ is close to 0 and it will increase just after the height. Thus, the particle trajectory begins to be shifted towards the direction of the pore throat again. At point F1, $|v_x/v_{plate}|$ reaches a maximum value and begins to decrease. Thus, the degree of offset of the trace begins to decrease and the trace gradually approaches vertical. Until G1, $|v_x/v_{plate}|$ is 0 , v/v_{plate} and v_z/v_{plate} reach their maximum values. The particle completes the acceleration process and starts the next cycle (G1 is the A1 for the next cycle).

Based on the above kinematic data, we next give a possible explanation of the settling process. From B1 to D1, as the particle gradually approaches the pillar, the fluid resistance between the particle and pillar will make the particle move toward the left. However, due to the more pronounced effect of gravity, the gap between particle and pillar side continues decreasing. This is why the curvature of the trace is gradually close to that of the pillar side. D1 is the potential contact point between the particle and pillar, and thus, the

particle will reach minimum velocity. Then, it will slide along the pillar surface. After E1, the gap between the particle and pillar will increase again due to the particle's inertia. At this time, the fluid around the particle will make the particle move towards the right, corresponding to an increase in v_x. As the particle continues settling (the gap of particle and pillar increasing), the fluid will resist particle horizontal motion, this is why the trace will become vertical gradually from E1 to G1. During the whole process, the most left the particle can reach is at E1 under the mechanical interactions. This could explain why the trace oscillates back and forth in the range of x coordinate between 508-530 pixels in Fig.3.4.

Fig.3.5 illustrates the settling traces and corresponding velocity profiles of 1 mm particles at different injection positions in M1. Due to the symmetry of the medium, we chose the left part of the medium for this description. The particles' trajectories at different injection positions (x_{in}) will gradually decelerate and merge at the aperture between the first and second rows. Similarly, we successively enlarge the trajectories and velocity profiles of each row and display them on the left side of Fig.3.5 (a) and Fig.3.5 (b). We can observe that the traces and velocity profiles of particles injected at different x_{in} will overlap and generally show the same trend at each row of pillars (from z_2 to z_6). Due to the symmetry of the medium, the motion of the particles in the second and fourth rows is symmetrical with the motion of the particles in the third and fifth rows. The small difference among them could be due to the experiment errors, such as in particle sphericity, size, and roughness. These results could indicate the same behavior for the motion of the particles through each row of pillars within the porous medium (from z_2 to z_6). When the medium was changed to M2 and M3 with different particle sizes (2 mm, 3 mm), we all observed similar periodic motions as well as symmetry phenomena. Thus, the injection position would not influence the particle sedimentation inside the medium.

Under different conditions (medium, particle size), the behavior of the particles is modified gradually on this basis, which is also described in detail next.

3.3.3 Particle sedimentation behavior for different particle size

Since the settling motion of particles is periodic and symmetric. Therefore we choose the settling process at the z_4 to compare the effect of different parameters. Fig.3.6 illustrates the settling traces and velocity profiles of 1 mm, 2 mm, and 3 mm particles at the fourth row of pillars in M1. We can find that for different particle sizes, their passage through each row of pillars also consists of two segments of motion with the same characteristic

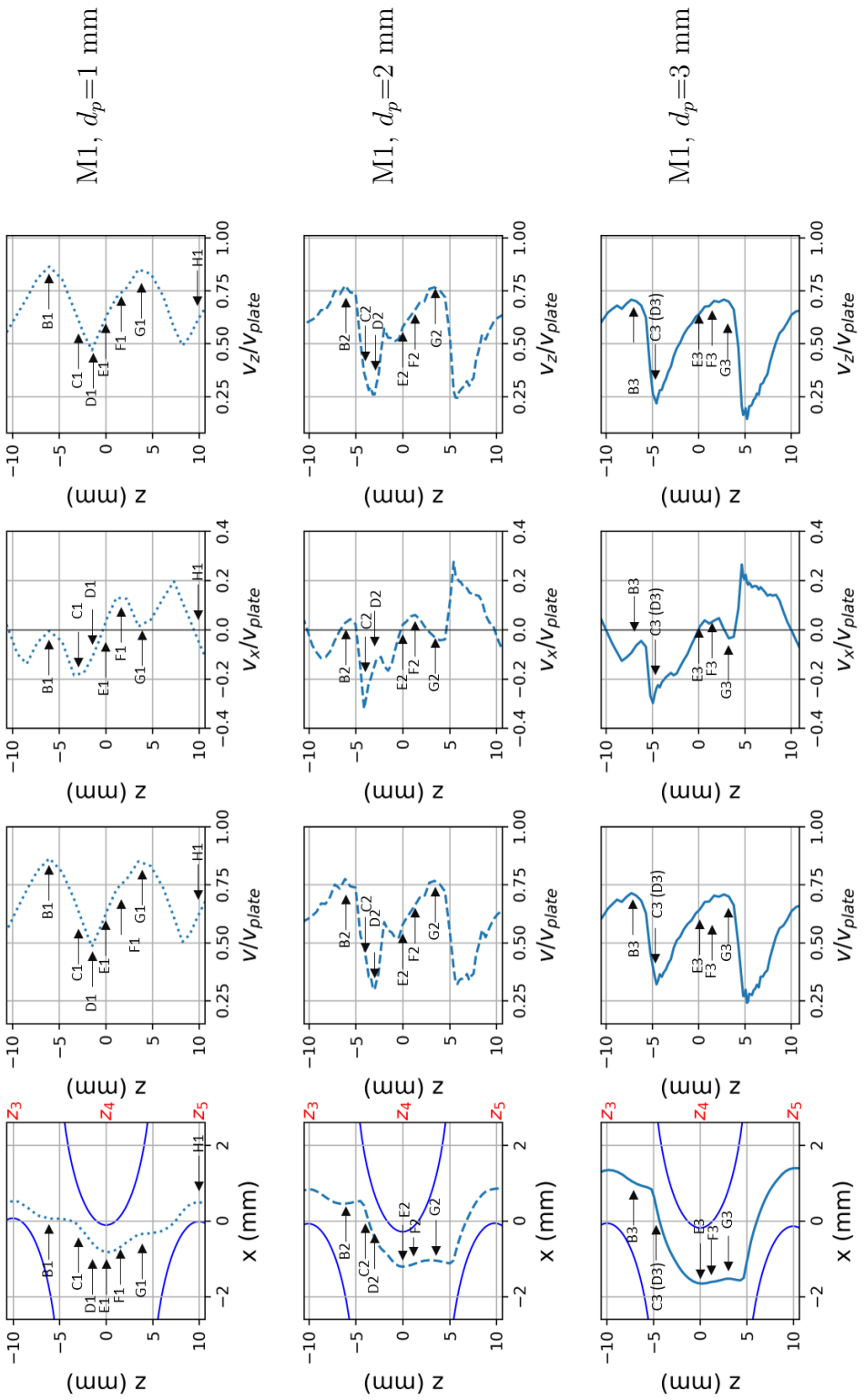

Figure 3.6: Trace and velocity profiles of particles passing fourth row for different particle sizes in M1 (from top to bottom: 1 mm, 2 mm, 3mm); The blue curves are the boundary of surrounding pillars; Each column of subplots have the same actual size scale (same blue circle); The axis of $x(pixel)$ is scaled up to show the curve between the cylindrical gaps; The coordinates in each subplot is normalized by the center position (0,0). Note: In the figure, the x-axis scale is enlarged to show the motion behavior of the particles in the x-axis direction. Fig.3.5 shows the true trace at scale x:z=1:1.

points. For the 2 mm particle, it decelerates in the B2-D2 segment to approach the pillar and then accelerates away in the D2-G2 segment; for the 3mm particle, it decelerates in the B3-D3 segment and accelerates in the D3-G3 segment. Points B2, B3 and G2, G3 correspond to the maximum v/v_{plate} and v_z/v_{plate} between the pillar gap. Points D2 and D3 correspond to the minimum v/v_{plate} and v_z/v_{plate} at the upper part surface of the pillar.

However, as the particle size increases, it changes the position of the special points during acceleration and deceleration, which in turn leads to the difference in the settling process for different particle sizes. First of all, during deceleration, when we increase the diameter of the particle, it makes all the motion feature points move towards the upper right corner of the image: like B1-B2-B3, C1-C2-C3, D1-D2-D3. v_x produces a lateral movement of the trace towards the pore direction during the process of B1-C1, B2-C2, and B3-C3. And the corresponding $|v_x/v_{plate}|$ maxima at C1, C2, C3 increase gradually with particle diameter. This means that larger particles would have larger lateral velocities. However, due to the small offset of B1, B2, and B3 and larger particle sizes (larger geometric blockage), the particles will reach C1, C2, and C3 at the higher part of the pillar. Next, we can see the larger the particles, the shorter the distance in the process of C1-D1, C2-D2, and C3-D3. Also as a result, D1, D2, and D3 will gradually move up to the upper right and the v/v_{plate} at these points will gradually decrease. This may be caused by the inertia of larger particles.

For the acceleration process, at D1-E1, D2-E2, and D3-E3, all different particle diameters will settle along the surface of the pillar. The $|v_x/v_{plate}|$ at the height of the pillar center (E1, E2 and E3) are all zero. At this point, E1, E2, and E3 are the most left due to the physical block of the pillar on the particle. Thereafter, $|v_x/v_{plate}|$ starts to increase again. And the maximum $|v_x/v_{plate}|$ at F1, F2 and F3 decrease. This shows that the larger the particle diameter at this point, the less lateral velocity towards the pores between E1-G1, E2-G2, and E3-G3. Thus, resulting in G1, G2, and G3 moving upward to the left. This is also the reason why B1, B2, and B3 move towards the upper right (symmetry of the medium). In addition, the maximum v/v_{plate} at G1, G2 and G3 also decrease gradually.

Overall, for different particle sizes, the geometric blockage between particles and pillars is the main factor affecting particle sedimentation. The more produced effect of gravity makes particle slides along the pillar side. At E1, E2, and E3, as the diameter of the particles increases, it makes the particle further to the left. The horizontal velocity (v_x/v_{plate}) causes the particles of different diameters to move toward the pore throat, which in turn

reduces the blockage of the pillars. But none of this lateral displacement can completely avoid the blocking of the pillar. Thus, for large particle size, it will slow down at the upper part of the next row of pillar, reach the most right at pillar height, and start the next cycle. This characteristic restricts larger particle settling in a lower velocity range (v/v_{plate}), making a larger delay on the particle. Fig.3.8 plots the traces as well as velocity profiles for different particle diameters in M2 and M3. We can see that the particle diameter has the same effect on the motion of the particles in different media.

3.3.4 Particle sedimentation behavior in different medium

Fig.3.7 shows the settling traces and velocity profiles of different particle diameters at the fourth row of pillars in different mediums. For particle motion in M2 and M3, We can find the particle passage through each row of pillars also consists of two segments of motion with the same characteristic points. In M2, it decelerates in the B4-D4 segment to approach the pillar and then accelerates away in the D4-G4 segment; in M3, it decelerates in the B5-D5 segment and accelerates in the D5-G5 segment. Points B4, B5 and G4, G5 correspond to the maximum v/v_{plate} and v_z/v_{plate} between the pillar gap. Points D4 and D5 correspond to the minimum v/v_{plate} and v_z/v_{plate} at the upper part surface of the pillar.

But again, the change in the structure of the medium changes the location of the special points, which in turn leads to differences in the settling process. First of all, during deceleration, when we decrease e_x, it also makes all the motion feature points move towards the upper right corner of the image: like B1-B4-B5, C1-C4-C5, D1-D4-D5. v_x produces a lateral movement of the trace towards the pore throat direction during the process of B1-C1, B4-C4, B5-C5. However, due to the offset of B1, B4, and B5, the particle will reach C1, C4, and C5 at the higher part of the pillar. Also as a result, D1, D4, and D5 will move to the upper right and the velocities at these points will decrease.

For the acceleration process, at D1-E1, D4-E4, and D5-E5, particle will settle along the surface of the pillar in all three mediums. The $|v_x/v_{plate}|$ (E1, E4, and E5) at the height of the pillar center are all zero. At this point, E1, E4, and E5 are moved to the left due to the decrease in e_x, resulting in G1, G4, and G5 moving upward to the left. In addition, the maximum v/v_{plate} at G1, G4 and G5 also decrease.

Overall, the influence of porous medium structure on particle sedimentation is the same as that of particle size, and the main factor is the geometric blockage between particle and

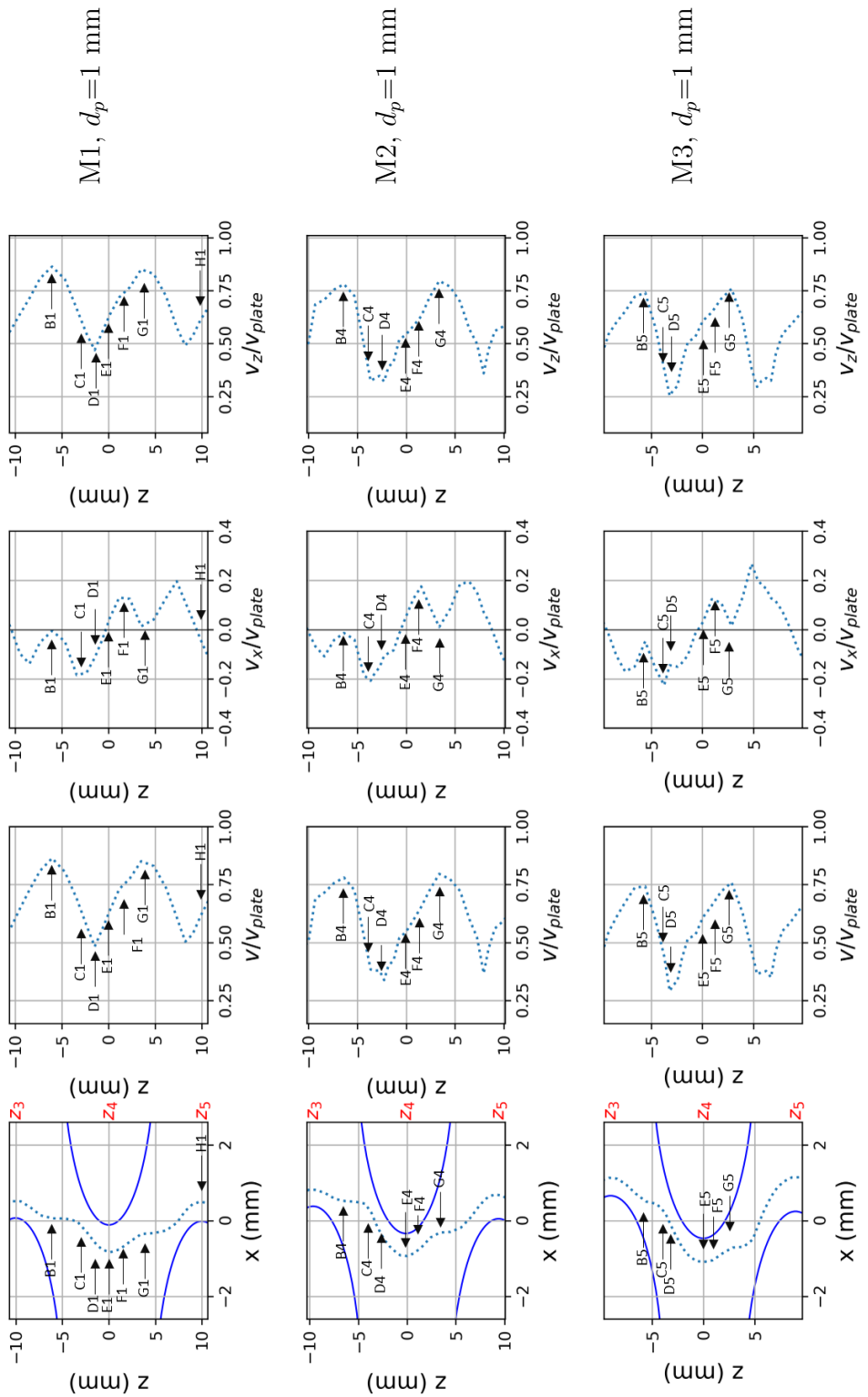

Figure 3.7: Trace and velocity profiles of particles passing fourth row for 1 mm particle in different media; The coordinates in each subplot are normalized by the center position (0,0). Note: In the figure, the x-axis scale is enlarged to show the motion behavior of the particles in the x-axis direction. Fig.3.5 shows the true trace at scale x:z=1:1.

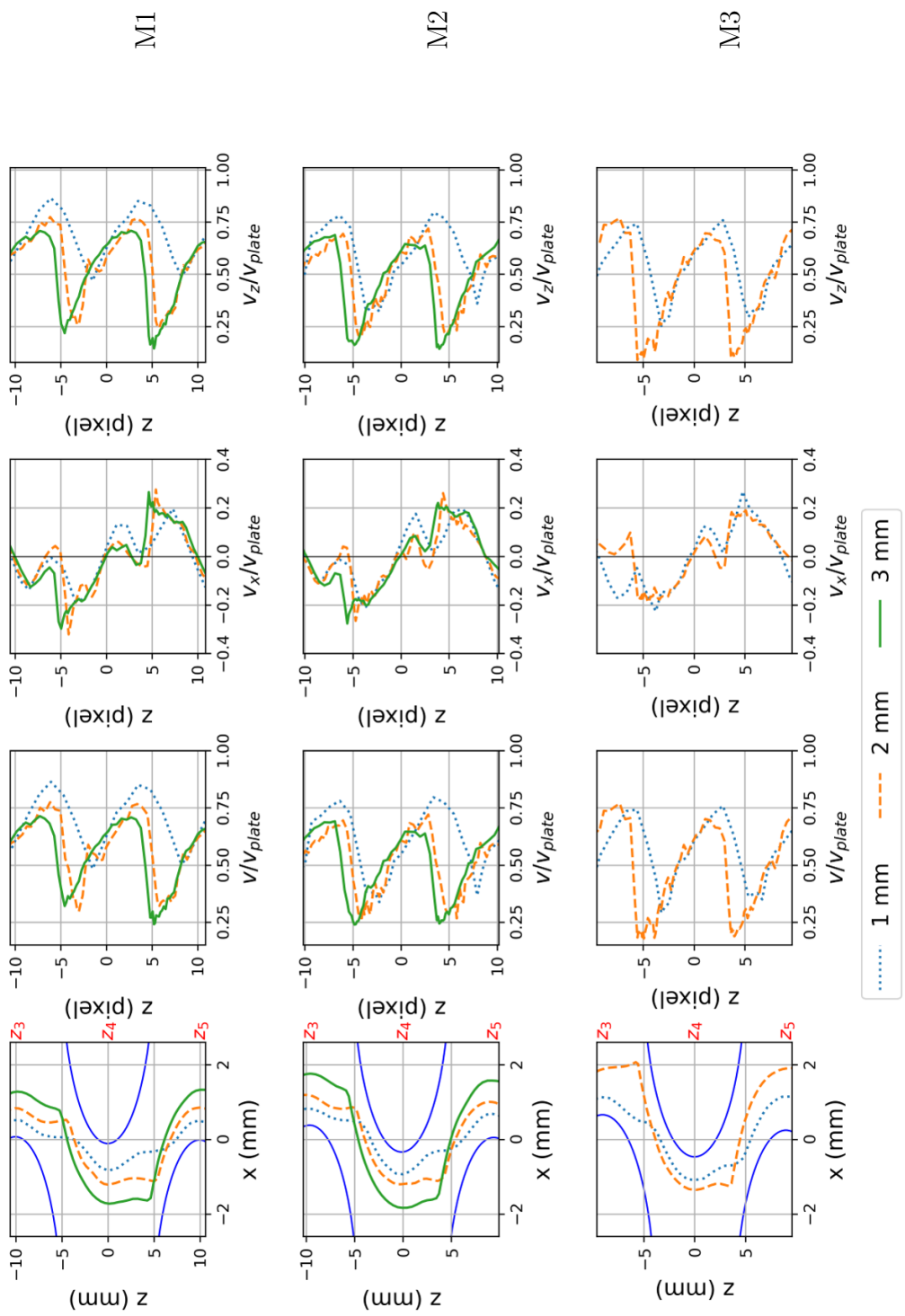

Figure 3.8: Trace and velocity profiles of particles passing the fourth row for different particle diameters in different media; The coordinates in each subplot are normalized by the center position (0,0). Note: In the figure, the x-axis scale is enlarged to show the motion behavior of the particles in the x-axis direction. Fig.3.5 shows the true trace at scale x:z=1:1.

pillar. Decreasing e_x would increase such blockage and push particle toward more right or left (like E1, E4, E5). This makes particle slow down at the upper part of the next row of pillars, and in turn, restricts particle settling in a lower range of velocity and induces a larger delay. Fig.3.8 plots the traces as well as velocity profiles in different mediums for different particle diameters, which shows the same tendency when we change the medium for 2 mm and 3 mm particles.

3.3.5 Particle travel time across the media

Fig.3.9 illustrates the time taken for different particle sizes to pass through the entire media area (from $z_{start} = z_1$ to $z_{end} = z_6$) at different injection positions in M1. The horizontal coordinates $|x_{in} - x_{mid}|$ are to show the lateral distance of the injection position to the center of the medium (x_{mid} and x_{in} are showed in Fig.3.5). The absolute value of $|x_{in} - x_{mid}|$ presented here is because the variation of injection point coordinates x_{in} can be less or greater than x_{mid}. We can see that the normalized travel time taken by the particles will gradually decrease as the injection position moves away from the center of the porous media. And whether $x_{in} - x_{mid}$ is greater than 0 or less than 0 (injected at right or left), $|x_{in} - x_{mid}|$ follows the same decreasing trend. This shows the symmetry of particle movement on both sides. Also, different particle sizes show a similar decreasing trend. This decreasing trend gradually becomes weaker where $|x_{in} - x_{mid}|$ is around 5, which is equal to $e_x/2$ of M1. We observe the same behavior in M2 and M3, and the coordinates of $|x_{in} - x_{mid}|$ corresponding to the disappearance of the decreasing trend are also around 4.5 and 4.25, $e_x/2$ for M2 and M3.

Fig.3.10 illustrates the travel time for 1 mm particles to pass through each pore region at different injection positions in M1. Pore 1 corresponds $z_{start} = z_1$ to $z_{end} = z_2$, and so forth. We can see that at pore 1, when $|x_{in} - x_{mid}|$ is close to 0, the particles take more time to pass through the pore region. This is attributed to the fact that when particles are injected at the center of the medium, they contact the point directly above the pillar (in the middle of the inlet), consequently impeding the particle's sedimentation. Whereas, as $|x_{in} - x_{mid}|$ increases, the particle will pass the inlet at the side of the middle pillar, and t_p^* decreases, which indicates particle can pass through more quickly. At around $|x_{in} - x_{mid}| = 5$, the travel time of pore 1 is not significantly different from the travel time at the other pores. For pore 2-5, the travel time does not show significant variation with the change in $|x_{in} - x_{mid}|$. Moreover, at each specific value of $|x_{in} - x_{mid}|$, the travel

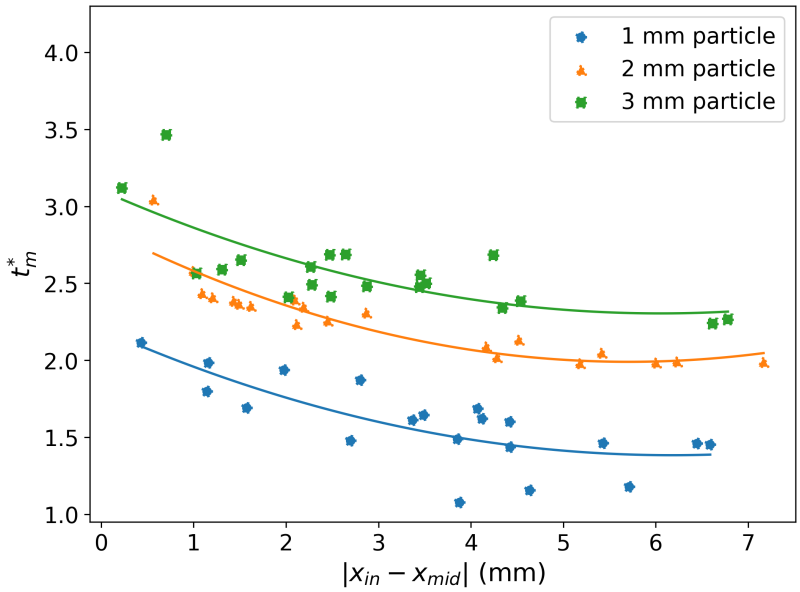

Figure 3.9: Travel time at medium scale for different particle size in M1 and different injection location; x_{in} is the x coordinate of the injection location; x_{mid} is the middle of medium, corresponding to the x coordinate of the solid black in the left side of Fig.3.4 (a); The curves are plotted by polynomial fitting.

times across these different pores also do not exhibit noticeable differences. In the case of different media and particles, we observed a similar behavior as here.

These results show that different injection positions lead to different travel times of the particles at pore 1, while it does not affect the motion of the particles inside the medium. At the same time, each particle has the same travel time along the same pore regions (pore 2 to pore 5) inside the medium, which also verifies that the particles are undergoing a periodic settling motion inside the medium as observed by the trajectories and velocity profiles.

3.3.6 Particle travel time for different d_p and media

Since the injection location does not affect the movement of the particles inside the medium. Therefore, as shown in Fig.3.11, we chose the $\bar{T}_p$ at the region of pore 4 (from $z_3 to z_4$ to show the effect of different particle diameters as well as the structure of the medium. The $\bar{T}_p$ donates the average of t_p^* among 20 tests. It can be seen that for each medium, as d_p increases, $\bar{T}_p$ also increases. At the same time, when we decrease the value

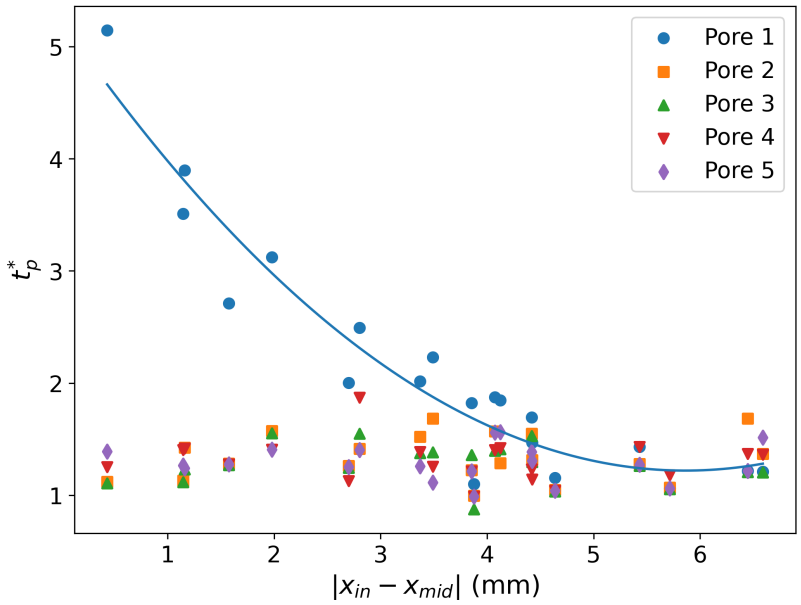

Figure 3.10: Travel time at pore scale for 1 mm particle in M1 and different injection location; The t_{plate} used here is smaller to that used for computation of t_m^*, so it will magnify the difference in t_p between particles.

of $e_x = e_z$ and increase the staggering between the pillars, $\bar{T}_p$ also increases. This is consistent with the phenomenon observed in traces and velocity profiles. Also, we can observe that the errors at 1 mm M1, 3 mm M1, and M2 are relatively large. For 1 mm particles and M1, the observed fluctuations in travel time might be attributed to the larger gaps between the pillars. Within this range, deviations in particle size can cause differences in the particle trajectories and velocity (as shown in Fig.3.5), ultimately resulting in fluctuations in travel time. In contrast, for 3 mm particles in M1 and M2, there is a greater overlap in their trajectories and velocities. The fluctuations in travel time for these larger particles may be due to the variations in contact with pillars and, consequently, in travel time.

3.4 Conclusion

By studying the settling behavior of a single particle between two plates, we find that the distance between the plates gradually constrains the movement of particles at the z-axis and retards the settling velocity of particles. The smaller the particle size, the delay will be relatively larger. For the particle motion in the porous medium, under our experi-

ment conditions, we found particle will do a periodical and symmetrical motion inside the medium. The injection position would not influence the particle motion inside the medium. Even the mechanical interactions will make the particle move toward the pore throat, but due to the more pounced effect of gravity, the particle will approach the pillar and slide along the pillar side. This makes the geometrical blockage between particle and pillar govern the characteristic in sedimentation. The larger particle size and smaller e_x increase the blockage of the pillar. This makes particles approach the upper part of the pillar and settle at a lower normalized velocity. Thus, the particle will experience more delay. At the same time, the effect of increasing particle size and decreasing e_x are comparable. These results give us some basic understanding of complex transportation and clogging phenomena.

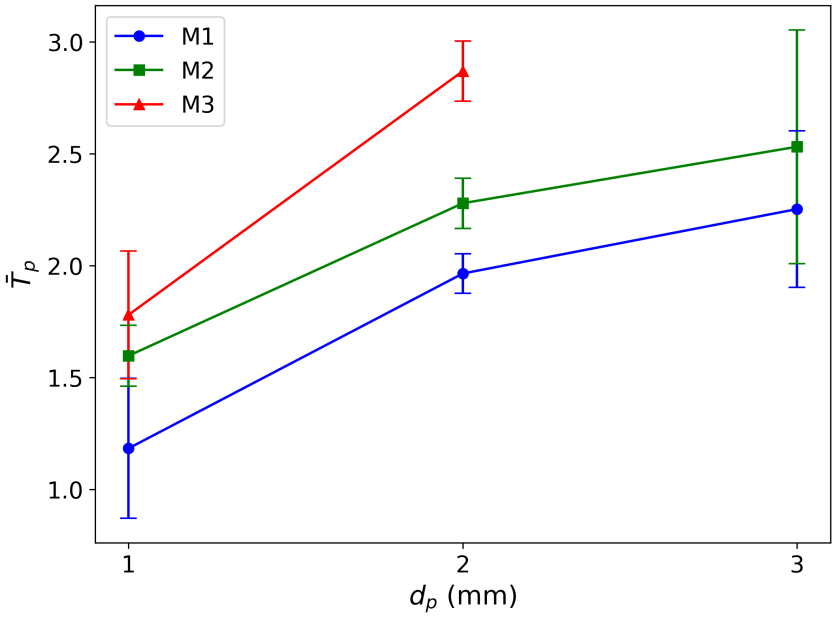

Figure 3.11: Travel time at pore 3 for different particle diameters and medium structures.

Chapter 4

Sedimentation behavior of particle group

4.1 Introduction

In the previous chapter, we investigated the settling motion of individual particles in different media structures and the caused delays. In this chapter, we gradually increased the number of injected particles ($N_{injected}$) and changed the particle size ratio (α, ratio between particle diameter and minimum pore size) to observe the motion behavior of multiple particles within different media structures and ultimately show the reasons for the occurrence of clogging. When we inject multiple particles at the same time, the particle trajectories and the velocity profiles are no longer varied with significant regularity as a single particle due to inter-particle pushing. Therefore, we demonstrate the settling process of the particles by the distribution of the concentration profile along the depth of the medium. This gives a characterization of the accumulation and dispersion of different $N_{injected}$ within the medium, while the maximum accumulation concentrations at different medium regions and α are further compared to show the effect of both. For the induced delay, the average travel time of particle population through the entire media region as well as each pore region under different $N_{injected}$ and α are further calculated to show their influence. Besides, an increase in $N_{injected}$ could cause the particles to clog the pores of the medium. By counting the number of particles entered, exited, and retained in the entire media region and each pore region, it shows a critical number of $N_{injected}$ ($N^c_{injected}$) existed that particles start to be retained and further indicates the distribution of deposited particles. Next, we directly show the particle motion at pore space for different $N_{injected}$ and α, which give a reason for the clogging occurrence at different parts of the medium and show the influence of these two factors. Finally, we estimate the clogging probability as it was defined in chapter 2 over 20 tests in the whole media region as well as in each pore region for different $N_{injected}$ and α. The settling characteristics of the particle population

in the medium and the process that ultimately leads to the occurrence of clogging in the medium area are well illustrated with these results.

4.2 Adjusted experimental setup

To observe the settling behavior of multiple particles in a porous medium and the occurrence of clogging, we used the assembly setup as shown in Fig.2.8. Both the assembled medium and injection box are immersed in the liquid to avoid air bubbles and surface tension. The injected particles are placed in advance inside the injection box, in sequence from the center to the sides. When the first space is filled, subsequent particles continue to be placed sequentially on top (as shown in Fig.2.8). By pulling back the sliding baffle, the particles will successively settle into the medium under the force of gravity. The settling behavior of the particles in the x-z plane of the medium is recorded by the camera for subsequent image analysis and data processing. In this experiment, three media configurations were used, corresponding to $e_x = e_z$ of 10, 9, and 8.5 mm in Fig.2.7, and three particle sizes were used, 1, 2, and 3 mm, respectively. For each medium and particle size, the number of injected particles ($N_{injected}$) was gradually increased until the clogging phenomenon occurred. For each configuration (specific combination of medium, particle size, and number of injected particles), the experiment was repeated 20 times. The parameters associated with the experiment are shown in Table.4.1 and the specific experiments performed with different variables are shown in Table.4.2.

Table 4.1: Experiment parameters of clogging experiment

Liquid	Viscosity of liquid	0.023	$\mathrm{Pa \cdot s}$
	Density of liquid	1181	$\mathrm{kg/m^3}$
Particle	Particle density	2470	$\mathrm{kg/m^3}$
	d_p	1, 2, 3	mm
Porous medium	D_f	10	mm
	$e_x = e_z$ (Fig.2.7)	10 (M1), 9 (M2), 8.5 (M3)	mm
	e_p (Fig.2.7)	4.14, 3.44, 3.08	mm
Box injection	L	20	mm
	W	1.5, 3, 4.5 ($1.5d_p$)	mm
	h	30	mm
Camera	Image scale	15.6	$pixel/mm$
	Image frequency (f)	110	Hz

Table 4.2: Relevant variables of the experiment conducted

d_p	Medium	$\alpha = \frac{d_p}{e_p}$	$N_{injected}$					
1mm	M1	$\alpha = 0.24$	40	80	120	200	300	400
1mm	M2	$\alpha = 0.29$	40	80	120	200	300	400
1mm	M3	$\alpha = 0.32$	40	80	120	200	300	400
2mm	M1	$\alpha = 0.48$	4	10	20	40	60	80
2mm	M2	$\alpha = 0.58$	4	10	20	40	60	80
2mm	M3	$\alpha = 0.65$	4	10	20	40	60	80
3mm	M1	$\alpha = 0.72$	4	10	20	40	60	80
3mm	M2	$\alpha = 0.87$	4	10	20	40	60	80

4.3 Concentration profile

4.3.1 Concentration profile with time

The concentration and its variation along the depth direction could help to investigate the accumulation or the dispersion of the particles during settling. This parameter is defined as the total apparent surface area of the particles divided by the surface area of the selected zone. Fig.4.1 shows the concentration profiles (c) as the particles settle (at different t) under different $N_{injected}$. For $N_{injected} \leq 20$, we observe the same trend. As particles are successively injected, certain c values are generated at pore 1 (depth = 10mm) in Fig.4.1 (a), (b), and (c). As t increases, the particles gradually pass through pore 1 and enter the interior of the medium, and the range of the c distribution increases. At the same time, a peak can be generated in the range of the distribution. As t continues to increase (the particles continue to settle), both the range of the c distribution and the peak move in the direction of depth. After the particles have completely left the medium, the c profile returns to 0. This shows that when multiple particles are injected simultaneously, the obstruction of the medium pillar will cause the particles to disperse and settle within a certain distance range. In Fig.4.1 (d), (e), and (f) ($N_{injected} \geq 40$), the c values resulting from particle settling significantly increase, indicating a higher degree of particle accumulation. Under these conditions, particles start to be retained. The retained particles produce a constant c at the retained depth. Thus, we will observe the appearance of two or more wave peaks: one due to the retention of particles, with a more intense distribution, and does not move with time anymore, and one due to the accumulation of settling particles, which is moving with time.

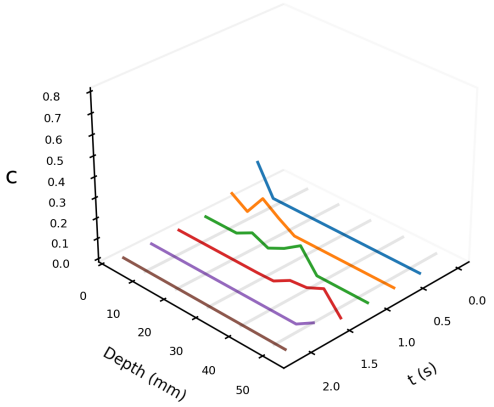

(a) 4 particles

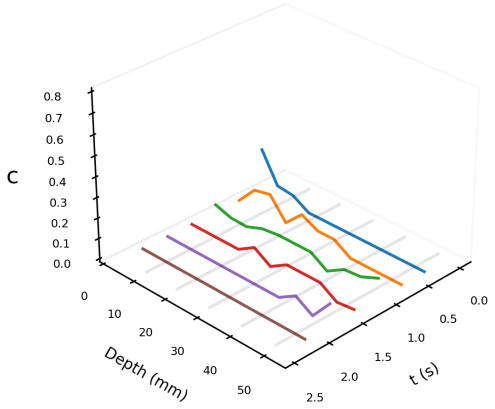

(b) 10 particles

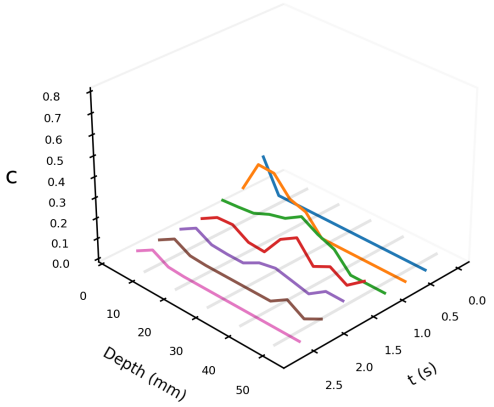

(c) 20 particles

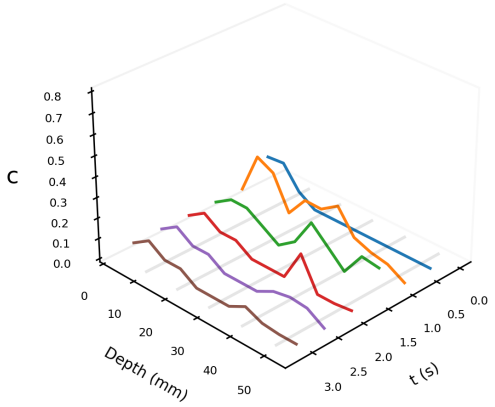

(d) 40 particles

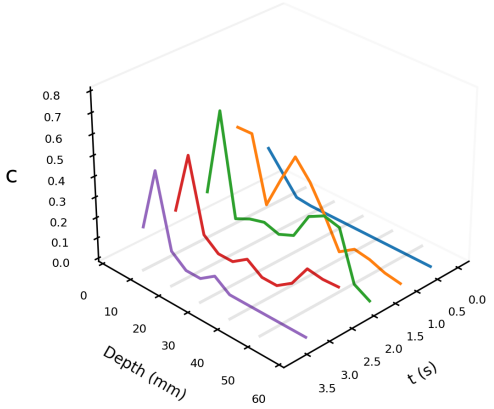

(e) 60 particles

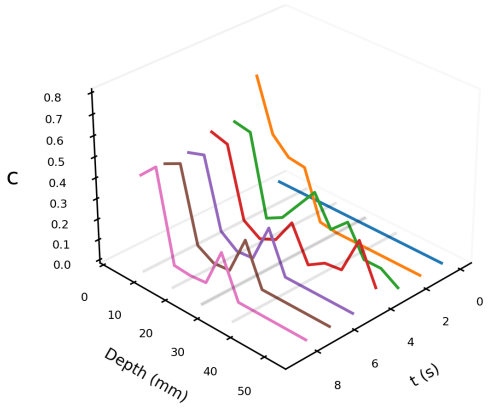

(f) 80 particles

Figure 4.1: Concentration profiles along depth with $\alpha = 0.48$ ($d_p = 2$ mm and $e_p = 4.14$ mm) and different $N_{injected}$; The center position (in depth) of pores are 10 mm, 20 mm, 30 mm, 40 mm, and 50 mm.

4.3.2 Maximum concentration produced during settling process

Fig.4.1 illustrates the spatial-temporal distribution of $c(z,t)$ under different conditions. In this section, we fixed the value of z and searched for the maximum concentration value at the corresponding position throughout the settling process (t from 0 to the time that all particles pass through). This indicates the degree of accumulation of particles in different regions. The areas are divided into $A1$, $A2$, ... $A12$, as showed in Fig.2.14. For $\alpha \leq 0.48$, we could see a similar trend with changes in $N_{injected}$. As shown in Fig.4.2 (a) - (c) with $N_{injected} = 40$ or Fig.4.2 (d) with $N_{injected} = 4$, a smaller c_{max} value is produced at each area and there is no significant variation between regions. This shows that at this point, the particles accumulate less in each region and do not vary with depth. As we increase $N_{injected}$ to 80 in Fig.4.2 (a) - (c) and 10 in Fig.4.2 (d), there is a large increase in c_{max} at A2, but after the particles pass through A2, c_{max} decreases significantly and remains essentially constant with depth. This shows that the particles will accumulate more at A2, but inside the medium, the particles will still accumulate to a lesser extent. Keep increasing $N_{injected}$, the c_{max} produced at the entrance (A2) and the internal pores will be significantly larger compared to those under smaller $N_{injected}$, and c_{max} at A3-A12 is relatively lower than A1, A2, which indicates that the particles could produce a large accumulation at A1 and A2 and this could be maintained along the medium depth to some extent. Besides, after passing A2, we have a greater chance of seeing larger c_{max} at A4, A6, A8, A10 and viewing relatively small c_{max} values in adjacent regions: A3, A5, A7, A9. This shows that due to the blockage of the pillars, the particles produce significant accumulation at the pore throat, while after passing, the degree of accumulation is reduced. At the same time, the particle population repeats this behavior continuously with depth. This implies the tendency to clog at different depths.
For $\alpha > 0.48$, in Fig.4.2 (e) - (f), we can find that as $N_{injected}$ increases, c_{max} increases significantly mainly at A1, A2, and in the inner region of the medium, there is a smaller change in the c_{max} value. This is because, at this point, the diameter of the pores (e_p) is close to the diameter of the particles (d_p), limiting the particles only to flow out of the pores one after another.

4.4 Particle travel time

In this section, we use the average travel time that the particle population passes through the target area (Fig.4.3) to show the particle delay induced by the different parameters.

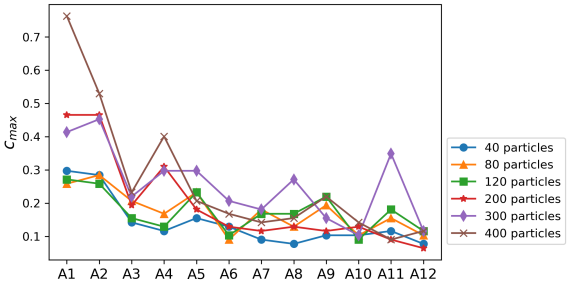

(a) $\alpha = 0.24$, $d_p = 1$ mm, $e_p = 4.14$ mm

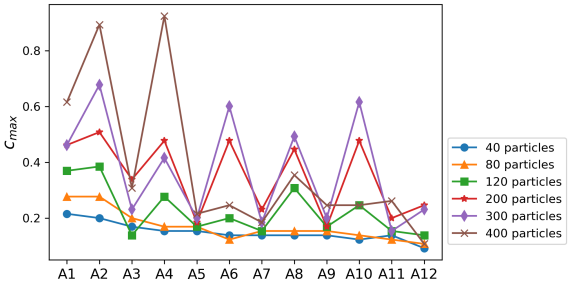

(b) $\alpha = 0.29$, $d_p = 1$ mm, $e_p = 3.44$ mm

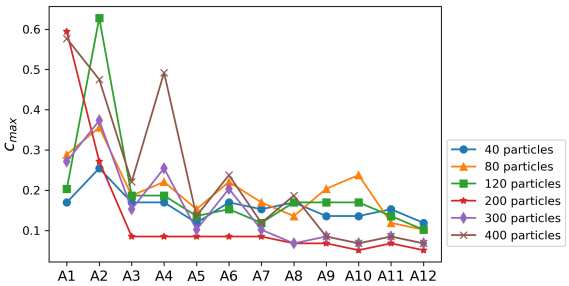

(c) $\alpha = 0.32$, $d_p = 1$ mm, $e_p = 3.08$ mm

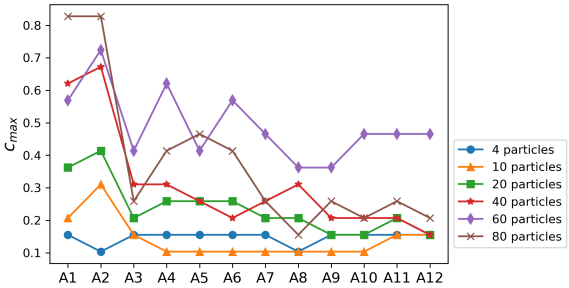

(d) $\alpha = 0.48$, $d_p = 2$ mm, $e_p = 4.14$ mm

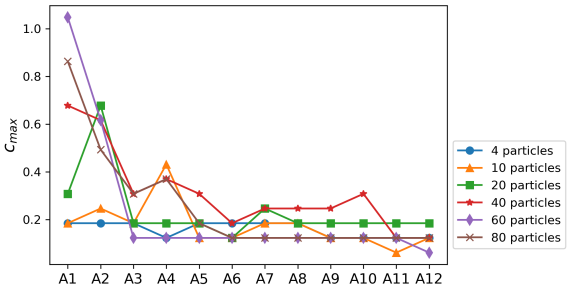

(e) $\alpha = 0.58$, $d_p = 2$ mm, $e_p = 3.44$ mm

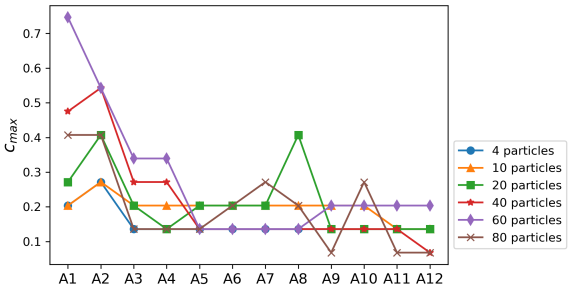

(h) $\alpha = 0.65$, $d_p = 2$ mm, $e_p = 3.08$ mm

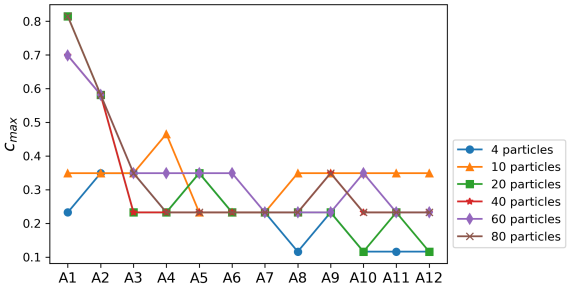

(g) $\alpha = 0.72$, $d_p = 3$ mm, $e_p = 4.14$ mm

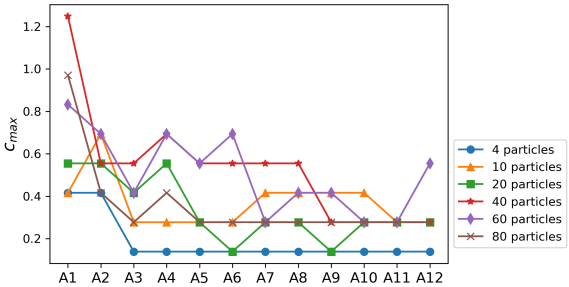

(f) $\alpha = 0.87$, $d_p = 3$ mm, $e_p = 3.44$ mm

Figure 4.2: The maximum concentration that is induced at area of $A1$, $A2$, ..., $A12$ during the sedimentation process under different $N_{injected}$ in a test.

The corresponding travel times are calculated as shown in Eq.2.23 and 2.24.

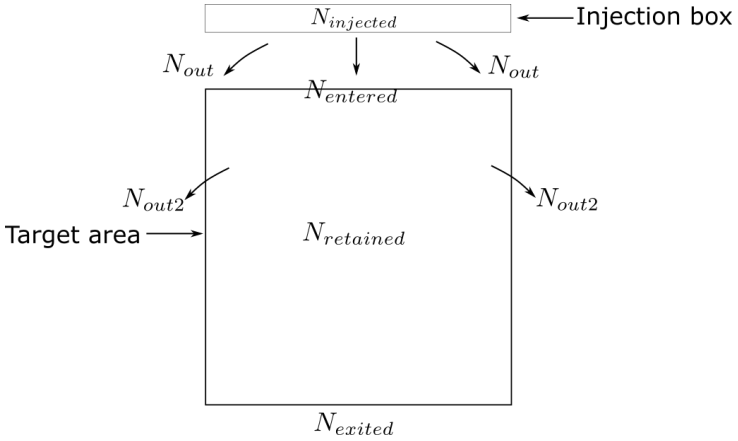

Figure 4.3: Schematic diagram of particle travel time calculation and particle number count at a target area.

4.4.1 Particle travel time through entire medium

Here, we set the target region (Fig.4.3) as the entire medium area to show the delay experienced by particles. Fig.4.4 shows the average time consumed by the particles to pass through the whole medium for different injected particle numbers ($N_{injected}$) and particle size ratios (α). For different α, we observe similar trends in the variation of $\bar{T}_m^*$ with $N_{injected}$. We take $\alpha = 0.48$ as an example for introduction. When $N_{injected}$ just starts to increase, $\bar{T}_m^*$ decreases gradually. When $N_{injected}$ reaches a critical value ($N_{injected}^c = 40$), $\bar{T}_m^*$ reaches a minimum. After that, $\bar{T}_m^*$ does not decrease. This shows that when we just start to increase the $N_{injected}$, it will reduce the delay of the particles and promote the particles to pass through the medium area. And after the $N_{injected}^c$, the delay will start increasing. As α increases, the curve will reach its minimum more quickly, corresponding to a decreasing $N_{injected}^c$.

Fig.4.4 (a), (b), (c) show the variation of $\bar{T}_m^*$ with $N_{injected}$ under different α (same d_p and different e_p), respectively. It can be seen that when the d_p and $N_{injected}$ are the same, decreasing e_p (increasing α in each subplot) could result in larger $\bar{T}_m^*$ values. This shows that for the same particle and $N_{injected}$, a larger α (smaller e_p) will always prevent the passage of particles. Similarly, larger d_p will increase the delay of the particles. In addition, the influence of d_p and e_p on the $\bar{T}_m^*$ is comparable. For example α= 0.58 and 0.72, corresponding $d_p = 2$ mm, $e_p = 3.44$ mm and $d_p = 3$ mm, $e_p = 4.14$ mm, there is

no significant difference in $\bar{T}_m^*$ corresponding to the same $N_{injected}$.

4.4.2 Particle travel time through each pore layer

In this section, we set each pore area in Fig.2.14 as the target area in Fig.4.3. Fig.4.5 shows the average travel time of particles at each pore for different numbers of injected particles and particle size ratios. Again, for each α, they have a similar trend, so we present it here as an example with α=0.48. When α is equal to 0.48, a single particle produces a large $\bar{T}_p^*$ at pore 1 and smaller values at pore 2-5, while the $\bar{T}_p^*$ values at pores 2-5 have no obvious change trend. Compared to individual particles, the increase in $N_{injected}$ (0-20) leads to a small decrease in $\bar{T}_p^*$ values at each pore. After $N_{injected} = 40$ (critical value), $\bar{T}_p^*$ at pore 1 no longer decreases and increases a little; at pores 2-5, $\bar{T}_p^*$ starts to increase significantly. This shows that when we just increase the value of $N_{injected}$, it promotes the passage of particles through each pore area. When $N_{injected}$ is greater than the critical value, it still promotes the particles to pass through the pore 1 area, but at pores 2-5, it will delay the particles significantly. Since different particle size ratios correspond to different critical $N_{injected}$, this results in different trends of $\bar{T}_p^*$ with $N_{injected}$ in each subplot. In addition to this, at each pore area, a larger α (larger d_p or smaller e_p) also leads to a larger $\bar{T}_p^*$ value. This is consistent with the results shown in at medium: the smaller pore size and larger particle diameter would induce a more serious delay on particles.

4.5 Particle number entered, exited, retained

In this section, we show the number of particles entered, retained, and exited the target area ($N_{entered}$, $N_{retained}$ and N_{exited}) and the number of particles out of the medium area (N_{out}) when injecting different numbers of particles ($N_{injected}$) under different conditions. N_{out} are the particles that do not enter the target area due to the push among particles and thus settle at both sides. Very few particles flow out at both sides of the target area (N_{out2}), so the corresponding number is set to 0. With this assumption, we can write:

$$N_{injected} = N_{out} + N_{entered} = N_{out} + N_{retained} + N_{exited} \tag{4.1}$$

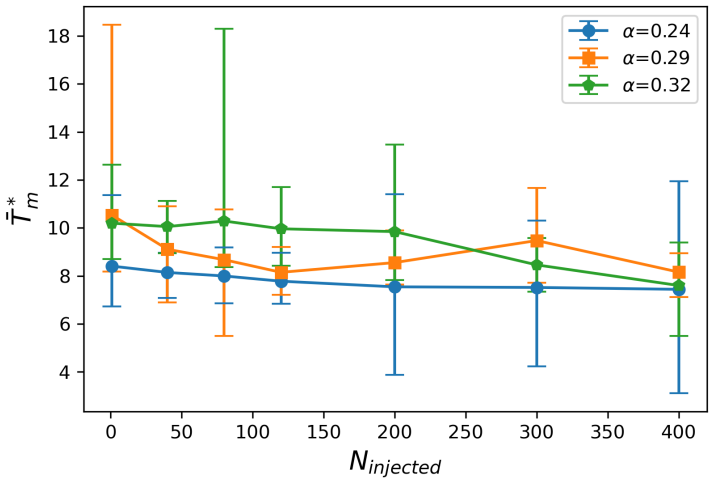

(a)

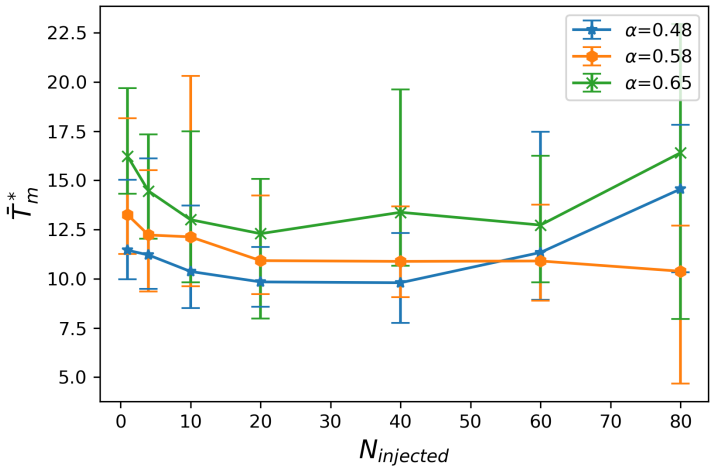

(b)

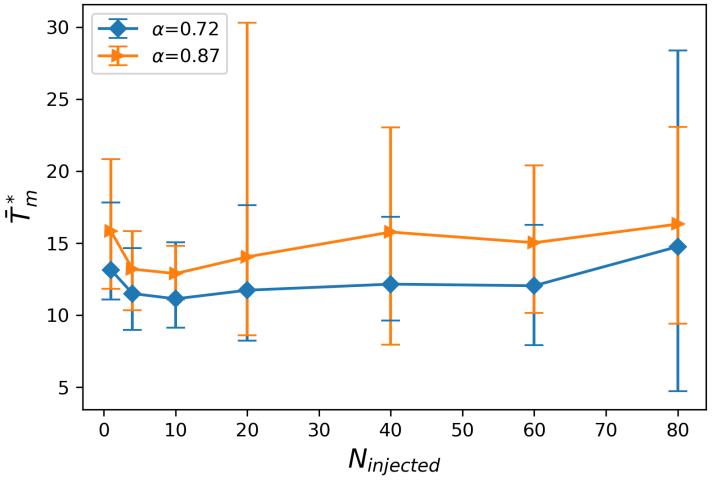

(c)

Figure 4.4: Travel time passing through the entire medium under different particle number injected and particle size ratio; (a) d_p=1 mm; (b) d_p=2 mm; (c) d_p=3 mm.

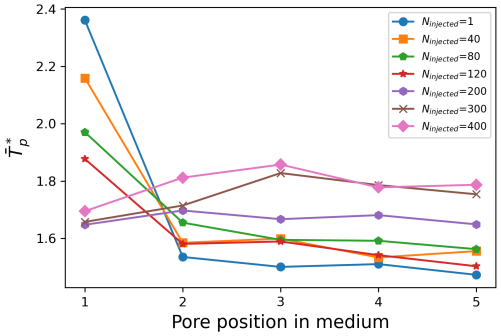

(a) $\alpha = 0.24$

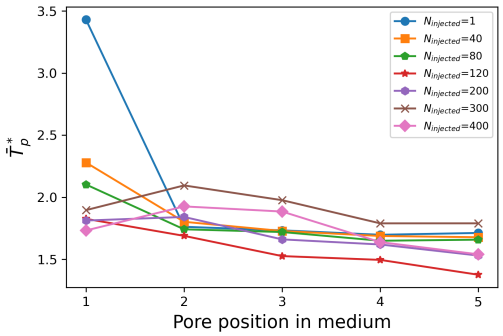

(b) $\alpha = 0.29$

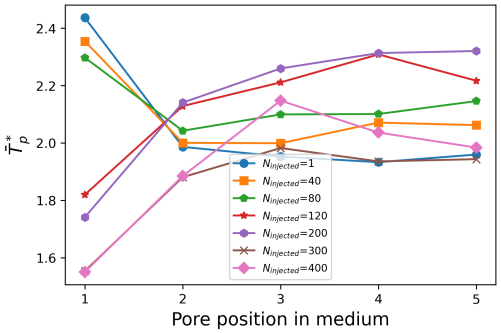

(c) $\alpha = 0.32$

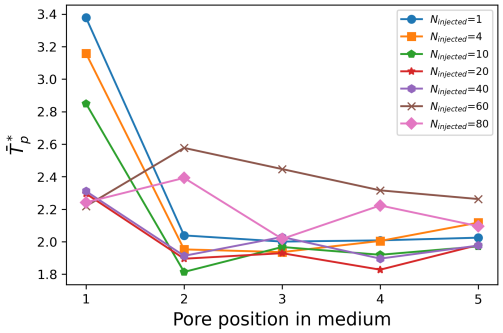

(d) $\alpha = 0.48$

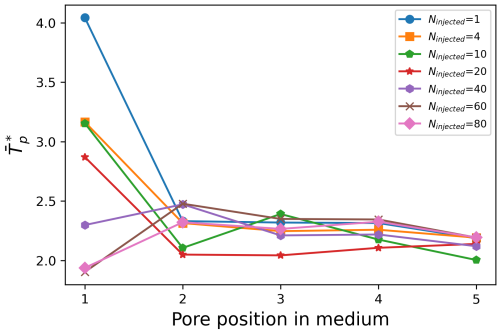

(e) $\alpha = 0.58$

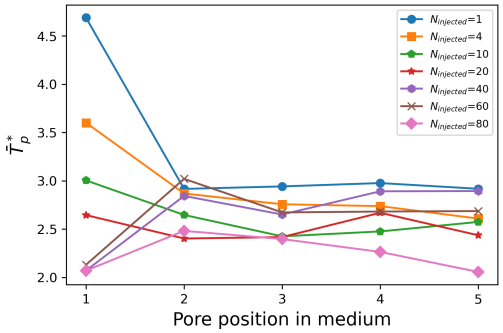

(h) $\alpha = 0.65$

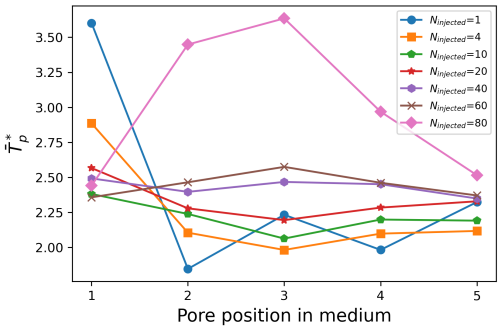

(e) $\alpha = 0.72$

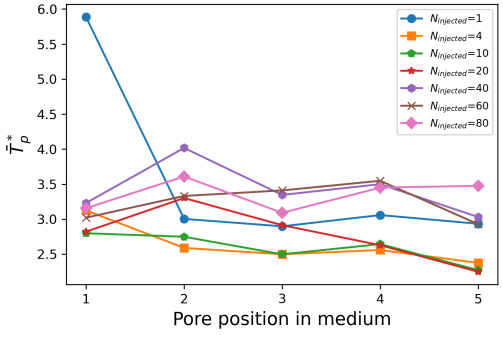

(h) $\alpha = 0.87$

Figure 4.5: Average particle travel time among 20 tests with different particle numbers injected at each pore area for different particle size ratios.

4.5.1 At medium

In this section, the entire medium region (shown in Fig.2.14) is treated as the target region in Fig.4.3 to study the inflow and outflow of particles. Fig.4.6 illustrates the variation of $\bar{N}_{entered}$, $\bar{N}_{retained}$ and $\bar{N}_{exited}$ over 20 tests with $N_{injected}$ for different particle size ratios. For each α, $N_{entered}$ increases gradually with $N_{injected}$ and, at the same time, the difference between the two increases gradually. This shows that as $N_{injected}$ increases, more particles enter the medium. However, due to the increase of inter-particle blocking, more particles will also flow out of the media region (N_{out}). Combining Fig.4.7, $\bar{N}_{exited}$ also starts to increase gradually with $N_{injected}$ and $N_{entered}$, and after $N^c_{injected}$, $\bar{N}_{exited}$ basically does not increase significantly. This shows that after the $N^c_{injected}$ (e.g., $\alpha = 0.48$, $N^c_{injected} = 40$), a critical $\bar{N}_{exited}$ is created - the number of particles that can pass through the medium region do not change anymore ($\bar{N}^c_{exited}$). Besides, Fig.4.7 shows the $\bar{N}^c_{exited}$ will increase with α. When α=0.24, the experimental setup had a slight unevenness in the front and back plates, which led to experimental errors (including inter-particle overlap for particle detection, particle injection, and retention, etc.), and thus the $\bar{N}^c_{exited}$ was less than that of $\alpha = 0.30$. The difference between the $\bar{N}_{entered}$ and $\bar{N}_{exited}$ is the $\bar{N}_{retained}$. And $\bar{N}_{retained}$ starts producing a significant increase at the $N^c_{injected}$. These results show that once we reach the $N^c_{injected}$, some particles will start to be retained inside the medium and clog the pores. As $N_{injected}$ continues to increase, subsequent particles, thus, are further retained. For different α, the $N^c_{injected}$ will gradually decrease as α increases, thus leading to different trends in each subplot. Meanwhile, Fig.4.8 demonstrates the $\bar{N}^c_{exited}/\bar{N}_{entered}$ under each α, in which $N_{entered}$ corresponds to the value when N_{exited} just arrive at critical value. It shows the closed values of $N^c_{exited}/N_{entered}$ under each α, which may indicate a similar clogging behavior.

4.5.2 At each pore layer

For each pore region, firstly, we counted the average number of particles entered over 20 tests. Then, we normalized the values by the $\bar{N}_{entered}$ at the pore 1, which is further used to show the penetration of the particle population relative to the total particles that can enter the medium ($\bar{N}_{entered}$ at the pore 1).

$$\Phi = \frac{\bar{N}_{entered}}{\bar{N}_{entered} \text{ at pore 1}} \tag{4.2}$$

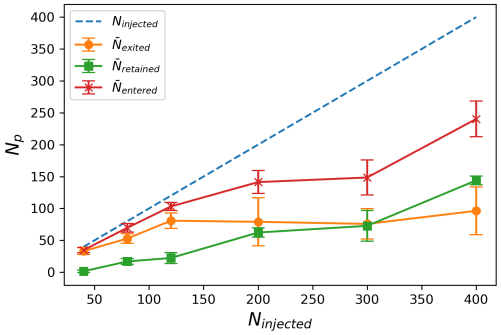

(a) $\alpha = 0.24$

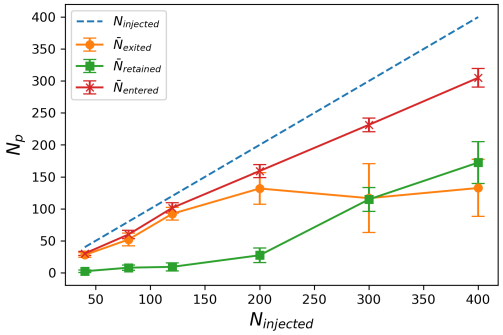

(b) $\alpha = 0.29$

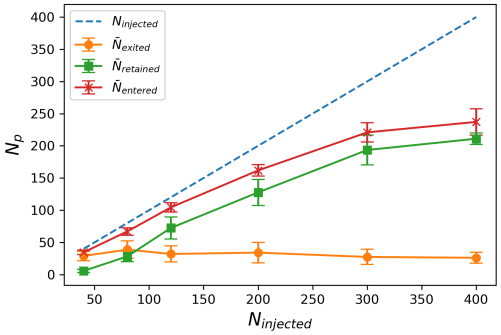

(c) $\alpha = 0.32$

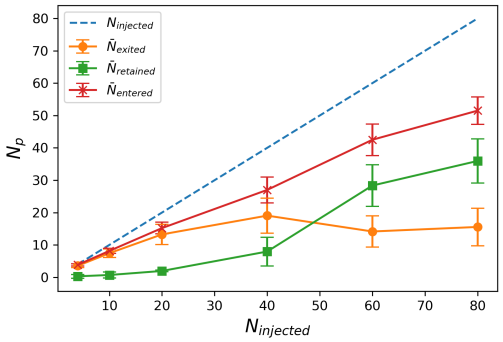

(d) $\alpha = 0.48$

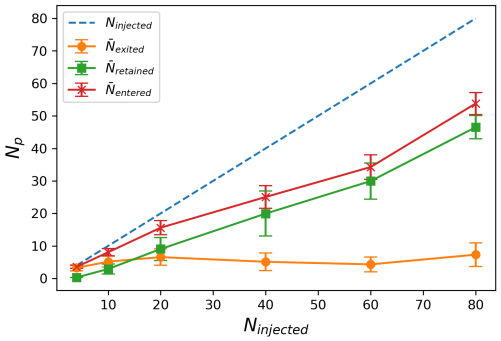

(e) $\alpha = 0.58$

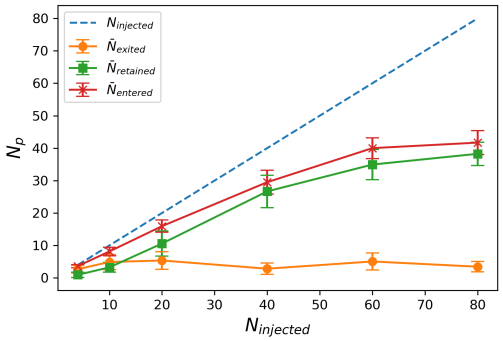

(h) $\alpha = 0.65$

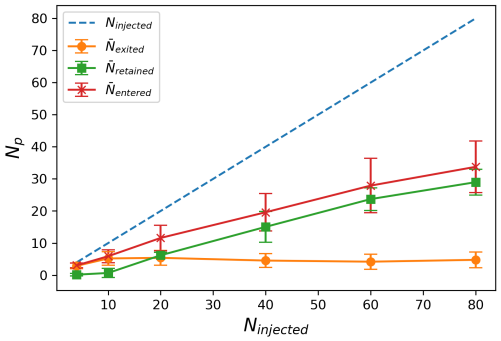

(e) $\alpha = 0.72$

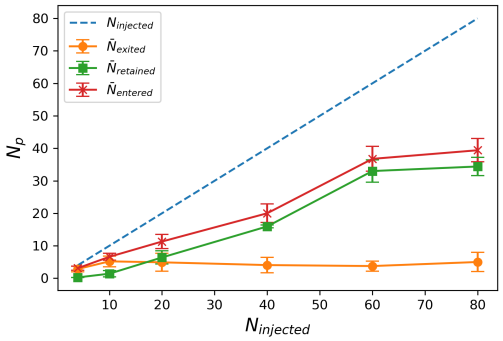

(h) $\alpha = 0.87$

Figure 4.6: Average particle number entered, exited, and retained among 20 tests with different particle numbers injected for different particle size ratios.

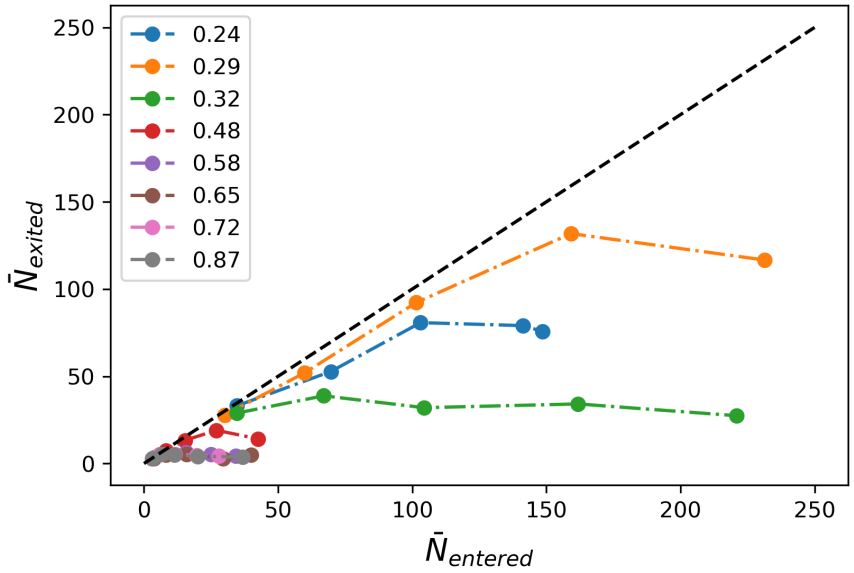

Figure 4.7: The N_{exited} with $N_{entered}$ under each α.

As shown in Fig.4.9, in each subplot, the particle population demonstrates a similar pattern of change as $N_{injected}$ increases. When $N_{injected}$ is smaller than $N^c_{injected}$, the value of Φ does not change significantly with depth and is very close to 1. This implies that the number of particles entering the medium can all pass through each medium region. At $N^c_{injected}$, Φ decreases between pores 1 and 2 and then does not change with depth. This shows that some particles begin to be retained at pore 1 at this point. And the particles that pass through pore 1 can all pass through the medium. As $N_{injected}$ continues to increase, there is a decrease at pores 1, 2, 3, even 4 and 5, which shows that there will be some particles retained inside the medium. And the difference between pore 1 and 2 is larger, showing that the particles are mainly retained at pore 1. Different α corresponds to different $N^c_{injected}$ values, thus leading to differences among subplots. Also, under large $N_{injected}$, an increase in α leads to a smaller Φ, and Φ will mainly decrease at pores 1 and 2. This means that a larger α will block the passage of particles and, at the same time, this will result in a higher amount of retained particles in the upper layers of the medium.

4.5.3 Deposition profile

To further demonstrate the distribution of particle deposition within the medium, Fig.4.10 shows the final distribution of particle deposition with different numbers of injected par-

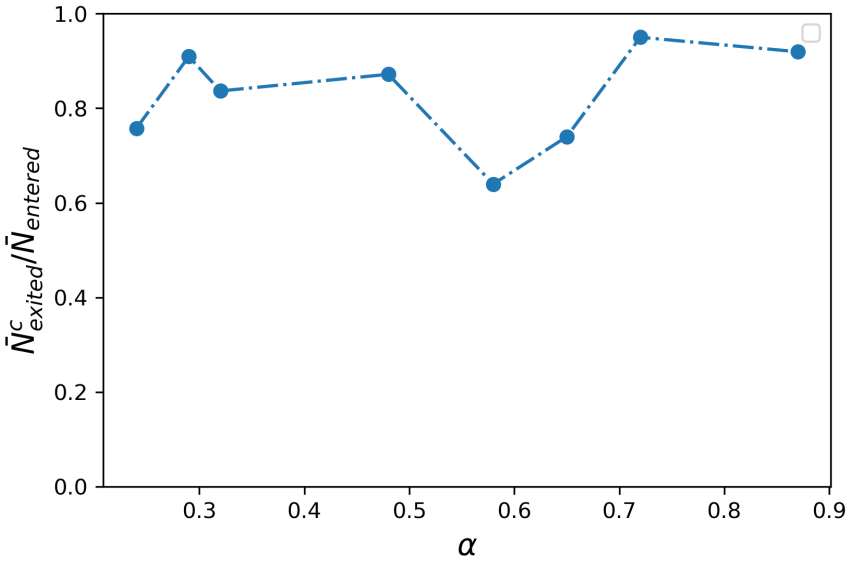

Figure 4.8: The $N^c_{exited}/N_{entered}$ under each α, in which $N_{entered}$ corresponds to that when N_{exited} just arrive at critical value.

ticles in a test at each particle size ratio. First, for each particle size ratio, essentially no particles were retained within the medium when $N_{injected}$ is less than $N^c_{injected}$. As we gradually increase the $N_{injected}$, some particles start to be retained in the A2 region (depth= 10 mm). Continuing to increase the $N_{injected}$, the number of particles retained at A1 and A2 increases, and some particles are retained inside the medium (A4, depth= 20 mm and A6, depth= 30 mm, etc.). For different α, when α is less than 0.48 and $N_{injected}$ is large enough, we can see that the number of deposited particles decreases with depth in the medium. And when α is greater than 0.48, even though $N_{injected}$ is large enough, the particles are mainly concentrated at the A1, A2 region (depth= 0 - 10 mm).

4.6 Observed particle behaviors induced clogging

This section directly shows how the behavior of the particles changes with the variation of $N_{injected}$ and α and ultimately leads to the occurrence of clogging, to further explain the results obtained in the previous sections. First, using $\alpha = 0.48$ as an example, we present how $N_{injected}$ affects the behavior changes of the particles, both at the entrance of the medium (pore 1) and in the interior of the medium (left part from A3 to A6 area as an example). This could demonstrate the accumulation process of particles at the pore

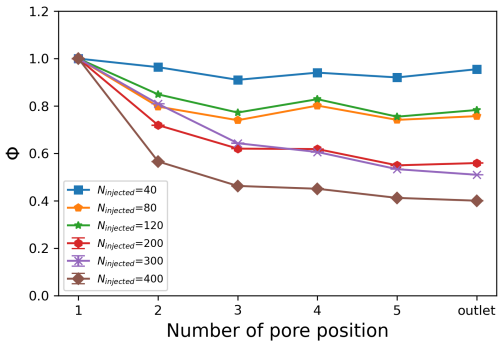

(a) $\alpha = 0.24$

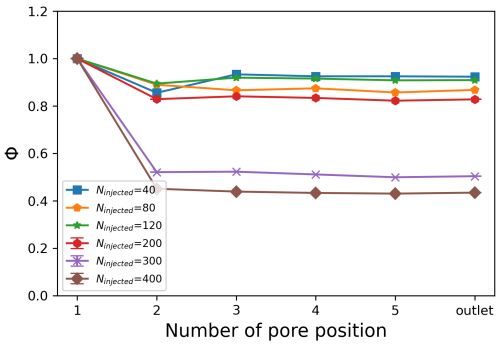

(b) $\alpha = 0.29$

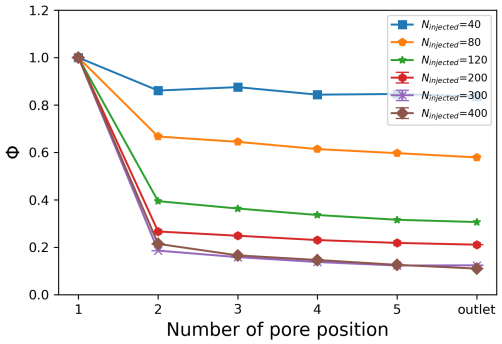

(c) $\alpha = 0.32$

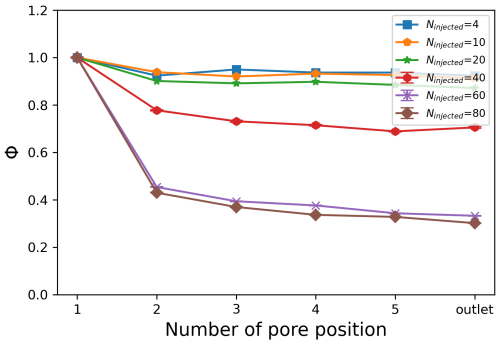

(d) $\alpha = 0.48$

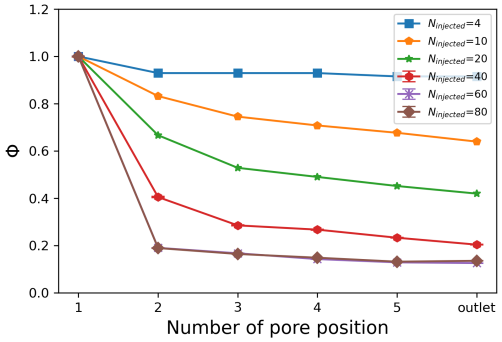

(e) $\alpha = 0.58$

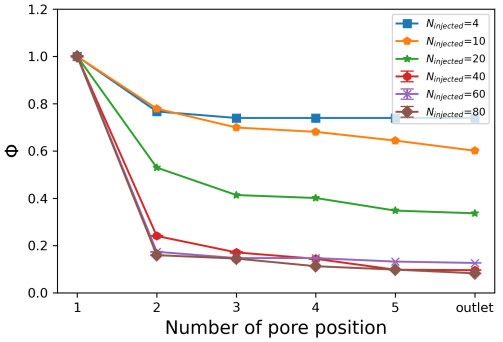

(h) $\alpha = 0.65$

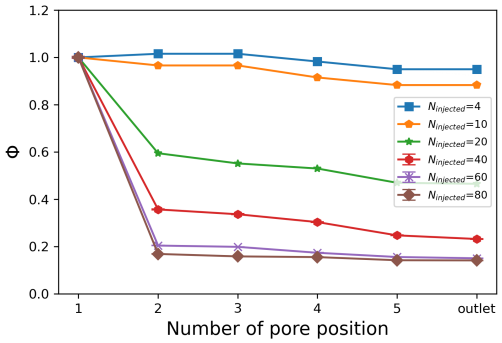

(e) $\alpha = 0.72$

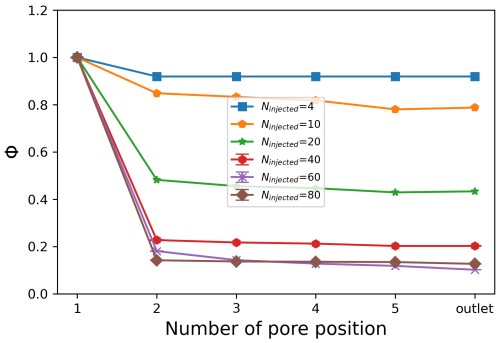

(h) $\alpha = 0.87$

Figure 4.9: Average particle number entered, exited, and retained among 20 tests with different particle numbers injected at each pore area for different particle size ratios.

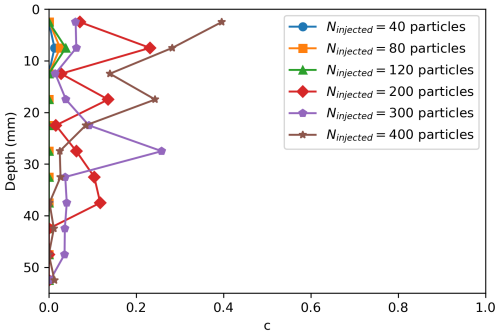

(a) $\alpha = 0.24$

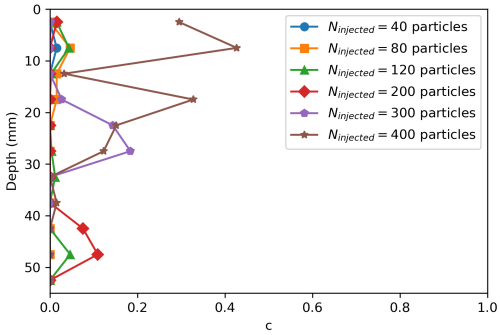

(b) $\alpha = 0.29$

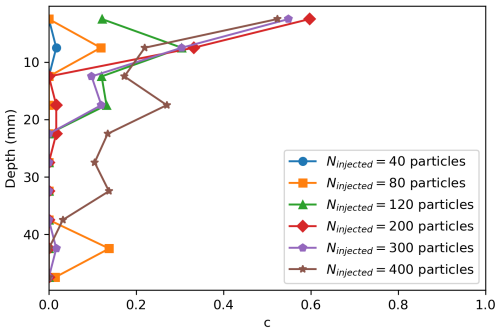

(c) $\alpha = 0.32$

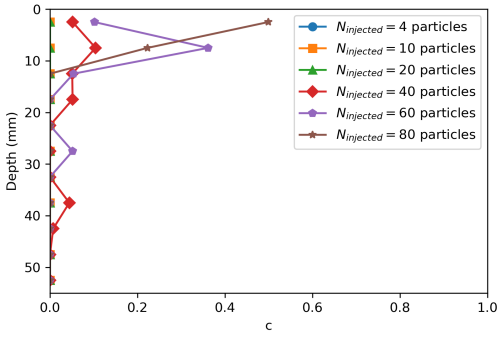

(d) $\alpha = 0.48$

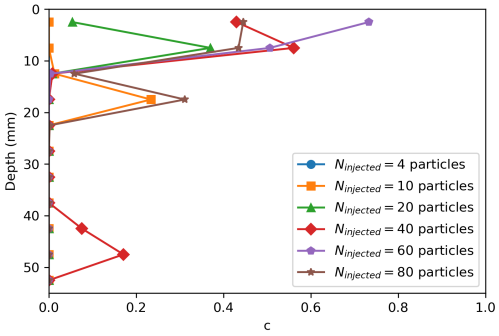

(e) $\alpha = 0.58$

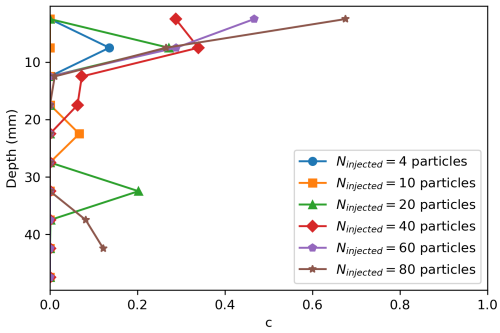

(h) $\alpha = 0.65$

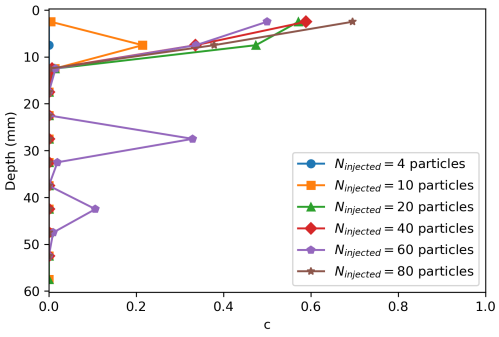

(e) $\alpha = 0.72$

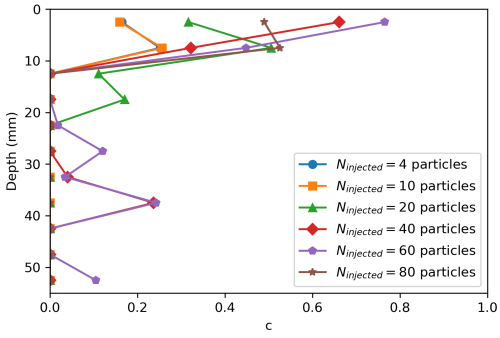

(h) $\alpha = 0.87$

Figure 4.10: Deposition profile for different particle number injected and particle size ratio.

throat. Thereafter, we chose the a2 and a4 areas in Fig.2.14 as examples to quantitatively describe the observed phenomena. Moreover, we also show qualitatively and quantitatively how the behavior of the particles changes for different α. These behaviors primarily involve the inflow and outflow of particles within pore spaces, contact among particles, contact between particles and pillars, and concentration within the pores.

4.6.1 Qualitative description for different $N_{injected}$

At the entrance (pore 1)

Fig.4.11 shows how the behavior of the particles changes and eventually leads to clogging at the medium entrance when the number of injected particles ($N_{injected}$) is gradually increased. When $N_{injected}$ is 4 (Fig.4.11 (1) to (4)), the pushing between the particles causes the particles to be distributed within the width of the inlet. As a result, the particles in the middle will pass after contacting with the bottom pillar. The particles located on both sides will pass along the sides. At the pore throat, due to the geometric blockage between the pillar and the particles, it will be possible for the particles to come into contact with each other (Fig.4.11 (3) and (4)) and then flow out together. When we increase the $N_{injected}$ to 10 ((5) to (8) in Fig.4.11), the pushing between the particles causes the particles to be distributed within a certain range of the x-axis and z-axis. As particles enter the pore space, those in the center are deposited at the upper part of the bottom pillar and accumulate. These deposited particles could further capture the particles near the center, of which the behavior can extend to the two sides (Fig.4.11 (6) to (7)). Due to the low number of injected particles, no subsequent particles enter. Therefore, the deposited particles stop continuing to expand and then slowly flow out of the pore along the bottom pillar (Fig.4.11 (8)). When we increase the $N_{injected}$ to 20 (Fig.4.11 (9) to (12)), this will further enhance the above process. Inside the pore region, the distance between the particles decreases, causing more particles at the center to accumulate on the bottom pillar, while the particles on both sides move towards the pore throat due to the pushing of the center particles, thus passing through the pore area quickly (Fig.4.11 (10) to (12)). As we continue to increase the $N_{injected}$ to 40 ((13) to (16) in Fig.4.11) and 60 ((17) to (20) in Fig.4.11), the above behavior is further enhanced and the inter-particle contact can be extended to the other side of the pore due to sufficient subsequent particles. Thereafter, due to gravity and contact between the particles, the particles will do a stick-slip motion along the bottom subject, and the more the particles are outwardly

located, the relatively larger velocity they have (shear motion of particles, indicated by red arrows and particle color, in Fig.4.11 (15), (19)). In this process, when a stable force chain connection across the pore throat is suddenly established between the particles, particle bridges are formed, which in turn block the pore throat. As we continue to increase the $N_{injected}$ to 80, due to the larger number of particles and smaller particle spacing, the blockage of the particles on both sides induced by the left and right pillars propagates to the center (Fig.4.11 (22)), resulting in small velocities for the particles on both sides and relative larger velocities for the particles in the center, which in turn leads to the possibility of particle bridges formation between the left and right pillars. Since no stable contact is established, the blockage between the particles gradually weakens and begins to accelerate as settling continues (Fig.4.11 (23)). While the particles gradually come into contact with the bottom pillar, the inter-particle contact could spread throughout the area (Fig.4.11 (24)), resulting in particle blockage.

Inside medium

Fig.4.12 shows how the behavior of the particles changes and eventually leads to clogging at the internal pores of the medium when the number of injected particles ($N_{injected}$) is gradually increased. When $N_{injected}$ is 4 ((1) to (4) of Fig.4.12), the number of particles is small, and therefore there is little inter-particle influence. The particles will pass through the internal pores of the medium sequentially. The behavior of the particles is therefore close to the settling of individual particles - the particles oscillate back and forth within a certain range of the x-axis due to the obstruction of the pillars (in the range of two vertical dash lines, main sedimentation channel). When $N_{injected}$ is equal to 10 ((5) to (8) in Fig.4.12), a small accumulation of particles occurs at the entrance and then flows out sequentially. The effect between particles remains small. When we increase the $N_{injected}$ to 20 ((9) to (13) in Fig.4.12), we can see that at the constriction of the entrance (at first row), due to the geometrical obstruction of the particles and the pillars, the particles come into contact with each other and flow out of the pore space together (Fig.4.12 (9) and (10)). As a result, the outflowing particles will have greater inertia (greater velocity) and due to the blockage of the right particles (close to the pillar side), the left particles will settle along the further outboard side and thus be deposited further up the pillar in the next layer (Fig.4.12 (11)). The deposited particles then reduce the size of the pore channel and trap the following particles within the main channel (between dash lines), causing the particles to accumulate at the pore throat. Similarly, due to the accumulation

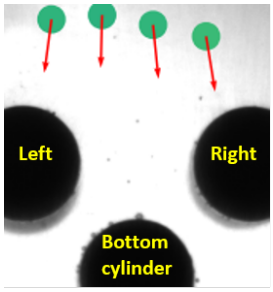

(1)

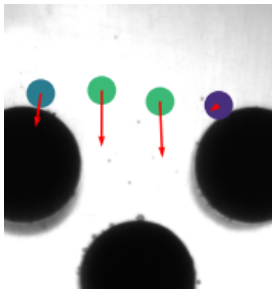

(2)

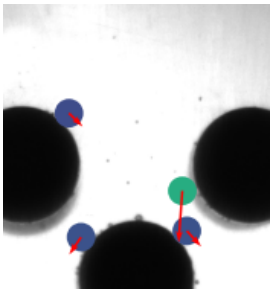

(3)

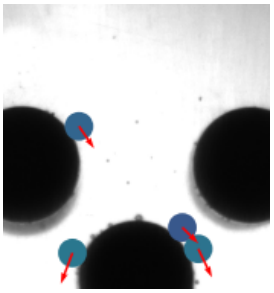

(4)

$N_{injected} = 4$ particles

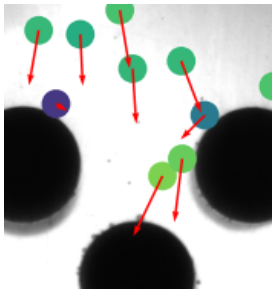

(5)

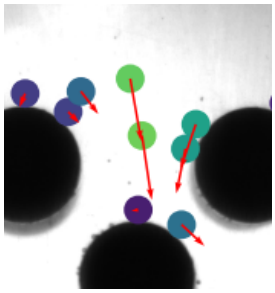

(6)

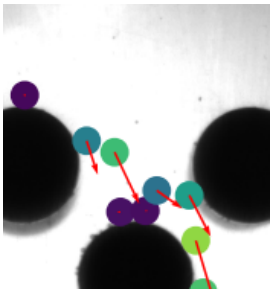

(7)

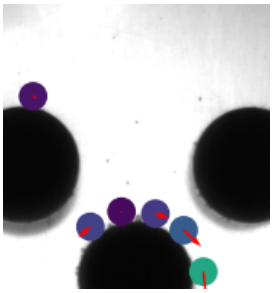

(8)

$N_{injected} = 10$ particles

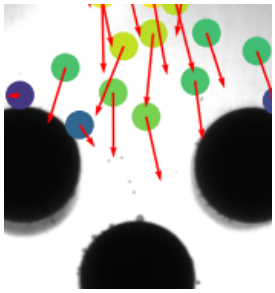

(9)

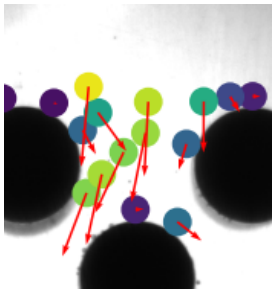

(10)

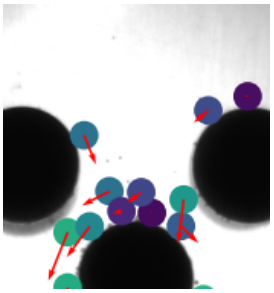

(11)

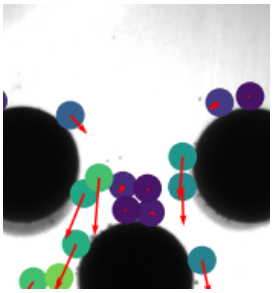

(12)

$N_{injected} = 20$ particles

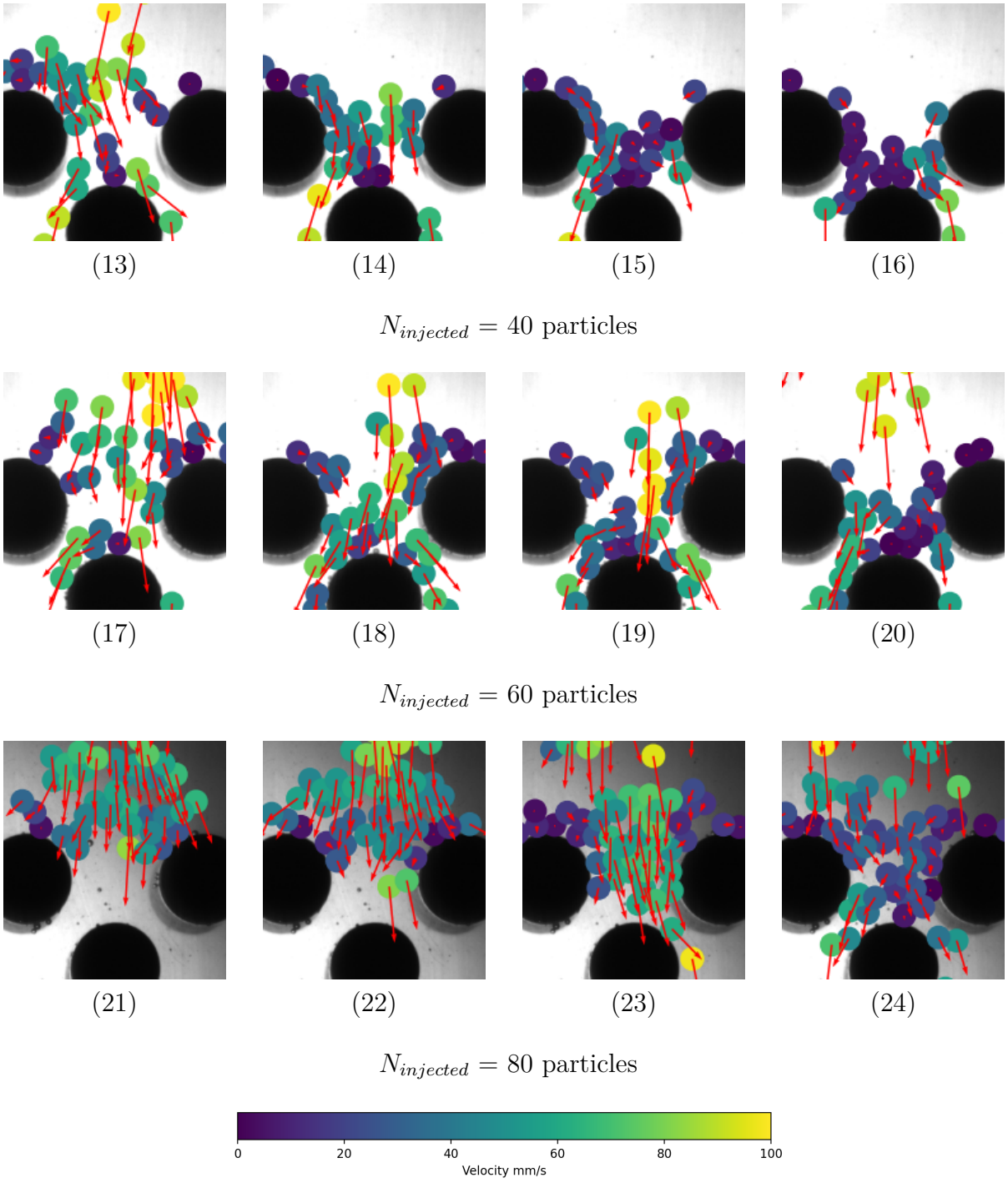

Figure 4.11: Sedimentation process at the entrance for different particle number injected of 2 mm particle and M1; particle colors indicate velocity magnitude; red arrow length and direction show relative velocity and direction.

of particles at the second row of pores, contact and blocking between particles will also cause particles to accumulate at the next row of pore throat. As we increase the $N_{injected}$ to 40, 60, and 80 (Fig.4.12 (13) - (24)), the number of particles entering the interior of the medium increases, and more particles create an accumulation at the interior pores, allowing a chain of forces to build up between the particles across the pore throat, which then creates the potential for clogging. Again, this accumulation behavior of the particles could also lead to accumulation at the next pore.

4.6.2 Quantitative description for different $N_{injected}$

As can be seen from the previous section, the process of particles clogging the entrance and the interior of the porous medium involves changes in particle flow, particle concentration, contact between particles, and contact between particles and pillars. Therefore, this section quantitatively describes the process of clogging under different $N_{injected}$ by analyzing the settling images. The particle flow at the inlet and outlet (q_{in} and q_{out}) are calculated as shown in Eq.2.29. The particle concentration is calculated as shown in Eq.2.30. The contact between particles and between particles and the bottom pillar is calculated by Eq.2.32 and 2.33. To focus on the particle accumulation behavior at the pore throat, we select a2 and a4, the half area of A_2 and A_4 in Fig.2.14.
In Eq.2.29, $N_{entered}^{\Delta t}$ is the particle number entered from t_j to $t_j + \Delta t$ and $q_{in}^{t_j+\frac{\Delta t}{2}}$ shows the particle inflow at time $t_j + \frac{\Delta t}{2}$. Thus, if we fix the Δt from the start to the end - partition the entire settling process into equal periods. We can obtain the variation of the particle flow (q_{in}) over time. The outlet flow of the particles (q_{out}) is calculated in the same way as the inlet flow.
This calculates the histogram of the number of particles entered or exited over time divided by the Δt. Different bin widths and starting points in histogram calculation lead to different results [51]. Therefore, in this study, we employed Kernel Density Estimation (KDE) to generate the frequency distribution graph. In KDE, the bins are centered at each particle position, and for each of them entering at t_i, the value of particle flow (q_{in}) it can generate is:

$$K_H\left(t - t_i\right) = \frac{1}{H\sqrt{2\pi}} e^{-\frac{(t-t_i)^2}{2H^2}} \tag{4.3}$$

$K_H\left(t - t_i\right)$ is using the Gaussian function to continuously divide particle number (equal to 1) into the bin width of 3H (65.26% will concentrate in the range of $t_i - H, t_i + H$),

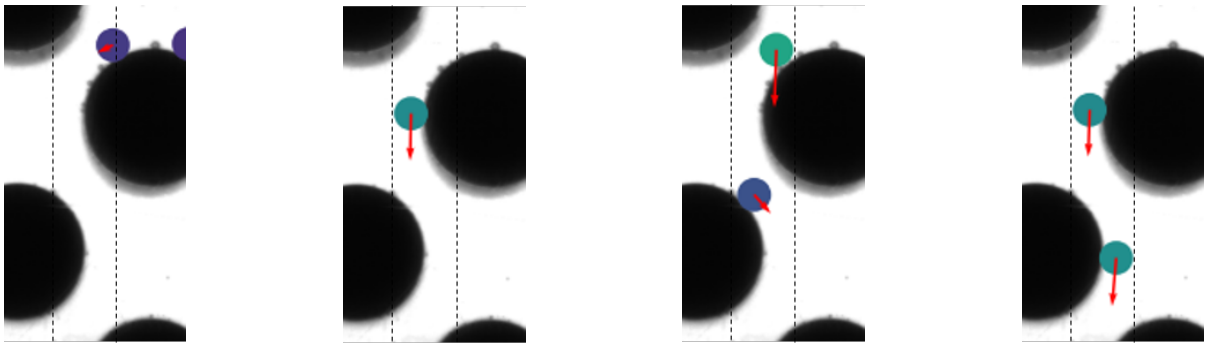

(1) (2) (3) (4)

$N_{injected} = 4$ particles

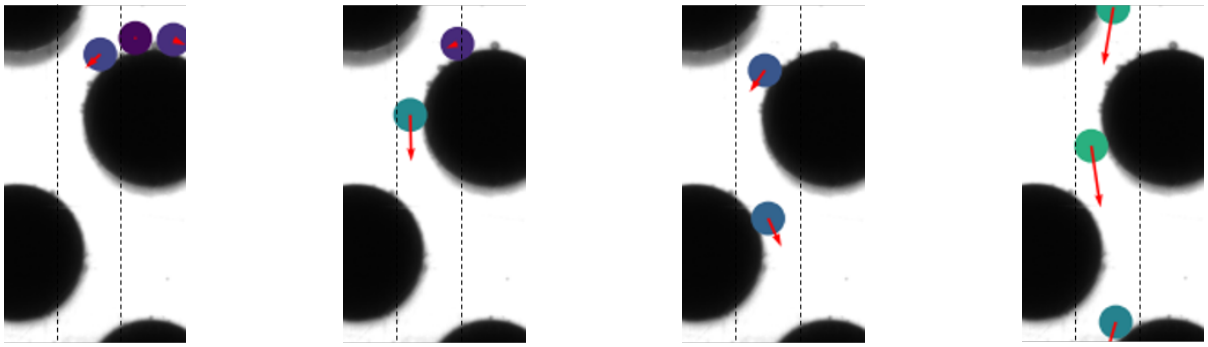

(5) (6) (7) (8)

$N_{injected} = 10$ particles

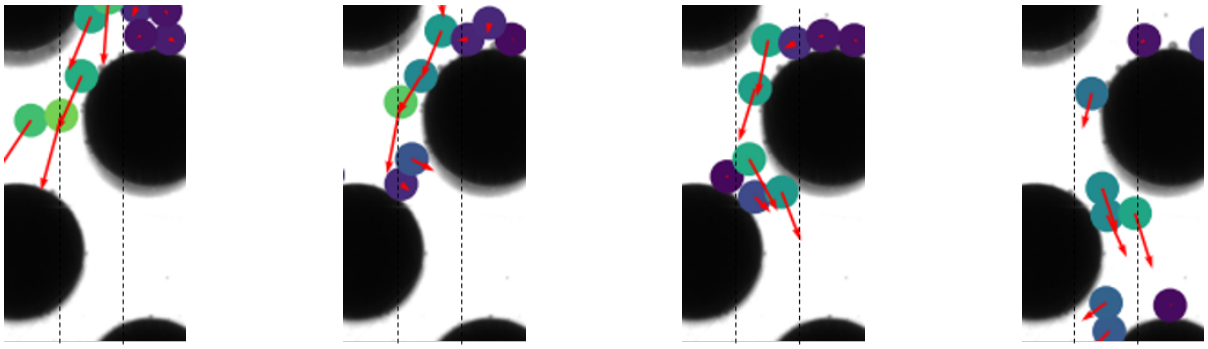

(9) (10) (11) (12)

$N_{injected} = 20$ particles

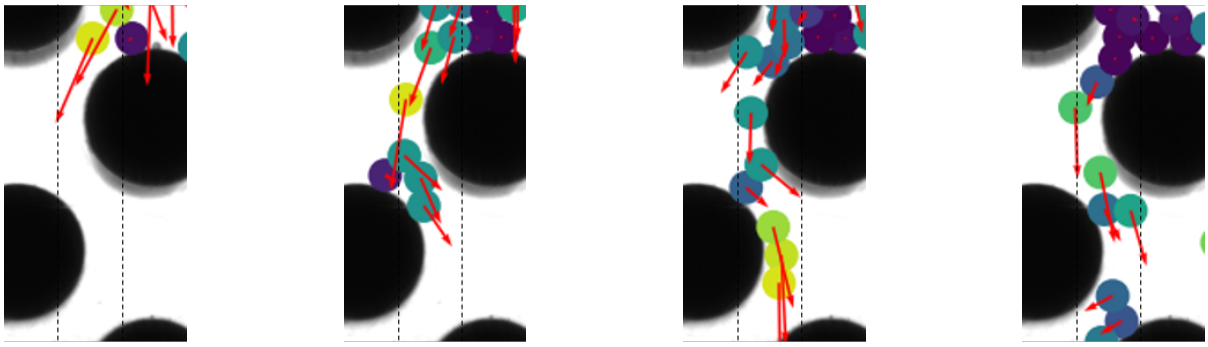

(13) (14) (15) (16)

$N_{injected} = 40$ particles

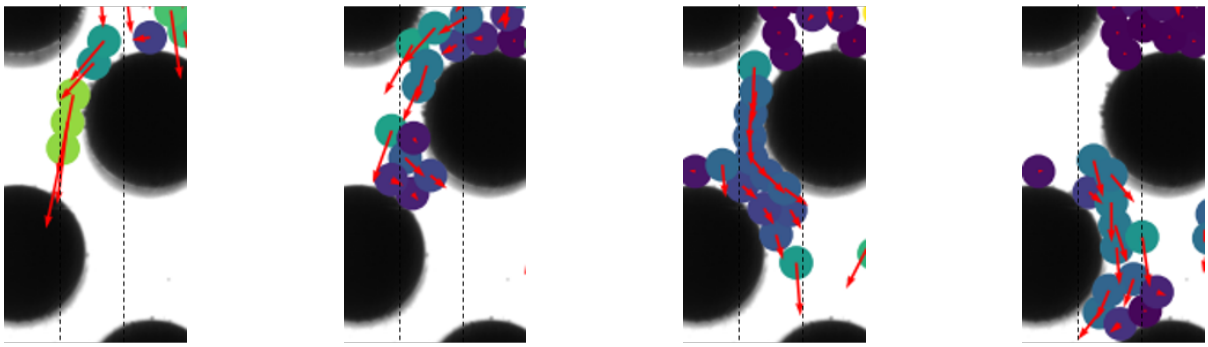

(17) (18) (19) (20)

$N_{injected} = 60$ particles

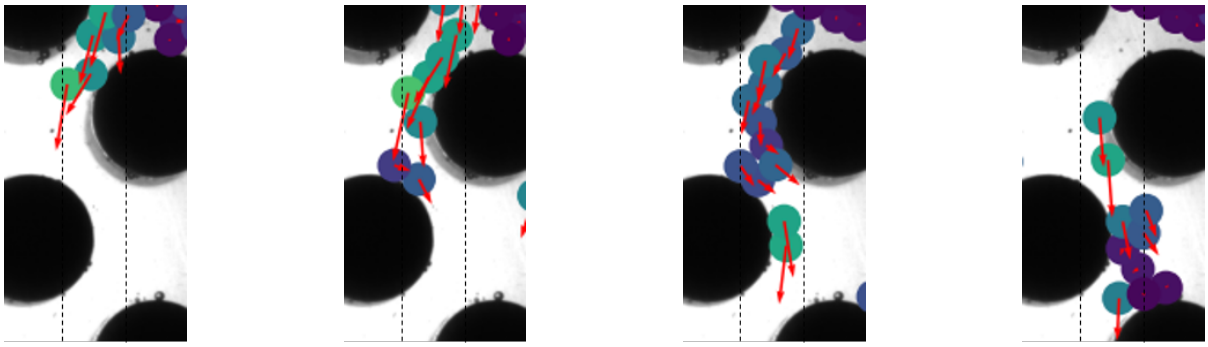

(21) (22) (23) (24)

$N_{injected} = 80$ particles

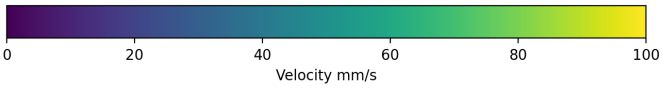

Figure 4.12: Sedimentation process inside of medium for different particle numbers injected of 2 mm particle and M1; particle colors indicate velocity magnitude; red arrow length and direction show relative velocity and direction.

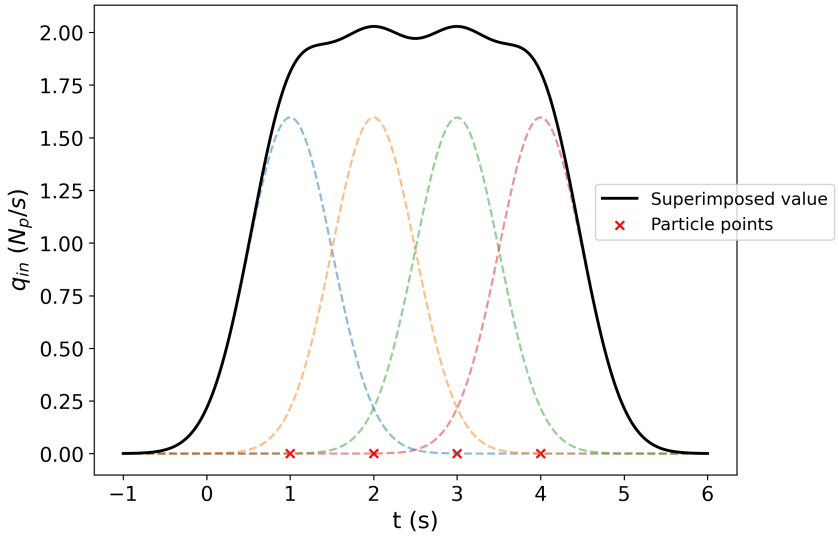

Figure 4.13: Schematic diagram of the KDE calculation. Here, four particles are distributed to enter at t=1, 2, 3, 4 s. Bandwidth (Δt) is 0.5. The dashed line represents the value of the frequency distribution resulting from centering each particle. The solid line represents the result after superposition. $q_{in} = \frac{N_{entered}^{\Delta t}}{\Delta t} = \frac{1}{0.5} = 2$. We can see that the value after superposition is continuously stabilized around 2 during the period of particle entering, so it can better reflect the inflow of particles.

and then:

$$q_{in}\left(t - t_i\right) = \frac{K_H\left(t - t_i\right)}{H} \tag{4.4}$$

The obtained curve of each particle is the dashed line in Fig.4.13. These values are then superimposed to create a continuous frequency distribution graph [52], [53] (the solid line in Fig.4.13). Compared with histogram, the main difference of KDE is to make particle number continuously distributed with t, which could obtain a continuous curve of q_{in}. Besides, this approach effectively eliminates the influence of starting points in the calculation. During the KDE process, we used the Gaussian kernel function and set the bin width (Δt) to 0.15.

At entrance

Fig.4.14 illustrates the particle transportation process at a2 of M1 for different $N_{injected}$, 2 mm particles. By quantitatively describing the particle transportation process, the whole process can be divided into three stages: dispersion state, contact state, and clogging state. The dispersion stage is located at the very beginning of particle transportation. As the

particles continue to flow into the pore space, the particles enter the pore space and flow out orderly, leading to a small value of c. In this stage, the value of CN_p remains small. This shows that the particles within the pores are dispersed within the space. The second phase is the contact phase. The media structure blocks the passage of the particles, leading to an accumulation of particles in the space. As c continues to increase to a certain degree (the distance between particles decreases and blockage among particles increases), CN_p suddenly starts to increase significantly. This shows the process by which the particles would deposit at the bottom pillar and further rapidly trap the rest of the particles in the space. Therefore, the transition between the dispersed and contact states is accompanied by a decrease in q_{out} and a rapid increase in c. This puts the particles in contact with each other. The contact state between the particles allows them to establish force-chain connections across both sides of the pore. And once a stable connection is formed, clogging occurs (clogging stage). At this point, q_{out} decreases rapidly to 0. Continued entry of particles could still change the value of c, but soon it will remain constant.
When the $N_{injected}$ is less than 20, the small q_{in} produces small c, the particles are dispersed within the pore space and little contact is created between the particles. When the $N_{injected}$ is 20, the c in the space can reach around 0.4 induced by the relatively large q_{in}. At this time, the blockage between the particles and the pillar will cause the particles to contact and accumulate at the pore throat, resulting in a shift in the contact state. However, since there are not enough particles to supplement, the accumulated particles gradually flow out of the pore space. Continuing to increase $N_{injected}$ (40-80), a large number of additional particles (q_{in}) enter the space following those that are already in contact. This allows the contact state of the particles in the pore space to be maintained for a longer period (indicated by CN_p with time), and therefore the particles have more opportunities to establish stable connections at the pore throat and form a blockage.

Inside medium

Fig.4.15 illustrates the particle transportation process at a4 of M1 for different $N_{injected}$, 2 mm particles. By comparison with the particle transport process at the entrance, the transport of particles through the internal pores does not have a state transition: from the dispersed state to the contact state. The $N_{injected}$ directly determines whether the particles will pass through the internal pore in a dispersed or in-contact state. When $N_{injected}$ is less than 20, the CN_p and CN_{pc} are almost 0, and no accumulation of particles occurs in the

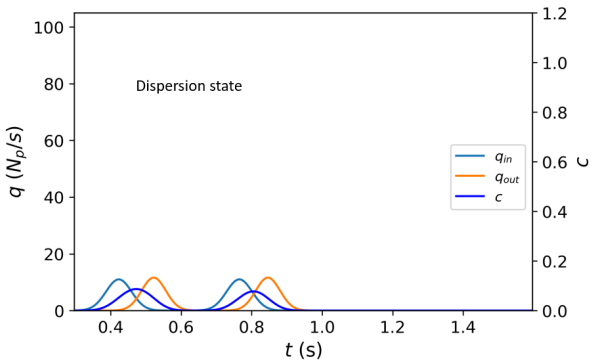

(1)

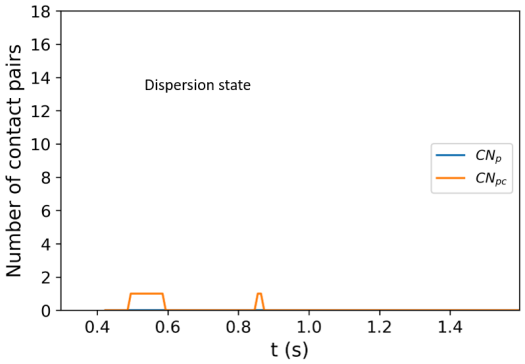

(2)

$N_{injected} = 4$ particles

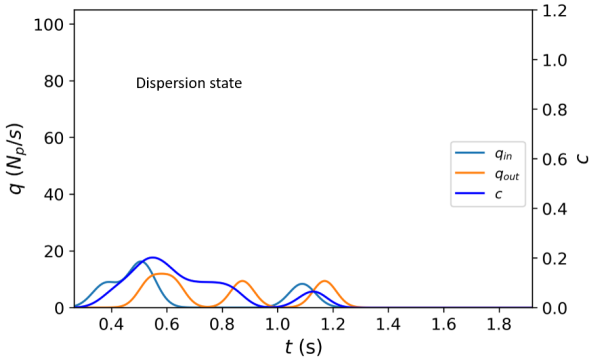

(3)

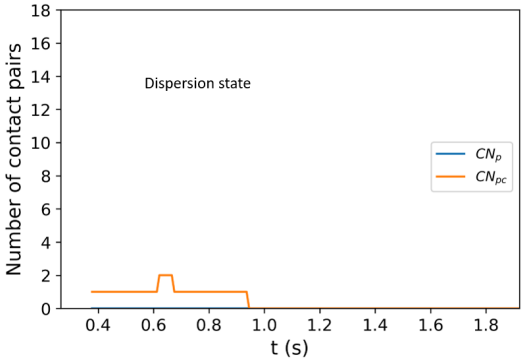

(4)

$N_{injected} = 10$ particles

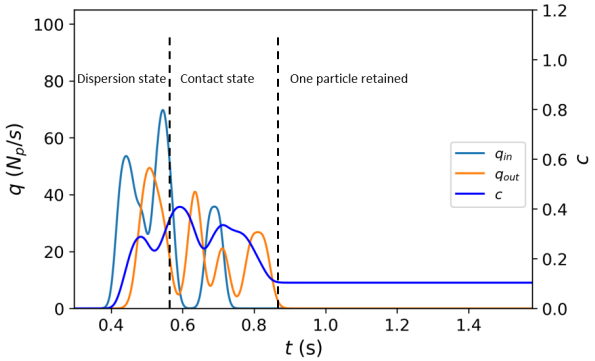

(5)

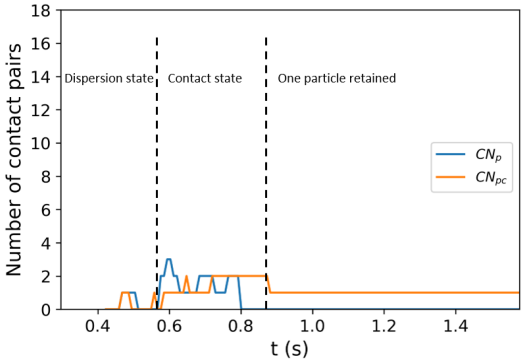

(6)

$N_{injected} = 20$ particles

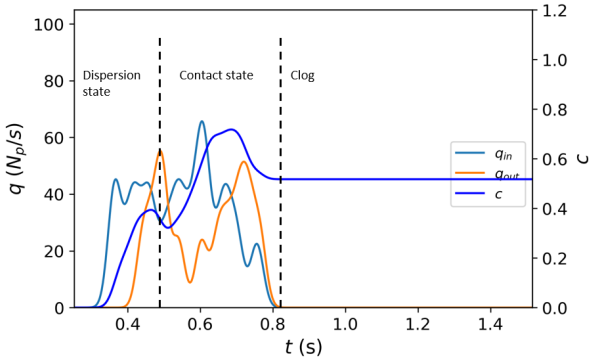

(7)

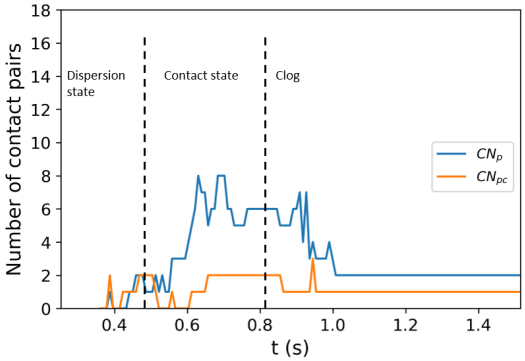

(8)

$N_{injected} = 40$ particles

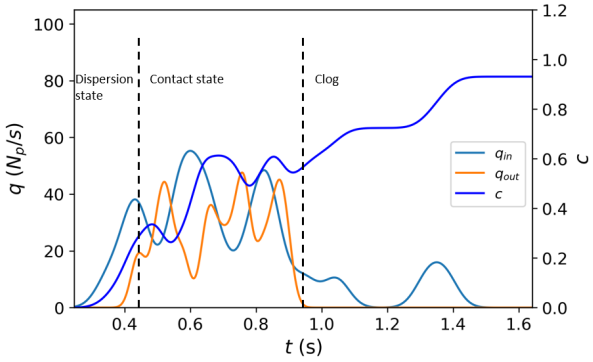

(9)

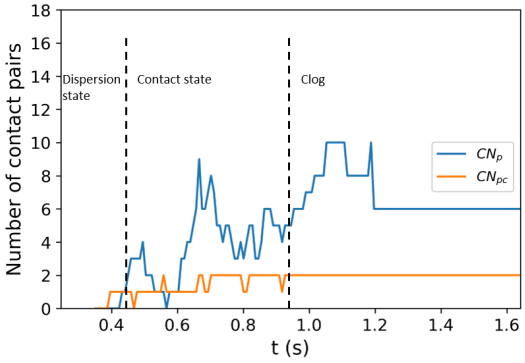

(10)

$N_{injected} = 60$ particles

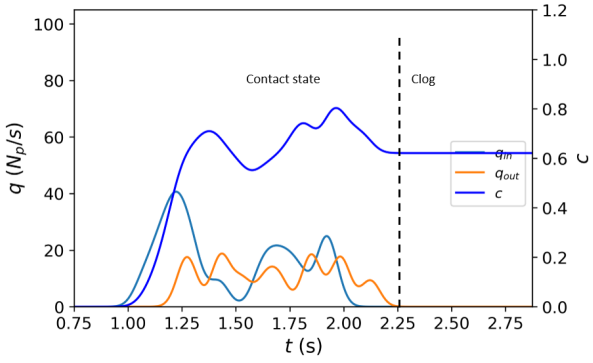

(11)

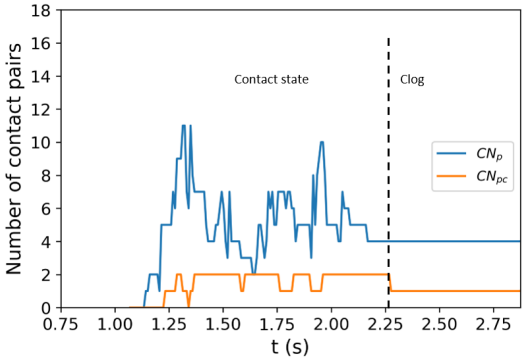

(12)

$N_{injected} = 80$ particles

Figure 4.14: Particle inflow and outflow, concentration, contact number among particles and, between particle and bottom pillar over time for different $N_{injected}$, 2 mm particle at the left entrance of M1.

internal pore. When $N_{injected}$ is 20, the inter-particle blocking and contact at the entrance increases. There is a very small increase in the CN_{pc} which remains for a small period, indicating that particles come into contact with the upper part of the pillar, and then exit the pore along the side of the pillar. When $N_{injected}$ is 40, the previously deposited particles trap the particles in the main channel, leading to a small value of CN_p. At $N_{injected}$=60, the larger q_{in} indicates more particles enter into the a4 area at the same time. This could also show that the blockage among particles is larger at entering and this could cause particles to deposit on the pillar. Then, the deposited particles trap subsequent particles. Thus, CN_p gradually increases to higher values and can be maintained for a longer period. Just like at the entrance, a prolonged state of particle contact leads to a higher probability of clogging. At $N_{injected}$=80, a smaller number of particles enter the interior of the medium due to the rapid formation of clogging at the entrance. However, due to the blocking and contact between the particles, an accumulation can also form at the internal pores.

4.6.3 Qualitative description for different α

As the particle size ratio (α) changes, the geometrical obstruction formed between the medium structure and the particles also changes, which in turn leads to different settling processes. Here we introduce the settling process of $N_{injected}$= 80 and 1 mm, 2 mm, and 3 mm particles in M1 (corresponding to α of 0.24, 0.48, and 0.72 respectively) as an example.

At entrance

As shown in Fig.4.16 (1) - (4), as the 1 mm particles enter the pore space, the particles gradually accumulate in the upper part of the bottom pillar due to the obstruction. Under the action of gravity, the accumulated particles will automatically fill the inter-particle pore space to form a relatively dense particle pile (Fig.4.16 (2) - (3)). At the same time, the accumulated particle pile will gradually expand to the sides of the pore space, which tends to be in contact with the particles that settle on the two sides of the pore space and form the particle bridge at the pore throat. However, at this time, it is difficult to form particle bridges because the d_p and $N_{injected}$ are small. Therefore, the deposited particles flow out simultaneously along the surface of the bottom pillar. When $d_p = 2$ mm (Fig.4.16 (5) - (8)), the geometric blockage formed between the particles and the pillars increases significantly. After the particles enter the pore space and form contact with the bottom

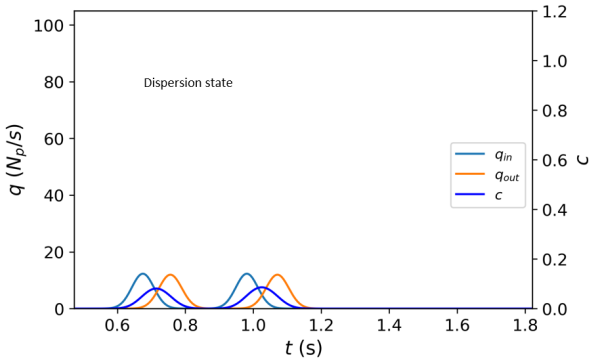

(1)

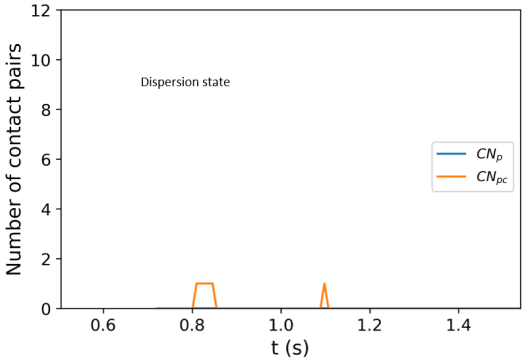

(2)

$N_{injected} = 4$ particles

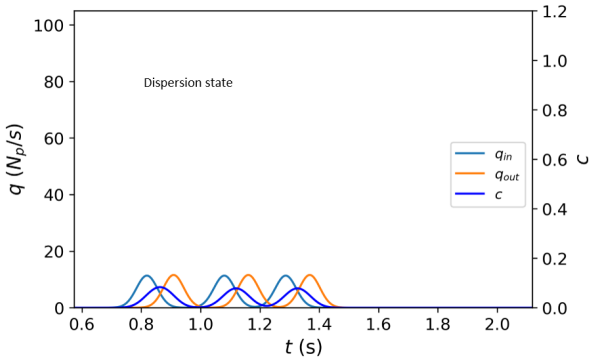

(3)

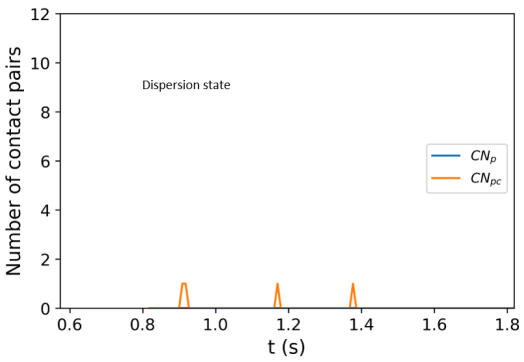

(4)

$N_{injected} = 10$ particles

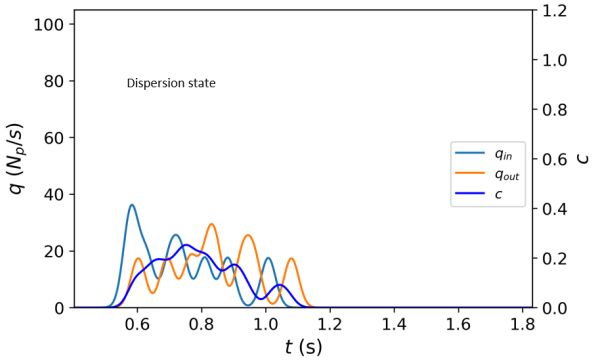

(5)

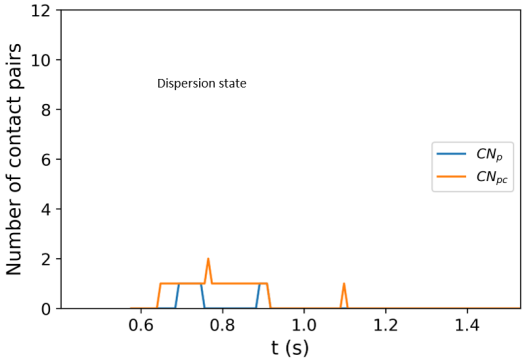

(6)

$N_{injected} = 20$ particles

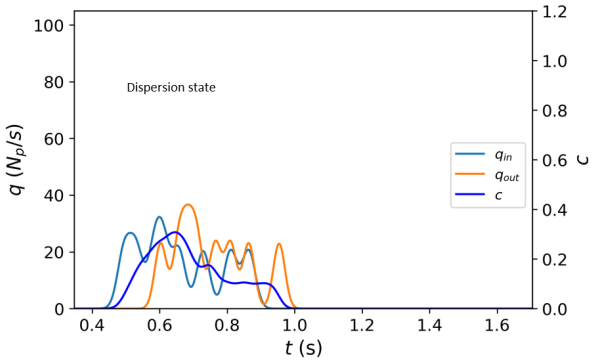

(7)

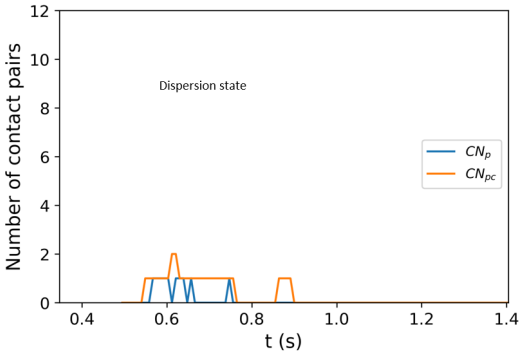

(8)

$N_{injected} = 40$ particles

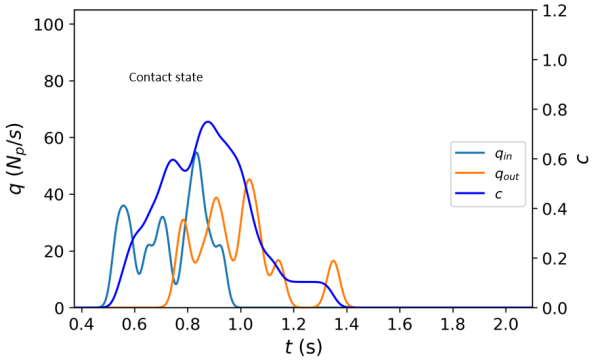

(9)

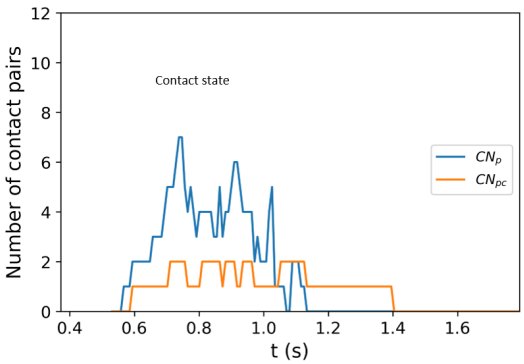

(10)

$N_{injected} = 60$ particles

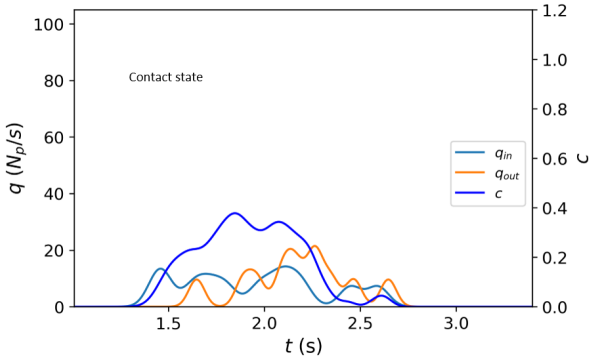

(11)

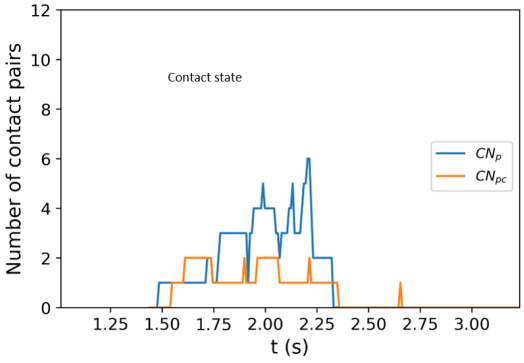

(12)

$N_{injected} = 80$ particles

Figure 4.15: Particle inflow and outflow, concentration, contact number among particles and, between particle and bottom pillar over time for different $N_{injected}$, 2 mm particle inside of M1.

pillar, this causes the contact to spread throughout the space, thus establishing contact across both sides of the pore. Thereafter, the particles are subjected to shear motion under the influence of gravity, with the outer particles having higher velocities, which promotes the formation of particle bridges. When $d_p = 3$ mm, the geometrical blockage between the particles and the pillar increases significantly. In Fig.4.16 (10), the deposition of two particles at the bottom pillar will block the passage of the subsequent particles, and only through the contact between a few particles will make the particles establish connections on both sides of the pore. Again, the particles will undergo a shearing motion and rapidly block the pore space.

Inside medium

Fig.4.17 (1) - (4) shows the settling process of 1 mm particles in the internal pores of the medium after passing through the entrance. In Fig.4.17 (1), a few particles flow out at the same time, and there is less obstruction between the particles, so the particles settle within the vertical dashed lines. And as the particles deposited at the entrance flow out together (in Fig.4.17 (2)), the inter-particle blockage increases significantly. The particles on the left will deposit in the upper part of the next layer of pillars and in turn block the settling of the particles at the main channel (Fig.4.17 (3)), which in turn establishes the possibility of particle contact across the pore throat and the formation of clogged pores. When no stable contact is formed, particles flow into the next pore. As the pillar delays the particles at the bottom, the number of particles flowing out together decreases (Fig.4.17 (4)). So the blockage between particles in the channel decreases and the particles will settle mainly within the channel, which leads to a decrease in accumulation at the next pore layer to some extent. When $d_p = 2$ mm, in Fig.4.17 (5), the smaller number of particles also produces a larger inter-particle blockage, causing the particles to be deposited in the upper part of the next layer of pillars, but there are no fast follow up particles in Fig.4.17 (6), so the two particles do not form an accumulation and flow out in Fig.4.17 (7). A large number of particles flow out at the entrance in Fig.4.17 (6), resulting in the outer particles being deposited in the upper part of the pillars, which in turn come into contact with the particles in the main channel, and then undergoes a shearing motion, creating the possibility of blockage. In the absence of a stable connection, the particles could still settle together. The outer particles are deposited on the upper part of the next layer of pillars and in reversal trap the particles in the main channel, again forming an accumulation at the pore throat (Fig.4.17 (8)). When $d_p = 3$ mm, due to the

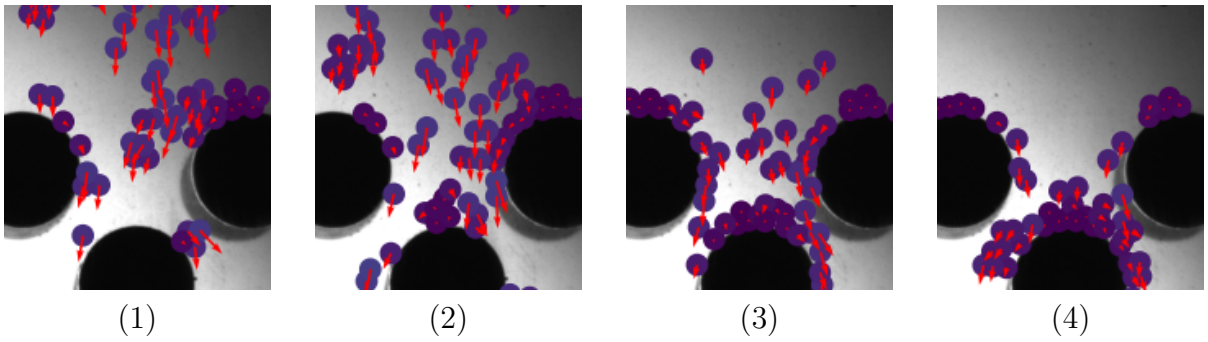

(1) (2) (3) (4)

$N_{injected}$ = 80 particles, d_p = 1 mm, M1

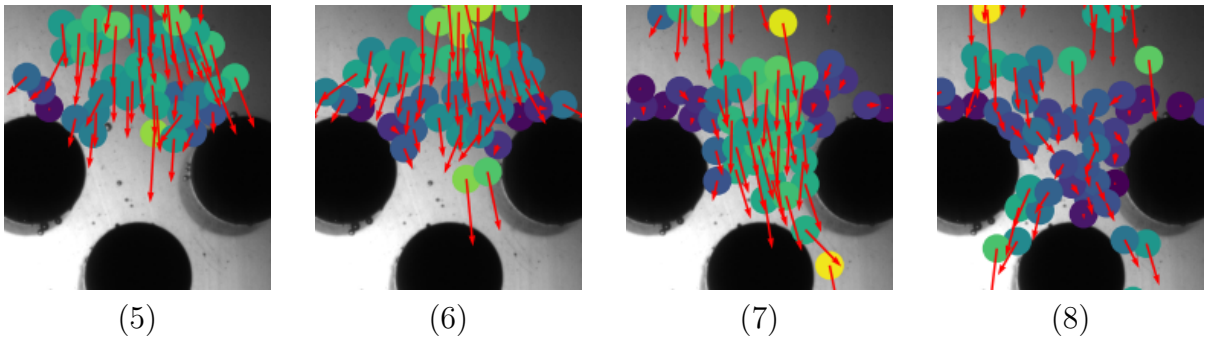

(5) (6) (7) (8)

$N_{injected}$ = 80 particles, d_p = 2 mm, M1

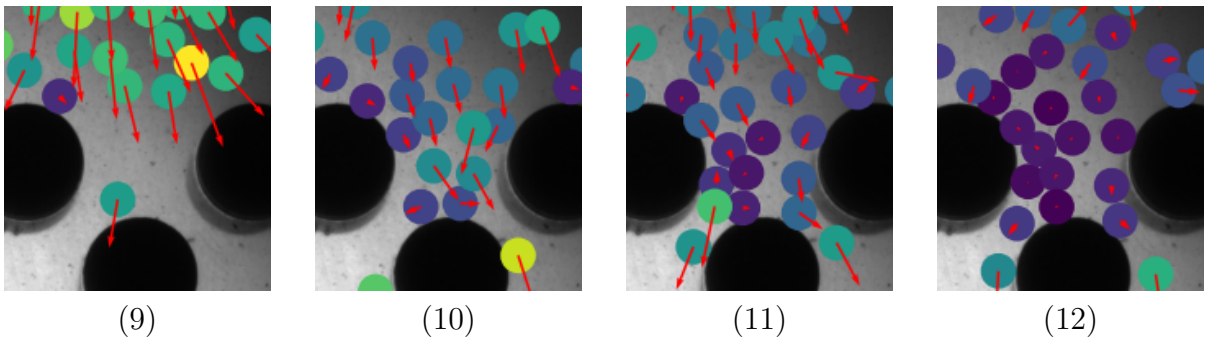

(9) (10) (11) (12)

$N_{injected}$ = 80 particles, d_p = 3 mm, M1

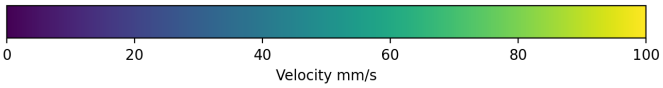

Figure 4.16: Sedimentation process at entrance for different particle diameter with $N_{injected}$ = 80 and M1; particle colors indicate velocity magnitude; red arrow length and direction show relative velocity and direction.

e_p = 4.14 mm, this limits the flow of particles: particles can only flow out one after the other. The short interval between the previous and subsequent particles-i.e., the previous particles have just been deposited at the next layer of pillars, and immediately subsequent particles follow up, only which could create the accumulation of particles, and thus the probability of clogging. Therefore, for smaller α, a large number of particles need to be settled together. The blockage between particles causes the outer particles to be deposited at the pore throat, which in turn leads to accumulation. For larger α, on the other hand, it is mainly due to the blockage by the structure of the medium, which in turn creates the possibility of particle accumulation.

4.6.4 Quantitative description for different α

At entrance

Fig.4.18 shows the settling process for different particle sizes with $N_{injected}$= 80 at a2 area of M1. For 1 mm, in Fig.4.18 (1) and (2), less q_{in} is generated because the settling velocity of the particles is small. With settling, the particles deposit on the bottom pillar and in turn capture more particles, hence CN_p and CN_{pc} gradually increase. The particles accumulate at the pore throat and then flow out together, so q_{out} gradually increases. Eventually, a particle is retained in the upper part of the bottom pillar (check-in video), so both CN_{pc} and c are maintained constant in the end. For 2 mm particle, in Fig.4.18 (3) and (4), a larger q_{in} is produced at the beginning with $N_{injected}$= 80, making c increasing rapidly. Due to the blockage among particles (large c), the CN_p increases quickly at the same time, inducing a contact state among particles. So the q_{out} is relatively small. The contact can be maintained for some time due to enough subsequent particles. The time at which q_{out} equals 0 indicates the formation of a particle bridge at the pore throat. The particles accumulate at the pore space stably and the c, CN_p and CN_{pc} become constant. For 3 mm, in Fig.4.18 (5) and (6), the sedimentation velocity of the particles is larger, but it also induces more blockage between pillars and particles. Therefore, q_{in} is just a little larger than that of 2 mm. Similarly, at 0.65 s the inter-particle converts to a contact state and quickly blocks the pore space. This shows that when we vary the size of the particles, they follow the same behavior at the entrance: accumulation of particles at the pore throat - expansion of the chain of contact forces among the particles - formation of particle bridge.

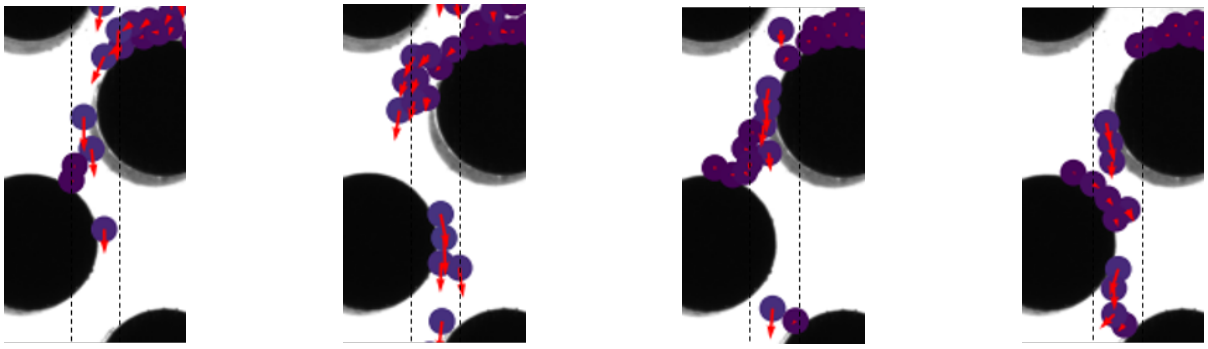

(1) (2) (3) (4)

$N_{injected} = 80$ particles, $d_p = 1$ mm

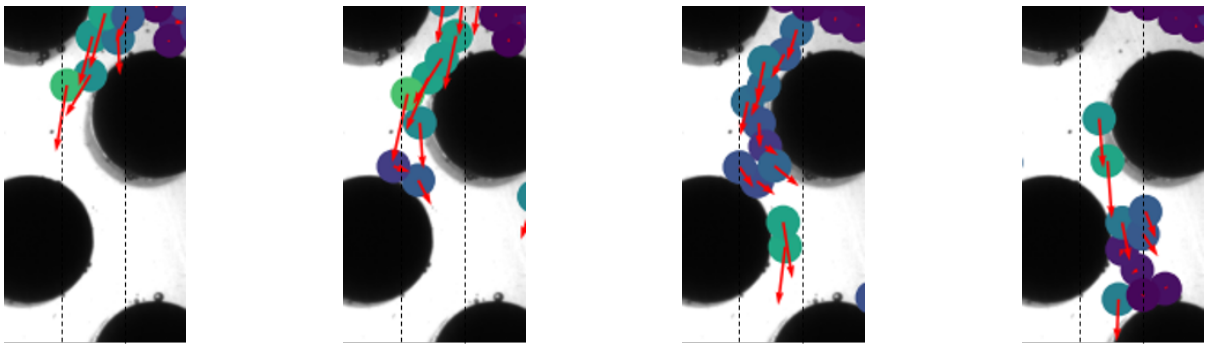

(5) (6) (7) (8)

$N_{injected} = 80$ particles, $d_p = 2$ mm

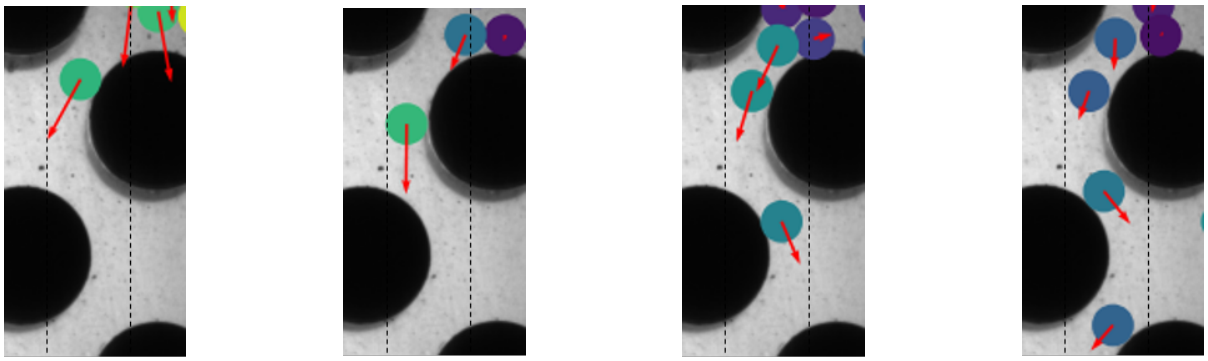

(9) (10) (11) (12)

$N_{injected} = 80$ particles, $d_p = 3$ mm

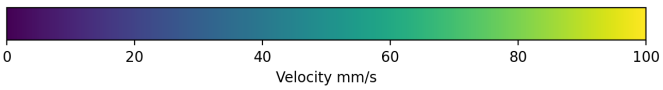

Figure 4.17: Sedimentation process inside of medium for different particle diameter with $N_{injected} = 80$ particles and M1; particle colors indicate velocity magnitude; red arrow length and direction show relative velocity and direction.

However, the different volume sizes of the particles also lead to differences in the settling process. The larger particles have greater settling velocity, which could result in a greater q_{in}, and it also increases the geometric obstruction between the particles and the pillars, resulting in a smaller q_{out} and larger residence time. Thus, the difference between q_{in} and q_{out} becomes large and the increasing rate of the concentration within the pore space is faster with increasing particle size. Both geometrical and kinematic contributions for large d_p make clogging more likely to occur.

Inside medium

Fig.4.19 illustrates the settling process at the a4 area of M1 when 80 particles of different sizes are injected. For 1 mm particles, in Fig.4.19 (1) and (2), at first, the smaller q_{in} produced only small CN_p and CN_{pc}. At around 5.5 s, the larger q_{in} produced larger CN_p and CN_{pc}, showing some particles accumulate at the pore throat. After, the particles flow out gradually, thus, the CN_p and CN_{pc} decrease slowly to 0. For 2 mm particles, in Fig.4.19 (3) and (4), the larger q_{in} make them accumulate directly, the c, CN_p and CN_{pc} increase at the same time. Because there is no stable connection across the pore throat, the particles flow out together at around 2.3 s, corresponding to a high value of q_{out}, which could make particles accumulate at the next pore throat. Then, all parameters become 0 quickly. For 3 mm particles, in Fig.4.19 (5) and (6), since the size of the pore throat at the inlet (e_p=4.14mm) is close to the diameter of the particles, this results in the particles flowing into the medium one by one, resulting the wave curve of q_{in} and q_{out}. When the particles enter into contact with the pillar and until after the particles flow out of the a4 area, the value of CN_{pc} will remain at 1. Due to the smaller q_{in}, the particles did not produce accumulation. In general, the blockage among particles and enough subsequent particles are needed to produce accumulation at the internal pore throat, which requires a large and continuous q_{in} from the entrance. Different particle sizes will have different interactions with pillars at the entrance, and further determine the q_{in} towards the inside pore, which will further influence the clogging occurrence inside.

4.7 Clogging probability

We repeated the experiment 20 times for each of $N_{injected}$ and α and the occurrence of clogging over 20 tests has been statistically analyzed to show the probability of clogging in different medium regions. Fig.4.20 shows the probability of clogging occurrence over

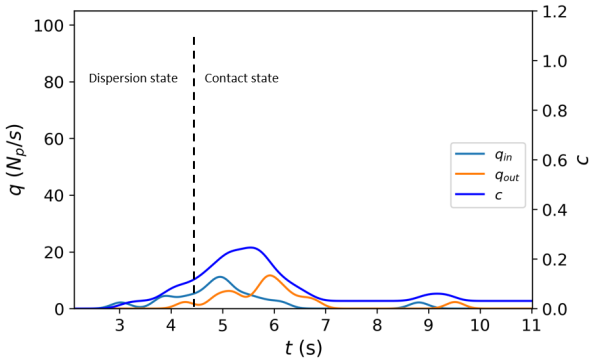

(1)

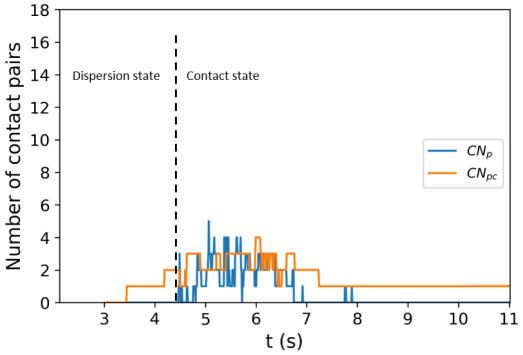

(2)

$N_{injected} = 80$ particles, $d_p = 1$ mm, entrance of M1

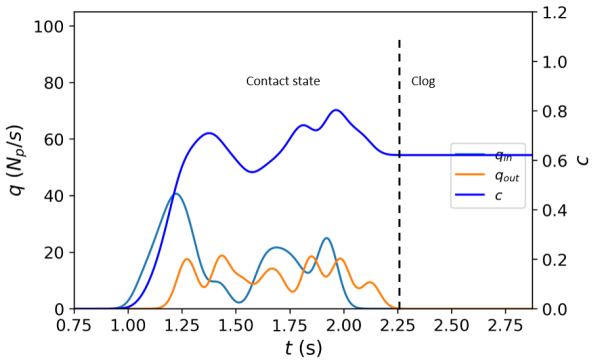

(3)

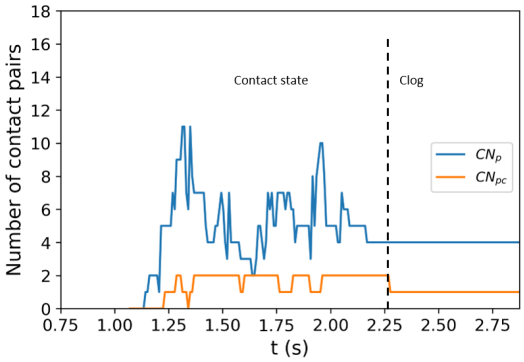

(4)

$N_{injected} = 80$ particles, $d_p = 2$ mm, entrance of M1

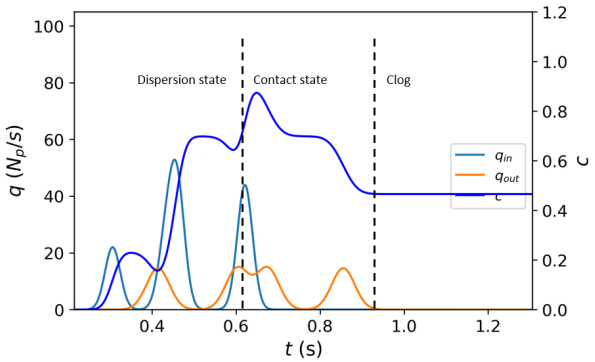

(5)

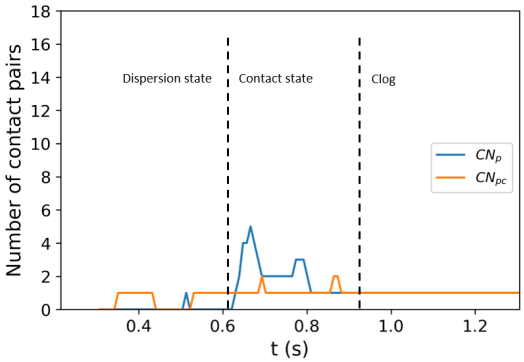

(6)

$N_{injected} = 80$ particles, $d_p = 3$ mm, entrance of M1

Figure 4.18: Particle inflow and outflow, concentration, contact number among particles and, between particle and bottom pillar over time for different particle size at the left entrance of M1.

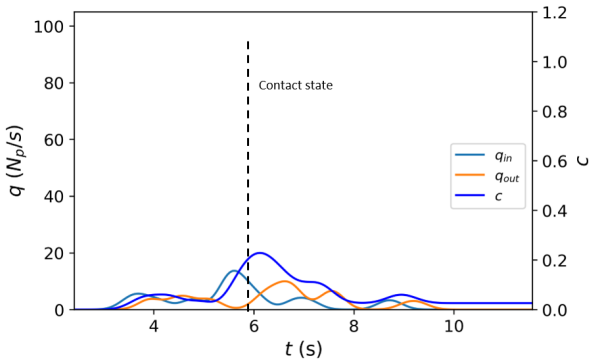

(1)

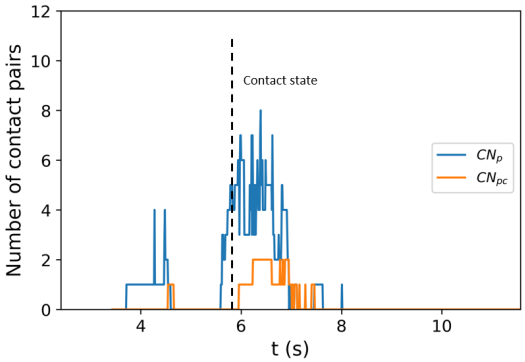

(2)

$N_{injected} = 80$ particles, $d_p = 1$ mm, inside of M1

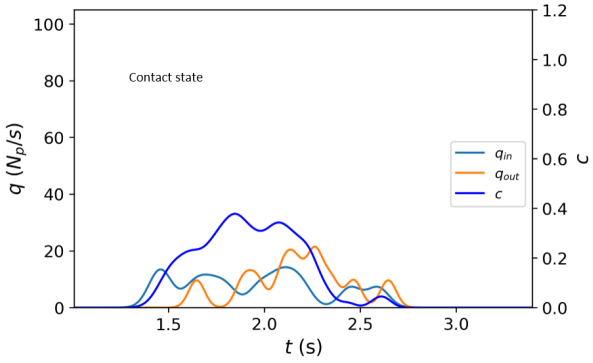

(3)

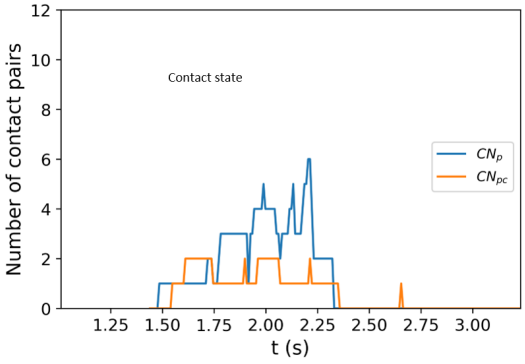

(4)

$N_{injected} = 80$ particles, $d_p = 2$ mm, inside of M1

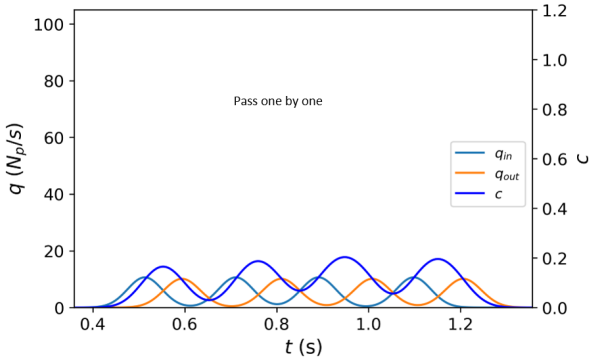

(5)

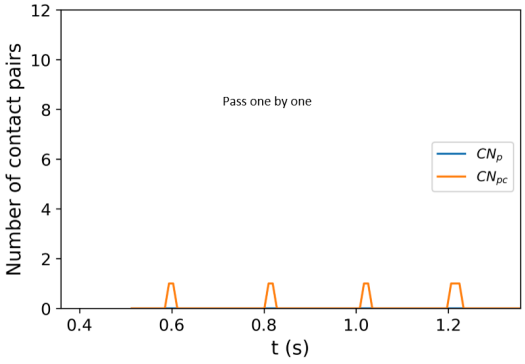

(6)

$N_{injected} = 80$ particles, $d_p = 3$ mm, inside of M1

Figure 4.19: Particle inflow and outflow, concentration, contact number among particles and, between particle and bottom pillar over time for different particle size inside of M1.

the whole media region. It can be seen that for each α, P_m increases with $N_{injected}$. After $N_{injected}$ exceeds the threshold value $N^c_{injected}$, the value of P_m increases rapidly to 1. For different α, the increasing rate of P_m decreases as α decreases. Thus, it requires a larger $N_{injected}$ to bring P_m to 1 for a small α. This shows that an increase in $N_{injected}$ increases the probability of clogging in the media region, and when a threshold value is exceeded, 100% clogging can occur. α mainly changes the rate of increase of P_m with $N_{injected}$. This is mainly because α changes the geometrical blocking between the particles and the pillars. The solid lines in Fig.4.20 are the fitted curves based on the model proposed by Gella et al [18], as shown in Eq.1.15. In the previous section, it has been directly showed that increasing $N_{injected}$ would make particles accumulate at the pore throat, and the velocity of particle flowing out (v_o) decreases with $N_{injected}$, such as in Fig.4.11. Therefore, we used the following equation to fit the data:

$$P_m = (a + b\frac{1}{N_{injected}})^{-(e_p/d_p)^2} \tag{4.5}$$

The fitting results show that the model can predict the blockage probability better.
Fig.4.21 shows the probability of occurrence of clogging in each pore region over 20 tests at different $N_{injected}$ and α. For each α, P_p shows an similar trend with different $N_{injected}$. We take $\alpha = 0.48$ as an example. When $N_{injected}$ is less than 40, the P_p in pore 1-5 is close to 0. And when $N_{injected}$ is equal to 40, the value of P_p increases at all pore 1-5, especially at pore 1, and P_p decreases with increasing pore depth. When continuing to increase $N_{injected}$, this trend is strengthened: the values of P_p at pore 1-5 increase significantly compared with smaller $N_{injected}$; the value of P_p at pore 1 is 1 and reaches the maximum value, it will decrease with depth and the decreasing trend become small gradually. This shows that when $N_{injected}$ is greater than $N^c_{injected}$, it could produce 100% of the pores are clogged at pore 1, while there is also a relatively higher probability of clogging at pores 2-5, but much less than that at pore 1. This is because at larger $N_{injected}$, the q_{in} into the interior of the medium is larger, and the pushing between the particles allows the particles to produce an accumulation at the internal pores, and therefore also produces a larger probability of clogging in the interior. At the same time, due to the spatial distribution of the pores, the particles will accumulate in the upper part more first, so the probability of clogging will decrease with depth.
α also affects the probability of clogging. First, α changes the value of $N^c_{injected}$: the larger α is, the smaller $N^c_{injected}$ is required to bring pore 1 to 100% clogging. Second, as α

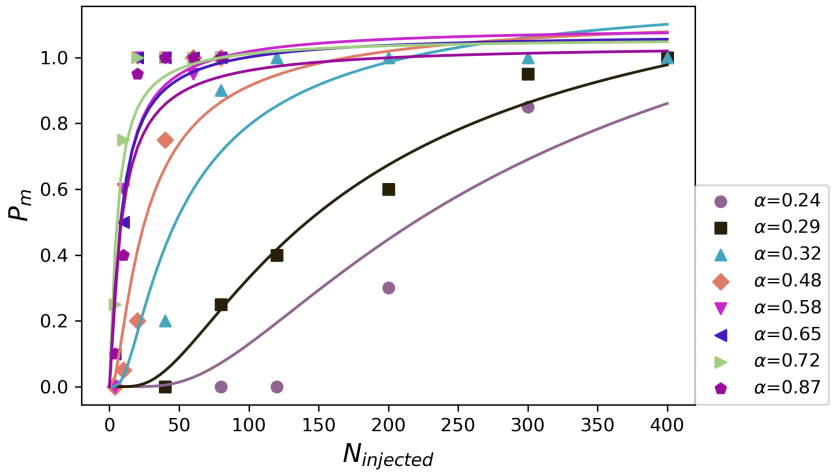

Figure 4.20: Clogging probability at medium for different particle numbers injected under each particle size ratio.

increases, the geometrical blockage in the upper part of the medium increases, this makes clogging easier, so P_p will become more concentrated in the upper part of the medium. At $\alpha = 0.72$ and 0.87 (3 mm particles), the media blockage to particles increases significantly. Sufficient $N_{injected}$ causes a continuous flow of particles into the interior of the media, and an even lesser accumulation of particles could lead to the occurrence of clogging. Thus after $N^c_{injected}$, a larger P_p can still be produced at pores 2-5.

4.8 Conclusion

Through the above studies, we have revealed in detail the motion characteristics of several particles in different media. Due to the blockage of pillar media, the particle population will be distributed in a certain range for settling. At the same time, when $N_{injected}$ is sufficiently high, the particles will accumulate at the pore constriction and the accumulation of particles is reduced after passing through the constriction. This behavior will be repeated continuously with the depth direction. When α is large, it restricts the entry of particles into the medium, thereby reducing the accumulation of particles within the medium. For the resulting delay, the smaller accumulation promotes the passage of particles through each region of the medium, reducing their average travel time. When $N_{injected}$ exceeds a critical value ($N^c_{injected}$), the travel time at the entrance does not decrease, and the travel time inside the medium increases, showing a tendency toward clogging. Different α

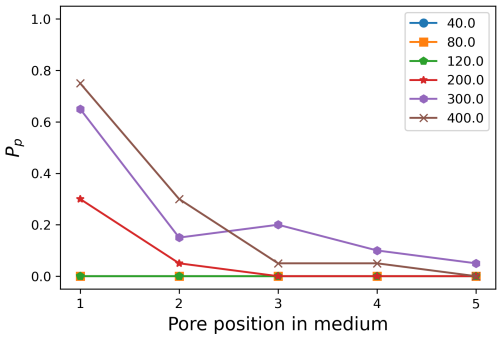

(a) $\alpha = 0.24$

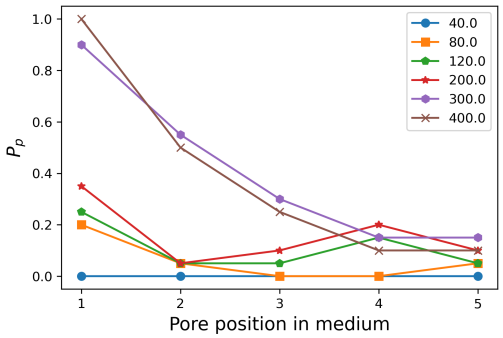

(b) $\alpha = 0.29$

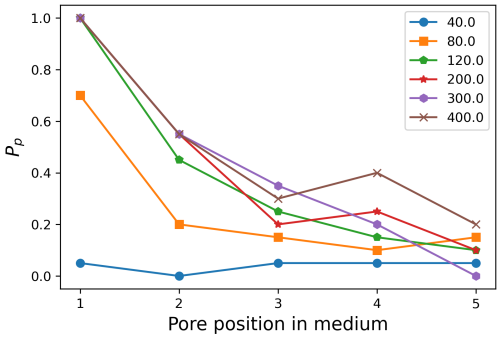

(c) $\alpha = 0.32$

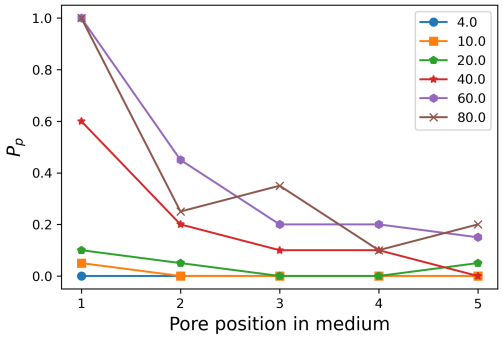

(d) $\alpha = 0.48$

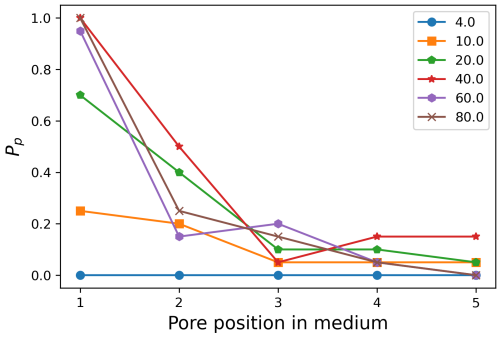

(e) $\alpha = 0.58$

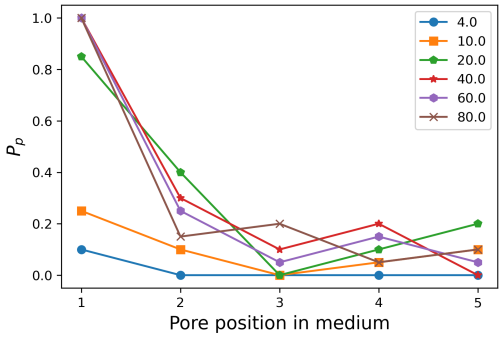

(h) $\alpha = 0.65$

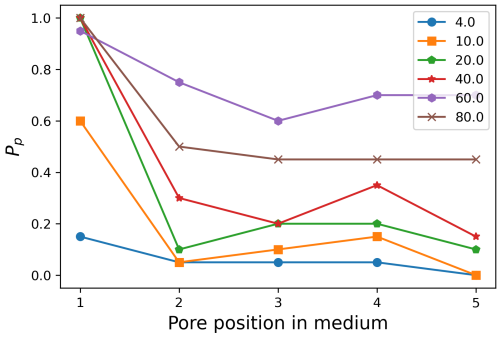

(e) $\alpha = 0.72$

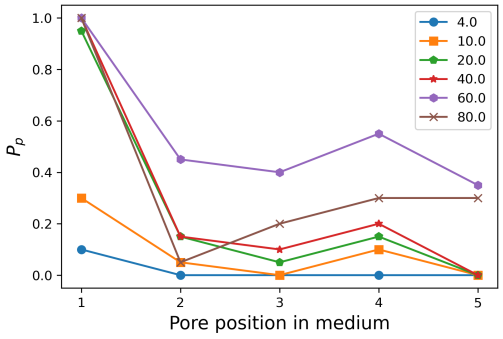

(h) $\alpha = 0.87$

Figure 4.21: Clogging probability at each pore layer for different particle numbers injected and particle size ratio.

corresponds to different $N^c_{injected}$ values, thus leading to varied trends in travel time with changes in $N_{injected}$ under each α. In addition, due to the change in particle size and media structure, we find a similar pattern as in the previous chapter: for the same $N_{injected}$, both larger particle sizes (d_p) and smaller pore sizes (e_p) lead to larger delays, and the effects of both are comparable.

For the particle number involved, we found $N_{retained}$ will start to increase around 0 at $N^c_{injected}$, showing that particles begin to be retained at this point. Also, N_{exited} will not increase significantly after $N^c_{injected}$, showing a critical value existed. By the deposition profiles, we found that the number of clogged particles was mainly retained in the upper areas of the media, especially at the entrance. Larger α (larger particles and smaller pore size) leads to more deposited particles concentrated towards the entrance.

Further demonstration of the particle behavior within the pore space directly gives the reason for the particles clogging different regions of the medium. At the entrance of the medium, the blockage by the pillars causes the particles to deposit on the pillar and further block the particles within the pore space. When there is a sufficient number of particles and due to contact between the particles, this will cause the accumulated particles to extend to the other side of the pore throat, which in turn leads to the possibility of clogging. For the interior of the media, the blockage between particles within the settling channel causes the particles on the outside to deposit on the pillars. This further blocks the passage of subsequent particles at the main settling channel, thus leading to the accumulation of particles in the internal pores and the formation of clogs. For different α, when the particles are larger or the pores are smaller, this increases the blockage between the particles and the pillar, and therefore the particles are more likely to form a blockage at the entrance. At the same time, this will limit the number of particles flowing into the interior of the medium, leading to a decrease in blockage between the particles at the main settling channel. At this point, the accumulation of particles at the internal pores is mainly due to the blockage by the pillar.

The quantitative analysis of the above-mentioned clogging behavior can further reflect the effect of different parameters better. A large particle inflow (q_{in}) means that many particles enter at the same time, which also shows that there will be blockage between the particles, and therefore the particle population will be more likely to accumulate at the pore throat. When the concentration (c) at the pore space is around 0.45 ± 0.05 (random particle packing density) [19], the contact pairs between the particles increases rapidly, indicating the accumulated particles expand to the other side of the pore throat. At this

point, the particle outflow (q_{out}) decreases, showing a greater tendency to clog [18]. For $N_{injected}$, q_{in} will increase with $N_{injected}$, which in turn affects the accumulation and clogging of particles at the pore throat (both at the media entrance and at the internal pores). For α, larger particles have faster-settling velocities and also increase the blockage by the pillar, which produces a larger q_{in} and smaller q_{out}; and the smaller pore size also restricts the outflow of particles. As a result, larger values of α increase the difference between q_{in} and q_{out}, making it easier for c to rise, thereby facilitating the formation of clog. Along the direction of media depth, the q_{out} at the previous pore will determine the q_{in} at the next pore, which in turn affects the accumulation of particles at the next layer of pores. Directly counting the clogging probability over 20 tests is consistent with the clogging trend described above. The clogging probability increases with $N_{injected}$, and especially starts to increase significantly at $N^c_{injected}$. When α is small, the clogging probability increases more quickly with $N_{injected}$ to 1. This can be well fitted by the model proposed by Gella et al. [18]. Along the direction of media depth, particles will first accumulate in the upper part of the media and thus will tend to form clogs in the upper part of the media. Therefore, when $N_{injected}$ is large enough, the clogging probability decreases rapidly with increasing depth. For larger α, it will limit the q_{in} flowing into the interior of the medium, so the clogging probability is more concentrated towards the upper part of the medium. Overall, with this study, we give details of how $N_{injected}$ as well as α affect the mechanism of forming clogs in the media region. This has important implications for our further understanding of clogging phenomena on large scales.

CONCLUSION AND PERSPECTIVES

In the visualization study, we first analyzed the motion of individual particles in a confined medium made of two parallel plates and a porous medium made of staggered pillar assembly. We found that as the gap (G) of the confined medium decreases, this significantly reduces the final settling velocity of the particles, and the smaller the diameter of the particles, G will affect the blocking of the particles. Second, by analyzing the settling motion of individual particles in the porous medium, we found that after the particles pass the entrance of the medium, the particles make symmetric and periodic (due to the symmetry and periodicity of the medium) settling motions. As a result, the particles will mainly reciprocate back and forth within a certain range of the main settling channels of the medium. By further analyzing the travel time, we found that decreasing the size of the pores (e_p) and increasing the diameter of the particles (d_p) both lead to larger travel times. This implies that smaller e_p and larger d_p (larger particle size ratio $\alpha = \frac{d_p}{e_p}$) will be more likely to lead to clogging.

For multiple particles, they will produce an accumulation at the pore constriction of the porous medium and this accumulation behavior repeats itself along the depth. When the size ratio is large, the accumulation of particles occurs mainly at the entrance of the medium. Besides, a critical value of the number of particles injected ($N_{injected}$) exists. At this time, the travel time will stop decreasing; the number of particles passing through the medium no longer increases (N^c_{exited}) and the number of particles retained ($N_{retained}$) by the medium begins to increase significantly; and the penetration of the particle population (Φ) also starts to decrease. All these results indicate that clogging begins to occur at this point. It is further indicated by the deposition profiles that particles are mainly retained at the entrance.

Observations of particle behavior in the pore space provide more details on the above results. For the entrance of the medium, the blockage of the porous medium as well as the blockage between particles causes them to accumulate at the pore constriction of the medium. When the number of accumulated particles is sufficiently large, it will induce the possibility of forming particle bridges. In the interior of the medium, the contact pattern between the particles and the pillars leads to channeling along the depth of the

medium into which further particles are captured. Therefore, the particle flowing out at the media entrance area (which determines the inter-particle blockage) is important for the formation of clogs inside the media. When α is large, particles can only flow out sequentially, and the accumulation of particles at the internal pores is mainly due to the medium structure blockage.

The inflow and outflow of particles, as well as the cumulative concentration change in the pore space, the contact pairs between particles, between particles and pillars can better reflect the dynamic clogging process. The contact pairs between particles can show the contact extension between particles, and when the cumulative concentration corresponds to about 0.45 ± 0.05 (random loose packing density [19]), the particles can fill the pore space, creating the possibility of clogging. Meanwhile, when the outflow of particles is 0, it shows the occurrence of clogging. At $N^c_{injected}$, this could make the cumulative concentration at the entrance reach the critical value, and consequently clogging begins to occur. Inside the medium, the inflow of particles can show the blockage between particles, which in turn determines the accumulation of particles and the occurrence of clogging.

The final statistical clogging probability is in agreement with the above clogging behavior. A larger $N_{injected}$ and α could induce a larger clogging probability. The particles will produce accumulation in the upper region of the medium more first, therefore, the clogging probability will decrease rapidly with depth.

Overall, this study reveals the transport and clogging characteristics of particles at the pore scale as well as within the tiny media region. A basic quantitative idea can better reflect this dynamic process. In the future, first, we can investigate the delayed effect of additional variables on the settling of individual particles, such as liquid flow rates, liquid viscosity, a larger range of particle sizes, density, and so on. This can provide the basis for the study of settling and clogging phenomena for multiple particles. Then, based on the quantitative ideas of this study, we can attempt to connect the kinetic and physical properties of the particle population with the clogging probability, while analyzing their distribution within the porous media, which further allows us to derive particle deposition profiles. In addition, the influence of more parameters, including physical parameters of the medium, particles, and fluid as well as different scales need to be further investigated.

NOMENCLATURE

$*$	Convolution operation
α	Particle size ratio
$\bar{N}_{entered}$	Average particle number entered the inlet among many tests
$\bar{N}_{exited}$	Average particle number exited from the outlet among many tests
$\bar{N}_{retained}$	Average particle number retained among many tests
$\bar{T}_m^*$	Mean particle travel time across medium among many tests
$\bar{t}_m^*$	Mean particle travel time across medium for multiple particles
$\bar{T}_p^*$	Mean particle travel time across pore space among many tests
$\bar{t}_p^*$	Mean particle travel time across pore space for multiple particles
$\bar{t}_{mj}^*, \bar{t}_{pj}^*$	Mean travel time across medium and pore space for test j
Δi	Maximum number of frames of gap that can be connected
Δt	Time interval
δ	The amount of overlap between particles or particle and medium grain
δ_t	Tangential displacement
γ	Weighting factor varying from 0 to 1
κ	Coefficient
λ	Capture efficiency
μ	Liquid viscosity
μ_g^γ	μ_g: dynamic viscosity of glycerol, γ is the weighting factor

μ_w^γ	μ_w: dynamic viscosity of water, γ is the weighting factor
μ_ϵ	Percentage change in viscosity of liquid mixtures in response to temperature fluctuations
μ_T	Viscosity of the liquid mixture at temperature T
Φ	The penetration of the particle population relative to the total particles that can enter the medium
ϕ	Porosity of porous medium
ϕ_s	Coefficient
ρ_g	Glycerol density
ρ_l	Liquid density
ρ_p	Particle density
ρ_w	Water density
σ	Standard deviation of the Gaussian filter
$\vec{F_d}$	Drag force
$\vec{F_i}$	Inertial force
$\vec{F_l}$	Lubrication force
$\vec{F_n}$	Normal contact force
$\vec{v_f}$	Flow velocity
$\vec{v}$	Particle velocity
$\vec{v}$	Particle velocity
$\vec{x}, \vec{z}, \vec{y}$	Unit vector in x, z and y axis
a, b	Coefficient
A_*	The surface area of half pore region corresponding to $A_1, A_2, ...A_{12}$

Ar Archimedes number

c, d The number of objects in two consecutive frames

c Particle concentration

C_1, C_2 Coefficients for determining the passage of particles through the inlet, outlet

c_u Uniform coefficient

C_v Glycerol fraction in volume

c_{lim} The limiting concentration showing particles forming bridge at pore throat

C_m Glycerol fraction in mass

CN_{pc} Contact number between particle and pillar

CN_p Contact number between particles

d_ϵ The experimental errors

D_f Medium grain diameter (pillar diameter)

d_i The distance between each two particles

d_p Particle diameter

$D_{15,f}, d_{85,p}$ the size corresponding to 15% and 85% of the cumulative distribution of particle sizes

$d_{\Delta i}$ Maximum gap distance between particles that can be connected

D_f Pillar diameter

d_{max} Maximum distance between particles that can be connected

E^* The equivalent modulus of elasticity

e_p Pore diameter

e_p Radial pore size between pillars

e_x, e_z The parameters in arrangement of obstacles

f Frequency of camera photo

f_s The coefficient of friction

F_t Tangential contact force

F_{net} The net force of gravity and buoyancy force

G The gap distance for the confined media

g Gravity acceleration

G_σ Gaussian filter

h The thickness of fluid film

I Original image pixel value matrix

i Frame number

k_t Tangential stiffness

L Length of the injection box

n Dimension of the source image

$N_{clogged}$ The number of clogged tests

$N_{entered}$ Particle number entered at the inlet

$N^j_{entered}$ Particle number entered in test j

$N^{\Delta t}_{entered}$ The number of particles passing through during Δt

N_{exited} Particle number exited from the outlet

N^j_{exited} Particle number exited in test j

$N_{injected}$ Particle number injected at the injection box

$N_{retained}$ Particle number retained in the corresponding region

P Clogging probability

Q	Quality value for the detected spots
q_{in}	Particle inflow rate, Particle number/s
q_{out}	Particle outflow rate, Particle number/s
r	Particle radius
r^*	The equivalent particle radius
S	Image scale
SG	Specific gravity
St	Stokes number
St_c	Critical stokes number
T	Temperature in °C
t_i	Recording time
t_{inlet}	Recording time while particle at inlet
t^*_{mj}, t^*_{pj}	Normalized travel time across medium and pore space for particle j
t_m	Particle travel time across medium
t^*_m	Normalized travel time for the particle across medium
t_{outlet}	Recording time while particle at outlet
t_{plate}	The travel time of the particles in the case of only front and back flat media
t_p	Particle travel time across pore space
t^*_p	Normalized travel time for the particle across pore space
v	Scalar particle velocity
v^*	Normalized velocity by v_{plate}
V_g	Glycerol volume

v_o	Particle velocity when particles accumulate at the orifice
v_s	Terminal settling velocity or Stokes velocity
V_w	Water volume
v_{plate}	Final steady settling scalar velocity at front and back plates
v_x	Particle velocity component in x axis
v_y	Particle velocity component in y axis
v_z	Particle velocity component in z axis
W	Width of the injection box
x_i, z_i	Detected particle center coordinate
z_{inlet}	The coordinate of the z-axis of the inlet for the corresponding region
z_{outlet}	The coordinate of the z-axis of the outlet for the corresponding region

List of Figures

Bibliography

[1] H. Y. Jeong, S.-C. Jun, J.-Y. Cheon, and M. Park, "A review on clogging mechanisms and managements in aquifer storage and recovery (ASR) applications", Geosciences Journal, vol. 22, *4*, pp. 667–679, Aug. 2018.

[2] J. Zhang, S. Xia, N. Hu, W. Hao, R. Han, B. Meng, and Z. Zhang, "Optimization of anti-clogging pervious pavement structure based on numerical evaluation", Construction and Building Materials, vol. 275, p. 122 186, 2021.

[3] Q. Liu, S. Liu, G. Hu, T. Yang, C. Du, and M. Oeser, "Infiltration Capacity and Structural Analysis of Permeable Pavements for Sustainable Urban: A Full-scale Case Study", Journal of Cleaner Production, vol. 288, p. 125 111, Mar. 2021.

[4] R. Dubuis and G. D. Cesare, "The clogging of riverbeds: A review of the physical processes", Earth-Science Reviews, 2023.

[5] E. S. Boek, C. Hall, and P. M. J. Tardy, "Deep Bed Filtration Modelling of Formation Damage Due to Particulate Invasion from Drilling Fluids", Transport in Porous Media, vol. 91, *2*, pp. 479–508, Jan. 2012.

[6] A. Zamani and B. Maini, "Flow of dispersed particles through porous media — Deep bed filtration", Journal of Petroleum Science and Engineering, vol. 69, *1-2*, pp. 71–88, Nov. 2009.

[7] M. Razzaghmanesh and M. Borst, "Investigation clogging dynamic of permeable pavement systems using embedded sensors", Journal of Hydrology, vol. 557, pp. 887–896, 2018.

[8] X. Du, X. Ye, and X. Zhang, "Clogging of saturated porous media by silt-sized suspended solids under varying physical conditions during managed aquifer recharge", Hydrological Processes, vol. 32, *14*, pp. 2254–2262, Jul. 2018.

[9] O. S. Q. Yousif, M. Karakouzian, N. O. A. Rahim, and K. A. Rashed, "Physical Clogging of Uniformly Graded Porous Media Under Constant Flow rates", Transport in Porous Media, vol. 120, *3*, pp. 643–659, Dec. 2017.

[10] H. S. Kandra, D. McCarthy, T. D. Fletcher, and A. Deletic, "Assessment of clogging phenomena in granular filter media used for stormwater treatment", Journal of Hydrology, vol. 512, pp. 518–527, May 2014.

[11] Y. Tang, X. Yao, Y. Chen, Y. Zhou, D. Z. Zhu, Y. Zhang, T. Zhang, and Y. Peng, "Experiment research on physical clogging mechanism in the porous media and its impact on permeability", Granular Matter, vol. 22, *2*, pp. 1–14, 2020, Publisher: Springer.

[12] D. L. Huston and J. F. Fox, "Clogging of Fine Sediment within Gravel Substrates: Dimensional Analysis and Macroanalysis of Experiments in Hydraulic Flumes", Journal of Hydraulic Engineering, vol. 141, *8*, p. 04 015 015, Aug. 2015.

[13] I. L. Molnar, W. P. Johnson, J. I. Gerhard, C. S. Willson, and D. M. O'Carroll, "Predicting colloid transport through saturated porous media: A critical review: Predicting Colloid Transport Through Saturated Porous Media", Water Resources Research, vol. 51, *9*, pp. 6804–6845, Sep. 2015.

[14] G. Benosman, "Migration de particules fines dans un milieux poreux: Application au phénomène de colmatage", fr, p. 201, `https://theses.hal.science/tel-00997415`.

[15] Q. Liu, B. Zhao, and J. C. Santamarina, "Particle Migration and Clogging in Porous Media: A Convergent Flow Microfluidics Study", Journal of Geophysical Research: Solid Earth, vol. 124, *9*, pp. 9495–9504, 2019.

[16] P. Bacchin, Q. Derekx, D. Veyret, K. Glucina, and P. Moulin, "Clogging of microporous channels networks: Role of connectivity and tortuosity", Microfluidics and Nanofluidics, vol. 17, *1*, pp. 85–96, Jul. 2014.

[17] J. M. Frey, P. Schmitz, J. Dufreche, and I. G. Pinheiro, "Particle Deposition in Porous Media: Analysis of Hydrodynamic and Weak Inertial Effects",

[18] D. Gella, I. Zuriguel, and D. Maza, "Decoupling geometrical and kinematic contributions to the silo clogging process", Physical Review Letters, vol. 121, *13*, p. 138 001, 2018.

[19] G. Gerber, S. Rodts, P. Aimedieu, P. Faure, and P. Coussot, "Particle-Size-Exclusion Clogging Regimes in Porous Media", Physical Review Letters, vol. 120, *14*, p. 148 001, Apr. 2018.

[20] J. E. Schindelin, I. Arganda-Carreras, E. Frise, V. Kaynig, M. Longair, T. Pietzsch, S. Preibisch, C. T. Rueden, S. Saalfeld, B. Schmid, J.-Y. Tinevez, D. J. White, V. Hartenstein, K. W. Eliceiri, P. Tomancčák, and A. Cardona, "Fiji: An open-source platform for biological-image analysis", Nature Methods, vol. 9, pp. 676–682, 2012.

[21] D. Ershov, M.-S. Phan, J. Pylvänäinen, S. Rigaud, L. Le Blanc, A. Charles-Orszag, J. Conway, R. Laine, N. Roy, D. Bonazzi, G. Duménil, G. Jacquemet, and J.-Y. Tinevez, "Trackmate 7: Integrating state-of-the-art segmentation algorithms into tracking pipelines", English, Nature Methods, vol. 19, *7*, pp. 829–832, Jul. 2022, © 2022. The Author(s), under exclusive licence to Springer Nature America, Inc.

[22] C. Tien and B. V. Ramarao, Granular filtration of aerosols and hydrosols, 2nd ed. Amsterdam ; Boston: Elsevier, 2007, ISBN: 978-1-85617-458-9.

[23] A. Jewel, K. Fujisawa, and A. Murakami, "Effect of seepage flow on incipient motion of sand particles in a bed subjected to surface flow", Journal of Hydrology, vol. 579, p. 124 178, Dec. 2019.

[24] Z. Wang, X. Du, Y. Yang, and X. Ye, "Surface clogging process modeling of suspended solids during urban stormwater aquifer recharge", Journal of Environmental Sciences, vol. 24, *8*, pp. 1418–1424, 2012.

[25] A. Singh, P. V. Sampath, and K. P. Biligiri, "A review of sustainable pervious concrete systems: Emphasis on clogging, material characterization, and environmental aspects", Construction and Building Materials, vol. 261, p. 120 491, Nov. 2020.

[26] T. F. Fwa, S. A. Tan, and Y. K. Guwe, "Laboratory evaluation of clogging potential of porous asphalt mixtures", Transportation Research Record, vol. 1681, pp. 43–49, 1999.

[27] C. F. Yong, D. T. McCarthy, and A. Deletic, "Predicting physical clogging of porous and permeable pavements", Journal of Hydrology, vol. 481, pp. 48–55, Feb. 2013.

[28] M. Razzaghmanesh, "A Review of Permeable Pavement Clogging Investigations and Recommended Maintenance Regimes", Water, vol. 10, Mar. 2018.

[29] A. Radfar and T. D. Rockaway, "Clogging Prediction of Permeable Pavement", Journal of Irrigation and Drainage Engineering, vol. 142, *4*, p. 04 015 069, Apr. 2016, Publisher: American Society of Civil Engineers.

[30] J. Sansalone, X. Kuang, G. Ying, and V. Ranieri, “Filtration and clogging of permeable pavement loaded by urban drainage”, Water Research, Special Issue on Stormwater in urban areas, vol. 46, *20*, pp. 6763–6774, Dec. 2012.

[31] H. Kandra, D. McCarthy, and A. Deletic, “Assessment of the Impact of Stormwater Characteristics on Clogging in Stormwater Filters”, Water Resources Management, vol. 29, *4*, pp. 1031–1048, Mar. 2015.

[32] R. Sakthivadivel and H. A. Einstein, “Clogging of porous column of spheres by sediment”, Journal of the Hydraulics Division, vol. 96, *2*, pp. 461–472, 1970.

[33] S. Gibson, D. Abraham, R. Heath, and D. Schoellhamer, “Vertical gradational variability of fines deposited in a gravel framework”, Sedimentology, vol. 56, *3*, pp. 661–676, 2009.

[34] S. Gibson, D. Abraham, R. Heath, and D. Schoellhamer, “Bridging process threshold for sediment infiltrating into a coarse substrate”, Journal of Geotechnical and Geoenvironmental Engineering, vol. 136, *2*, pp. 402–406, 2010.

[35] M. Brunke, “Colmation and depth filtration within streambeds: Retention of particles in hyporheic interstices”, International Review of Hydrobiology, vol. 84, *2*, pp. 99–117, 1999.

[36] J. R. Valdes and J. C. Santamarina, “Particle Clogging in Radial Flow: Microscale Mechanisms”, SPE Journal, vol. 11, *02*, pp. 193–198, Jun. 2006.

[37] J. Fan, “Numerical study of particle transport and deposition in porous media”, `https://theses.fr/2018ISAR0003`, PhD Thesis, 2018.

[38] H. Hertz, “The contact of elastic solids”, J Reine Angew, Math, vol. 92, pp. 156–171, 1881.

[39] H. Hertz, “On the contact of solids—on the contact of rigid elastic solids and on hardness”, Miscellaneous papers, pp. 146–183, 1896.

[40] C. Tien and A. C. Payatakes, “Advances in deep bed filtration”, Aiche Journal, vol. 25, pp. 737–759, 1979.

[41] J. S. Andrade, A. D. Araújo, T. F. Vasconcelos, and H. J. Herrmann, “Inertial capture in flow through porous media”, The European Physical Journal B, vol. 64, *3-4*, pp. 433–436, Aug. 2008.

[42] C. Ghidaglia, “Filtration en profondeur de particules”, 1994.

[43] J. P. Herzig, D. M. Leclerc, and P. L. Goff, "Flow of Suspensions through Porous Media—Application to Deep Filtration", Industrial & Engineering Chemistry, vol. 62, *5*, pp. 8–35, May 1970.

[44] D. Gella, D. Maza, I. Zuriguel, A. Ashour, R. Arévalo, and R. Stannarius, "Linking bottleneck clogging with flow kinematics in granular materials: The role of silo width", Physical Review Fluids, vol. 2, Aug. 2017.

[45] K. To, "Jamming transition in two-dimensional hoppers and silos", Physical Review E, vol. 71, *6*, p. 060 301, 2005.

[46] N.-S. Cheng, "2008 Formula for the viscosity of a glycerol-water mixture", May 2008.

[47] T. Lindeberg, "Feature detection with automatic scale selection", Int. J. Comput. Vision, vol. 30, *2*, pp. 79–116, Nov. 1998.

[48] K. Jaqaman, D. Loerke, M. Mettlen, H. Kuwata, S. Grinstein, S. L. Schmid, and G. Danuser, "Robust single particle tracking in live cell time-lapse sequences", Nature methods, vol. 5, pp. 695–702, 2008.

[49] E. T. d. Vries, Q. Tang, S. Faez, and A. Raoof, "Fluid flow and colloid transport experiment in single-porosity sample; tracking of colloid transport behavior in a saturated micromodel", Advances in Water Resources, vol. 159, p. 104 086, 2022.

[50] D. G. Lowe, "Distinctive image features from scale-invariant keypoints", Int. J. Comput. Vision, vol. 60, *2*, pp. 91–110, Nov. 2004.

[51] P. d. Haan, "On the use of density kernels for concentration estimations within particle and puff dispersion models", en, Atmospheric Environment, vol. 33, *13*, pp. 2007–2021, Jun. 1999.

[52] B. W. Silverman, Density estimation for statistics and data analysis. Routledge, 2018.

[53] N.-B. Heidenreich, A. Schindler, and S. Sperlich, "Bandwidth selection for kernel density estimation: A review of fully automatic selectors", en, AStA Advances in Statistical Analysis, vol. 97, *4*, pp. 403–433, Oct. 2013.

RÉSUMÉ ÉTENDU EN FRANÇAIS

Le transport et le colmatage des suspensions dans les milieux poreux sont des problèmes cruciaux dans toute une série d'applications de génie civil, notamment la restauration des aquifères, la maintenance des chaussées drainantes, la gestion des lits de rivière et dans d'autres domaines comme le génie pétrolier. Ces phénomènes peuvent affecter de manière significative l'efficacité et la performance économique de ces systèmes. Par exemple, le colmatage peut réduire la capacité de recharge des aquifères, la capacité d'infiltration dans les chaussées perméables.

Des recherches approfondies ont été menées à l'aide d'expériences sur des colonnes macroscopiques afin d'explorer l'impact sur le colmatage de différents paramètres tels que la taille des particules, la concentration, la granulométrie du milieu et les taux d'injection. Ces études visent à comprendre les changements de perméabilité, les profils de dépôt et les pertes de charge dans les milieux poreux. Cependant, les valeurs critiques pour prédire le colmatage sur la base des rapports de taille des particules ne sont pas cohérentes d'une étude à l'autre, et la quantification de l'impact de ces grandeurs reste un défi. Cette complexité est attribuée à l'observation insuffisante du processus de dépôt des particules et aux interactions complexes entre les particules, les fluides et les milieux.
Au niveau microscopique, le dépôt de particules implique diverses forces mécaniques telles que la gravité, la poussée, l'inertie et la force de traînée. Les chercheurs ont introduit des nombres sans dimension tels que le nombre de Stokes et le nombre d'Archimède pour quantifier ces forces. Des études sont en cours pour comprendre comment ces forces, ainsi que la taille des particules, la nature du fluide et la structure du milieu, affectent le dépôt et le colmatage. Bien que certains modèles aient été développés pour prédire la probabilité de colmatage au niveau du collet des pores et pour décrire le profil de dépôt dynamique, des recherches supplémentaires sont nécessaires pour affiner ces modèles et incorporer d'autres facteurs affectant le processus de colmatage.

Dans ce travail, on s'intéresse à l'étude des trajectoires et des vitesses de particules dans un milieu poreux saturé en fonction du nombre de particules injectées et en fonction

de la taille des particules et de la taille de la plus petite constriction du milieu. L'objectif étant d'étudier le comportement mécanique de ces particules jusqu'au colmatage du milieu poreux. Nous cherchons également à évaluer la probabilité de colmatage en fonction des paramètres cités.

Pour ce faire, nous avons retenu la méthode de visualisation et de suivi de particules à l'aide de caméra rapide dans le domaine du visible. Nous avons conçu des milieux poreux modèles transparents en fixant des pastilles de section circulaire de diamètre D_f entre deux parois parallèles transparentes. L'épaisseur entre ces plans est de 1.5 fois celle des particules injectées pour réduire au maximum le mouvement latéral. Les pastilles sont disposées en quinconce selon six lignes dans le sens vertical. Elles sont disposées selon un motif triangulaire isocèle d'angle à la base égal à 45°. Les constrictions les plus étroites dont la taille est notée e_p se trouvent alors le long des côtés les plus longs. Nous avons utilisé trois milieux notés M1, M2 et M3 tel que le rapport $\frac{e_p}{D_f}$ est : 0.41, 0.34, 0.31 respectivement. Les particules injectées sont des petites billes en verre de diamètre d_p de 1mm, $2mm$ et $3mm$. Toutes les expériences sont menées en condition monodisperse, si bien que le rapport entre la taille de particule et la constriction la plus étroite ($\alpha = \frac{d_p}{e_p}$) peut prendre les valeurs : 0.24, 0.29, 0.32, 0.48, 0.58, 0.65, 0.72, 0.87. Le fluide qui sature le milieu est de l'huile de glycérine et un mélange de glycérine et d'eau, réputée très visqueuse pour réduire la vitesse des particules. Compte tenu de la densité des particules, de celle du fluide et la viscosité du fluide, la vitesse des particules est de l'ordre du mm/s.

Les images obtenues à l'aide de la caméra de fréquence maximale de 330 $images/s$ sont traitées avec le logiciel libre ImageJ. L'algorithme employé est Trackmate qui permet de détecter la position des particules dans chaque image. On obtient ainsi un ensemble de données (x, z, t) pour chaque particule qui seront ensuite utilisées pour le calcul des caractéristiques dynamiques des particules telles que la vitesse, le temps de parcours, la concentration de particules, le contact entre les particules et le contact entre les particules et les pastilles.

La technique expérimentale et la méthode de traitement d'images sont d'abord appliquées aux cas simples de chute de particule entre deux plans parallèles dont on varie la distance et le cas d'une particule statique posée sur une pastille. Cela nous a permis d'ajuster la fréquence d'acquisition d'images afin de réduire les fluctuations de vitesses et

de calibrer l'outil pour détecter finement le contour d'une particule et le contact particule/pastille.

Avant d'analyser le comportement de groupes de particules, on s'est d'abord focalisé sur le comportement d'une particule individuelle pour les trois diamètres et dans les trois milieux poreux proposés. Nous avons ainsi analysé les grandeurs cinématiques lors de l'infiltration ainsi que le temps de transit de la particule. Nous avons également étudié la variation de ces grandeurs lorsque la particule est injectée en un point d'un axe de symétrie vertical et en d'autres points de la même ligne horizontale mais à différentes positions de part et d'autre de l'axe de symétrie. On constate que lorsque la particule a franchi la première ligne d'obstacles, son comportement cinématique ne dépend plus de la position d'injection. Le temps de transit moyen dans le milieu augmente évidemment lorsque le diamètre de la particule augmente en raison de la résistance du fluide et le blocage des piliers. Pour un diamètre donné, ce temps diminue lorsque le point d'injection est de plus en plus éloigné de l'axe de symétrie. Le milieu poreux étant constitué de six lignes d'obstacles dans le sens vertical, on définit ainsi cinq couches. Le temps de traversée de chaque couche est quasiment le même quelle que soit la couche lorsque la particule est injectée en un point de l'axe de symétrie. Il diminue pour la première couche lorsque le point d'injection s'éloigne du point de l'axe de symétrie et reste invariant pour les couches inférieures.

Dans le but de déterminer et d'analyser les causes du colmatage d'un milieu poreux par des particules en sédimentation dans celui-ci, nous avons suivi le comportement d'un ensemble de particules. Les groupes de particules étudiés comportent 4, 10, 20, 40, 60 , 80 et jusqu'à 400 particules pour le diamètre 1, 2 et 3 mm. Le système d'injection est composé d'une boîte avec une ouverture linéaire de largeur légèrement supérieure au diamètre de la particule concernée. pour permettre de lâcher les particules au même moment. Cependant la taille de l'ouverture est fixe si bien que selon la taille et le nombre de particules, celles-ci peuvent être superposées sur plusieurs lignes dans la boîte d'injection. Ainsi, au-delà de 10 particules, celles-ci ne rentrent pas dans le milieu en même temps. Pour réduire les erreurs dues à cette injection aléatoire, nous avons moyenné les mesures de vingt tests.
Nous nous sommes intéressés aux profils de concentration des particules dans les trois milieux étudiés et pour les trois valeurs de diamètre retenues. On a d'abord montré comment ces profils évoluent dans le temps. Ces profils présentent des pics de concentration aux

premiers instants et à l'entrée du milieu poreux. De nouveaux pics apparaissent en profondeur lorsque le nombre de particules injectées est suffisamment grand. Ainsi on montre l'existence d'un nombre critique de particules au-delà duquel les particules s'accumulent dans le milieu poreux. Ce nombre critique dépend du rapport (α) des tailles des particules et des pores. Par ailleurs, lorsque α augmente, l'accumulation de particules se produit essentiellement en surface et pour des valeurs de α petites, cette accumulation en surface se produit pour les particules de grand diamètre.

Ensuite, nous avons calculé le temps moyen de déplacement de la population de particules dans l'ensemble du milieu et dans chaque couche sous les différentes conditions du nombre de particules injectées et de α. Pour les petites valeurs de α, jusqu'à 0.3, le temps de transit à travers tout le milieu est constant quel que soit le nombre de particules injectées, jusqu'à 400. Cependant, lorsque α augmente, le temps de transit varie avec le nombre de particules injectées. En effet, pour augmenter α, soit on augmente d_p soit on diminue e_p, ce qui augmente les contacts particules/pastilles et crée des occlusions qui ont pour conséquence d'augmenter le temps. L'analyse du temps de traversée de chaque couche montre que le temps de traversée de la première couche est le plus grand, celui des autres couches est quasiment constant. Ce qui pourrait s'expliquer par l'existence d'un temps de structuration de l'infiltration.

En analysant les flux de particules entrant et sortant du milieu, on détermine la concentration des particules retenues dans le milieu sous diverses conditions sur la taille des particules et la taille des pores. Le comptage du nombre de cas de colmatage parmi les nombreux essais réalisés a permis de quantifier la probabilité de colmatage selon le nombre de particules injectées et le rapport de tailles. Enfin, l'analyse des résultats, montre que la probabilité de colmatage augmente significativement avec l'augmentation du nombre de particules injectées et en particulier après avoir atteint ou dépassé un nombre critique de particules propre à chaque milieu.

COLLEGE DOCTORAL BRETAGNE SCIENCES POUR L'INGENIEUR

INSA INSTITUT NATIONAL DES SCIENCES APPLIQUÉES RENNES

Titre : Visualisation et analyse du dépôt de particules dans un milieu poreux jusqu'à son colmatage

Mot clés : Visualisation, sédimentation, comportement de colmatage, milieux poreux

Résumé : La manière dont les particules en suspension se déposent et conduisent au colmatage des milieux poreux est cruciale pour de nombreux scénarios d'application. Cette recherche utilise un modèle de milieu poreux transparent pour visualiser la sédimentation et le dépôt des particules. L'utilisation d'un algorithme de détection de particules sur des images obtenues par caméra rapide permet de suivre leurs trajectoires et leurs vitesses. L'analyse du comportement mécanique de ces particules est menée en fonction de la taille des particules et de celle des pores. Premièrement, l'analyse a montré que la gravité régit le mouvement d'une seule particule. Les trajectoires d'une particule injectée à différentes positions se rejoignent une fois qu'elles aient passé les premiers obstacles. Chaque trajectoire contourne les obstacles tout en conservant un mouvement globalement vertical d'infiltration profonde. Quant à la vitesse, elle est influencée par la présence d'obstacles et celle du fluide. Ensuite, l'injection d'un nombre croissant de particules a permis de montrer un nombre critique de particules au-delà duquel les particules s'accumulent dans le milieu poreux. Ce nombre critique dépend du rapport des tailles des particules et des pores. Cette accumulation de particules conduirait au colmatage du milieu poreux caractérisé par un flux sortant de particules nul. Le comptage du nombre de cas de colmatage parmi les nombreux essais réalisés a permis de quantifier la probabilité de colmatage selon le nombre de particules injectées et selon le rapport de tailles.

Title: Visualization and analysis of particle settling and clogging behavior in porous media

Keywords: Visualization, sedimentation, clogging behavior, porous media

Abstract: How suspended particles deposit and lead to clogging in a porous medium is crucial for many application scenarios. This research uses a transparent model of porous medium to visualize particle behaviors. The use of a particle detection algorithm on high-speed camera images enables us to track particle trajectories and velocities. The particle mechanical behavior is analyzed at different size ratios (particle size divided by pore size). Firstly, analysis has shown that gravity governs the single particle motion. The trajectories of a particle injected at different positions converge once it has passed the first obstacles. Each trajectory bypasses the obstacles while maintaining an overall vertical motion of deep infiltration. Velocity is influenced by the presence of obstacles and the fluid itself. Next, the injection of an increasing number of particles has demonstrated a critical number of particles beyond which particles accumulate in the porous medium. This critical number depends on the size ratio. This accumulation would lead to clogging and can be characterized by zero particle outflow. By counting the number of clogging cases over multiple tests, we can quantify the probability of clogging as a function of the number of particles injected and the particle size ratio.